Terahertz Laser Spectroscopy of Two- and Three-Dimensional Topological Insulators based on HgTe Nanostructures

Dissertation

zur Erlangung des Doktorgrades der Naturwissenschaften
doctor rerum naturalium
(Dr. rer. nat.)
an der Fakultät für Physik
Universität Regensburg

vorgelegt von
Kathrin-Maria Dantscher
aus Regensburg

im Jahr 2017

Die Arbeit wurde von Prof. Dr. Sergey D. Ganichev angeleitet.

Das Promotionsgesuch wurde am 08. Juni 2017 eingereicht.

Prüfungsausschuss:

Vorsitzender:	Prof. Dr. Vladimir Braun
1. Gutachter:	Prof. Dr. Sergey D. Ganichev
2. Gutachter:	Prof. Dr. Christian Schüller
weiterer Prüfer:	Prof. Dr. Josef Zweck

Contents

1 Introduction

The utilization of the mathematical concept of topology to complement the band theory of solids can be considered as one of the milestones in solid-state physics in the last few decades. At the time of the introduction, most scientists believed that the band theory – originally developed by Felix Bloch in 1928 [1] – has already been well-understood. This concept acts as the basis for today's understanding of the band structure of crystals; therefore, it has been thoroughly investigated and has led to many technological developments. However, in 1972, J.M. Kosterlitz and D.J. Thouless introduced the concept of topology to identify new phases of matter [2, 3], for which they, together with F.D.M. Haldane [4, 5], were awarded the Nobel Prize 2016 in physics [6].

Their approach not only allowed the explanation of the quantization of the Hall conductance [7], it also enabled the prediction of a new class of materials called topological insulators [8, 9]. These fascinating materials are insulating in the bulk but exhibit topological protected gapless edge or surface states, which can be described by the Dirac equation for massless particles. The existence of such topological states has been predicted and experimentally proved in diverse materials [10]. Among these materials, an outstanding candidate is mercury telluride, which allows the fabrication of Dirac fermion systems with a high quality [11–13].

Mercury telluride is a narrow band gap semiconductor composed of heavy elements. In such a material, the strong spin-orbit coupling, together with relativistic effects, can lead to an inverted band structure [14, 15]. Due to this extraordinary band ordering, Dirac fermions can be realized in different ways in mercury telluride – either as a two-dimensional electron gas in quantum well structures at a characteristic thickness [16] or in two- or three-dimensional topological insulators [17, 18]. Whereas the former is characterized by unpolarized two-dimensional Dirac fermions [19], the latter exhibit a strict spin-polarization, which leads to a dissipationless transport along the edges or in the surface states [9]. This variety of Dirac fermion systems allows a broad investigation of these states and their properties.

Recently, it has been demonstrated that spin-dependent photogalvanic effects are a good tool for the investigation of Dirac fermion systems [20]. For example, photocurrents can be generated in the surface states of three-dimensional topological insulators Bi_2Se_3 [21] or BiTe and SbTe [22] with polarized radiation. In the two-dimensional case Olbrich *et al.* investigated HgTe quantum wells with different thickness, which are characterized by a normal, inverted, or Dirac-like dispersion, with the help of cyclotron resonance [23]. Although this work clearly demonstrates, that such enhanced photocurrents provide a unique selective access to details of the band structure of these systems, the study is limited to Dirac fermions in systems with critical thickness, which are spin-generated. As this study acts as one of the bases of this thesis, its results are summarized in Chapter 2, together with the fundamental concepts of topological insulators, photogalvanic effects, and the effect of cyclotron resonance. In Chapter 3, a brief overview of the used setup, the different measurement methods, and the investigated samples is given.

In this thesis, spin-polarized Dirac fermions in two- and three-dimensional topological insulators based on mercury telluride are investigated by means of terahertz laser spectroscopy. This study starts with the observation of cyclotron-resonance-enhanced photocurrents excited in three-dimensional HgTe films [24]. The obtained results are presented and discussed in Chapter 4. There the cyclotron resonance behaviour is analysed in regard to the band structure of the system, which allows an assignment of the observed photocurrents to the topologically protected top and bottom surface states. Furthermore, it is shown that such an opto-electronic study provides a sensitive method to probe the cyclotron masses and the mobility of two-dimensional Dirac surface states, even when the Fermi level lies in the conduction band or for micrometre-sized samples, for which pure optical methods are almost impossible.

In the second part, photocurrents flowing in the helical edge states are observed for the first time by exciting HgTe based two-dimensional topological insulators with circularly polarized terahertz radiation [25]. The corresponding study is described in Chapter 5 in great detail. It is demonstrated that this current arises due to a selective excitation of spin-up and spin-down electrons, which

causes an imbalance of the electron distribution between positive and negative wave vectors. Therefore, the associated photogalvanic current reverses its direction upon switching the helicity of the radiation. This observation provides a novel access for the probing of spin-transport in two-dimensional topological insulators.

The main results of the analysis of the two- and three-dimensional topological insulators are specified in the final chapter, which provides a summary and an outlook.

2 Physical Background

This chapter presents the theoretical background necessary to understand the experimental investigation of mercury telluride (HgTe)-based two- (2D) and three-dimensional (3D) topological insulators with terahertz radiation-induced opto-electronic effects. It starts with the fundamental concepts of 2D and 3D topological insulators and their realization in HgTe. As the novel transport properties of these structures are studied by means of terahertz radiation-induced photocurrents, the second section depicts the linear and circular photogalvanic effects, followed by an introduction to the cyclotron resonance. Finally, a summary of a preliminary investigation of cyclotron-resonance-enhanced photocurrents in HgTe quantum wells with parabolic and Dirac-like dispersions are outlined. The latter acts as a basis for the understanding of the photocurrents in non-trivial systems, which are discussed in the following chapters.

2.1 Topological Insulators

In the easiest picture a topological insulator (TI) is a material with an insulating bulk and metallic states at the boundary. These systems have been labelled as topological insulators because the edge (in 2D TIs) or surface (in 3D TIs) states originate from the topology of the system. For an easier understanding, first the Chern insulators are discussed, with which the basic concepts of topology in solid-state physics are introduced. Then, an overview of the elemental features concerning 2D and 3D topological insulators [26–28] is briefly outlined.

2.1.1 Chern Insulators

In solid-state physics, all electronic properties can usually be described mathematically with the Schrödinger equation $E\psi = \mathcal{H}\psi$, where $\mathcal{H}(\boldsymbol{k})$ is the Hamilton operator and $E(\boldsymbol{k})$ is the energy of the system in dependence on the crystal momentum $\boldsymbol{k}$. In a crystal, the corresponding energy eigenfunctions are written as Bloch wave functions $\psi(\boldsymbol{k})$ [1] and their eigenvalues define the energy

bands of the system. In the band theory of solids, an insulator is characterized by a gap between the last filled band (valence band (VB)) and the first empty one (conduction band (CB)), with the Fermi energy E_F in between. If the Hamiltonians of two insulators can interpolate continuously into each other without closing the energy gap, they are topologically equivalent [29,30]. However, in some cases, such an interpolation is not possible and a gap closing has to occur somewhere along the structure, leading to metallic states on the interface [30].

Different topological classes can be distinguished by an invariant $n \in \mathbb{Z}$ called Chern number [31]. This number is defined as the integral over the Berry curvature $\mathcal{F}_m(\boldsymbol{k})$, which describes geometrical properties of the wave function in the Brillouin zone. The Chern number for the *m'th* energy band is given as:

$$n_m = \frac{1}{2\pi} \int d^2\boldsymbol{k} \mathcal{F}_m. \tag{1}$$

By summarizing n_m over all occupied bands N the total Chern number of a systems is given by:

$$n = \sum_{m=1}^{N} n_m. \tag{2}$$

This invariant cannot change as long as the Hamiltonian varies smoothly and the band gap is not closed. In other words, two Hamiltonians with different Chern numbers cannot interpolate continuously and they belong to different topological classes.

In this sense, most insulators are the topological equivalent to vacuum, which – according to Dirac's relativistic quantum theory – can be seen as a wide band semiconductor with the Fermi energy in the gap. These insulators yield a Chern number equivalent to zero and are labelled as topologically trivial. One of the most famous topologically non-trivial Chern insulators ($n \neq 0$) is the integer quantum Hall effect (QHE), discovered experimentally by K. von Klitzing *et al.* in 1980 [32]. In their work, they showed that a two-dimensional electron gas in a strong magnetic field can lead to conducting one-dimensional channels at the edges of the sample with a quantized Hall conductance σ_{xy} of:

$$\sigma_{xy} = \frac{e^2}{h}\nu, \tag{3}$$

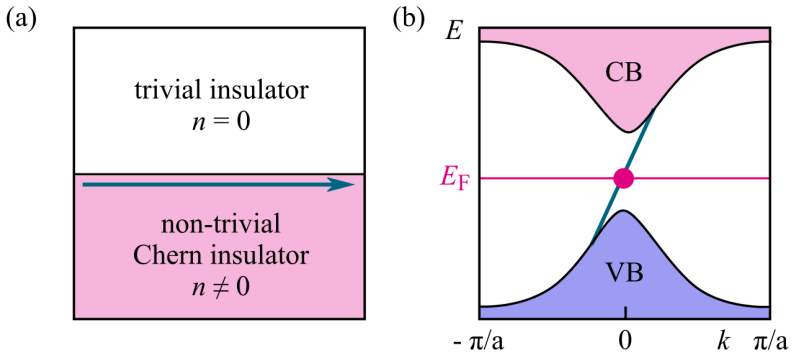

Figure 1: (a) At the interface between a trivial and a non-trivial Chern insulator, the band gap cannot interpolate continuously; therefore, it has to close at some point. This closing leads to conducting chiral states at the edges of the non-trivial insulator. (b) Electronic structure with a single edge state connecting the valence (VB) and the conduction band (CB). Red dot indicates the crossing point between the Fermi energy E_F and the edge states. Picture according to Ref. [30].

where e is the elementary charge, h the Planck's constant, and ν the filling factor. In 1982 Thouless *et al.* [7] expressed Eq. (3) mathematically in terms of the Berry phase and showed that the filling factor is equal to the Chern number.

Therefore, the main features of the QHE can be explained with the help of topology [33, 34]. As already mentioned the Hamiltonian of two insulators with different Chern numbers cannot by definition continuously interpolate if they are put into contact. Somewhere at the interface, the bands have to close and conducting edge states arise (see Fig. 1(a)). These edge states propagate only in a certain direction at one interface, which is referred to as chiral. As there are no counter-propagating states at the same edge, no backscattering is possible. Moreover, the conductivity of these states has to be quantized, because the Chern invariant can only change in integers. In $\boldsymbol{k}$-space, the edge states are represented by a single band connecting the bulk conduction and valence band. This is depicted in Fig. 1(b).

Since a magnetic field is needed for the QHE, the time reversal (TR) symmetry is broken. Moreover, the TR breaking can be seen directly in the Hall conduc-

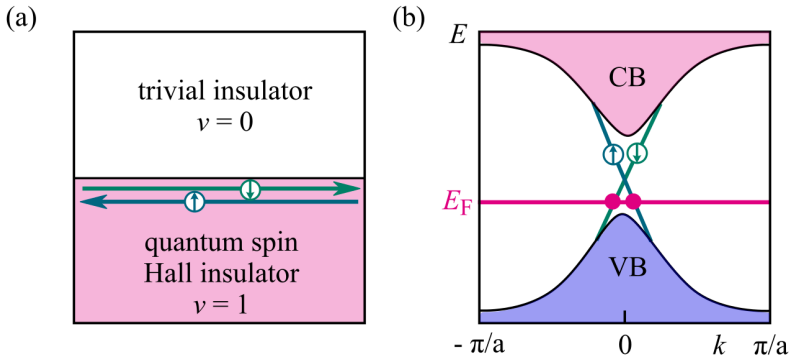

Figure 2: (a) Interface between a quantum spin Hall insulator and a trivial insulator. Green and blue lines represent helical edge states, where spin-up and spin-down electrons propagate in opposite directions. (b) Schematic band structure with edge states closing the band gap between the valence band (VB) and the conduction band (CB). Picture according to Ref. [30].

tivity (Eq. (3)), which is odd under time reversal ($t \to -t$). This led to the assumption that topologically non-trivial states can only occur in the presence of a high magnetic field. However, in 1988, Haldane [5] predicted a quantized Hall state for electrons moving on a graphene-like lattice in the absence of an external macroscopic magnetic field. Based on this idea, C.L. Kane and E.J. Mele [9] predicted the quantum spin Hall (QSH) effect in graphene. In QSH systems, the external magnetic field is replaced by the intrinsic spin-orbit interaction and thus the TR symmetry remains [8,35,36]. This has non-trivial consequences, as briefly outlined in the following chapter.

2.1.2 Two-dimensional Topological Insulator

In quantum mechanics, TR symmetry is represented by an anti-unitary operator $\mathcal{T} = TK$, where T is a unitary operator and K represents the complex conjugation. For spin 1/2 particles, the operator $\mathcal{T}$ squares to minus one ($\mathcal{T}^2 = -1$) and Kramer's theorem has to be applied [37]. This theorem declares that all eigenstates of a TR-invariant Hamiltonian have to be double-degenerated. Such pairs of degenerated states are known as Kramer pairs. This degeneracy is valid for all states of a TR symmetric system, even for edge states, which arise at the interface of two TR symmetric insulators with

different topological classification. Without spin-orbit interaction, Kramer's theorem leads to a degeneracy of the spin-up (↑) and -down (↓) states, whereas in a system with strong spin-orbit interaction, the states have to satisfy:

$$\mathcal{T}\,|k,\uparrow\rangle = |-k,\downarrow\rangle\,. \tag{4}$$

This leads to helical states, where carriers with a given spin move in one direction and the fermions having the opposite spin move in the opposite direction. In Fig. 2(a), this situation is schematically shown for the interface between a QSH insulator and a trivial insulator. The conducting channels are depicted in blue for spin-up and in green for spin-down electrons. This spin-momentum-locking results in a fully spin-polarized current. Moreover, backscattering between these Kramer pairs is forbidden, as the electron would have to flip its spin. Therefore, in this simple picture, the transport is regarded as dissipationless. A scheme of the corresponding band structure can be seen in Fig. 2(b). As before, the lines represent the edge states for spin-up and -down states, which are degenerated at $k = 0$ and non-degenerated at $k \neq 0$.

Analogous to the Chern insulator, which is grouped using Chern numbers, two-dimensional systems can be classified by the $\mathbb{Z}_2 = \{0, 1\}$ invariant, where $\mathbb{Z}_2 = 0$ represents the trivial and $\mathbb{Z}_2 = 1$ the non-trivial phase [30, 35]. One way to determine the $\mathbb{Z}_2$ invariant of a system, developed by L. Fu and C. L. Kane [38], is briefly introduced here. In Fig. 3(a) and (b), two examples of the energy dispersion of edge states in a two-dimensional insulator are plotted. Here, only half of the Brillouin zone ($0 < k_x < \Gamma_b = \pi/a$ where a is the lattice constant) is shown, as the other half ($\Gamma_a = -\pi/a < k_x < 0$) has to be the mirror image due to TR symmetry. Again, the red and blue shaded areas show the CB and VB respectively. In addition, possible edge states in the bulk gap are depicted in black.

At the TR invariant momenta $k_x = 0$ and $k_x = \Gamma_b$, these states are spin-degenerated, whereas for all other k_x, they are split due to the spin-orbit interaction, as seen in Eq. (4). The TR invariant points can connect in two different ways. They can reconnect pairwise, so that states that are connected at $k_x = 0$ join again at $k_x = \pm\pi/a$, as shown in Fig. 3(a). Alternatively, they can change their partner between these points, which is depicted in Fig. 3(b).

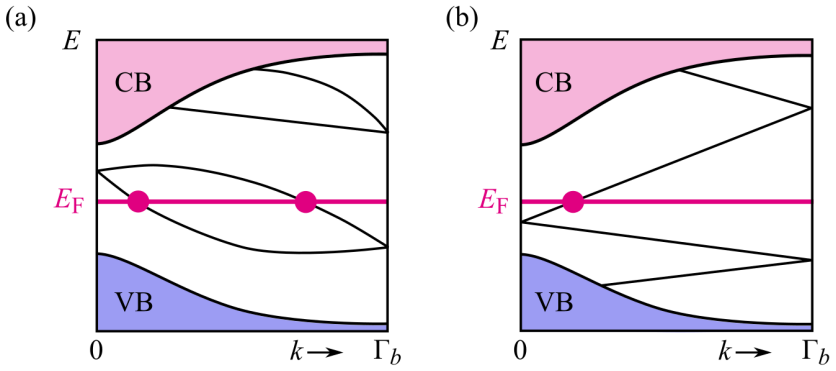

Figure 3: Possible energy dispersions of a time-reversal symmetric insulator along the edge. At $k_x = 0$ and $k_x = \Gamma_b = \pm\pi/a$ the surface bands are spin-degenerated, whereas in between these TR invariant points, the bands are split due to spin-orbit interaction. (a) The two states originating from $k_x = 0$ join again at $k_x = \Gamma_b$. This leads to an even number of crossing points between E_F and the edge states and therefore to a trivial phase ($\mathbb{Z}_2 = 0$). (b) The edge states originating from $k_x = 0$ do not rejoin at $k_x = \Gamma_b$ but combine with different partners. Therefore, they cannot be shifted out of the gap. This is characterized by an odd number of crossing points, which results in a non-trivial phase ($\mathbb{Z}_2 = 1$). Picture according to Ref. [30].

In the first case, the edge states can be eliminated by pushing them completely out of the band gap, which results in an empty band gap and therefore, in a trivial system ($\mathbb{Z}_2 = 0$). This situation is characterized by an even number of intersections of the Fermi level with the edge states. However, in the second case, the edge states cannot be pushed out of the gap; there is always an odd number of intersections between the conducting state and the Fermi level, making this system topologically non-trivial with $\mathbb{Z}_2 = 1$.

In summary, a two-dimensional topological insulator exhibits gapless spin-momentum locked edge states, which are protected against disorder by time-reversal symmetry. Therefore, at low temperature, the transport from charge and spin are regarded as dissipationless. These states can be distinguished from a trivial band insulator by the $\mathbb{Z}_2$ invariant.

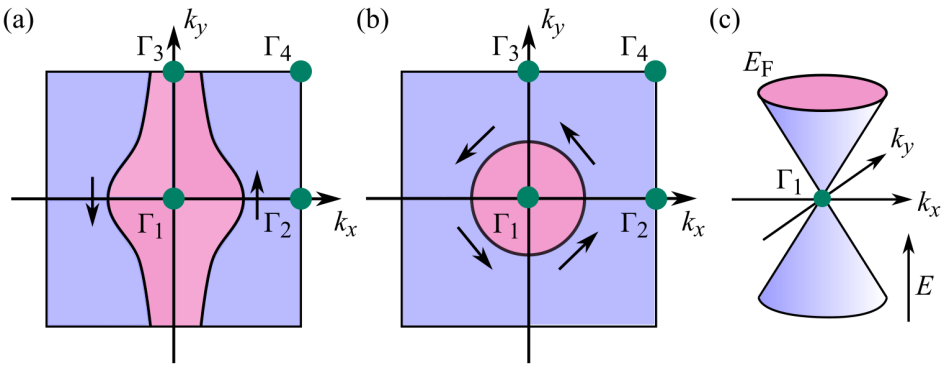

Figure 4: Energy spectra of (a) a weak and (b) a strong topological insulator in the first Brillouin zone. $\Gamma_{1,2,3,4}$ depict the TR invariant points, which are referred to as Dirac points. The characterization depends on the number of Dirac points which are intersected by the Fermi level E_F. (c) Simplest strong TI with only one Dirac point enclosed by the Fermi surface. Picture according to Ref. [30].

2.1.3 Three-dimensional Topological Insulator

In 2007, three groups (L. Fu and C. L. Kane [39]; J. E. Moore and L. Balents [40] and R. Roy [41]) independently predicted that topologically protected states can also be realized in three-dimensions. Although the topologically protected states are not edge currents but conducting surface states enclosing the insulating bulk, the above discussed features can be applied to the 3D case.

One difference between the 2D and the 3D cases is that for the characterization of a 3D TI four $\mathbb{Z}_2$ topological invariants $(v_0; v_1 v_2 v_3)$ are necessary. This can be understood by taking a closer look at the surface Brillouin zone, depicted in Fig. 4(a) and (b). There, the Brillouin zone has four TR invariant points ($\Gamma_{1,2,3,4}$), where the surface states are Kramer-degenerated. These points are depicted as green points and are referred to as Dirac points. Similar to the 2D case, the characterization depends on the number of Dirac points, which are intersected by the Fermi surface. If an even number of Dirac points is encircled at every physical surface (see Fig. 4(a)), the system is topologically trivial with the topological invariant $v_0 = 0$.

If the Fermi surface encloses an odd number of Dirac points the system is topologically non-trivial and is labelled as a 3D topological insulator. This system is characterized by $v_0 = 1$. The other three topological invariants ($v_{1,2,3}$) can be interpreted as the Miller indices of the reciprocal lattice [39]. In Fig. 4(b) and (c) the simplest case with only one enclosed Dirac point is shown. The black arrows represent the spin-direction. According to Kramer's theorem, the spin has to have opposite direction at $\boldsymbol{k}$ and $-\boldsymbol{k}$. Therefore, it winds around the Fermi surface. Although carriers can scatter between trivial and non-trivial surface states, these states cannot vanish due to their protection by topology [29]. In other words, the metallic behaviour of the surface states is robust against disorder.

Although the existence of quantum spin Hall states was first proposed in graphene, the realization of this states in this material turned out to be unrealistic due to its extremely small spin-orbit-induced band gap [42, 43]. However, in 2006, Bernevig *et al.* [16] predicted QSH states in semiconductor quantum wells (QW) with inverted band structure, followed in 2007 by the first realization in HgTe-based QWs by König *et al.* [17]. Almost at the same time, the first 3D system was established in $Bi_{1-x}Sb_x$ (2008) [44], followed by Bi_2Se_3 (2009) [45], Bi_2Te_3 (2009) [46], and HgTe (2011) [18].

2.1.4 Band Structure of Mercury Telluride

To understand the origin of topological states in mercury telluride, a closer look has to be taken at the band structure of this material. HgTe is a zincblende II-VI material and forms its bonds between the $6s$ electrons from the mercury atoms and the $5p$ electrons from the telluride atoms. In contrast to most semiconductors where the s-type Γ_6 band lies above the p-type Γ_8 band, the band ordering of HgTe is inverted due to strong relativistic effects [14, 15]. A schematic demonstration of the formation of the band structure of HgTe compared to those in cadmium telluride (CdTe) is given in Fig. 5(a) and (b) respectively.

In the initial system (H_{int}), the energy gap has approximately the same value for HgTe and CdTe. While a consideration of the Darwin term (H_{D}) and the

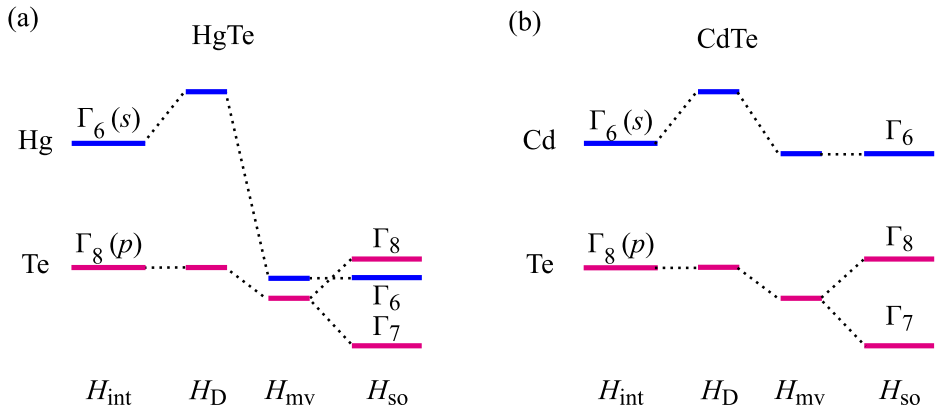

Figure 5: Schematic description of the main energy band formation at the Γ point for (a) HgTe and (b) CdTe. From left to right, the influence of the Darwin term (H_{D}), the mass velocity correction (H_{mv}), and the spin-orbit interaction (H_{so}) are considered. Due to the strong influence of the mass velocity correction, HgTe exhibits an inverted band ordering, whereas CdTe shows a trivial one. Picture according to Refs. [14, 15].

mass velocity term (H_{mv}) only results in a small displacement of the Γ_6 and Γ_8 bands in CdTe, the band ordering of HgTe is affected much more strongly. Due to the large atomic mass of Hg, the mass velocity correction is so strong that the Γ_6 is lowered to almost the same value as the Γ_8 band. The spin-orbit interaction described by H_{so} then splits the three-times-degenerated Γ_8 band in a double-degenerated Γ_8 and a Γ_7 band. In HgTe, this shifts the s-type Γ_6 below the p-type Γ_8 state and inverts the two bands.

In Fig. 6, the resulting energy spectrum of (a) bulk HgTe and (b) bulk CdTe is depicted near the Γ point. While CdTe exhibits a band ordering typical for a semiconductor, with the Fermi level between the Γ_6 and the Γ_8 band, the Fermi level in HgTe lies between the heavy hole (HH_1) and the light hole (LH_1) band. As these two bands are degenerated at $k = 0$ the system has no energy gap. Therefore, bulk HgTe is a topological semimetal [16, 47]. To realize a topological insulator, the degeneration of the LH_1 and HH_1 band has to be lifted. In the three-dimensional case, this can be done by growing a thin film of HgTe on a material with a slightly different lattice constant (e.g. CdTe). Due to the arising compressive strain, an energy gap opens and an insulating

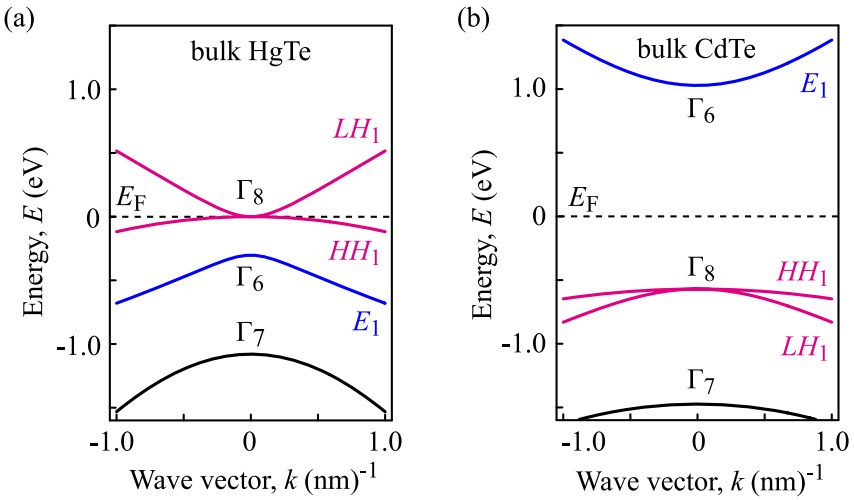

Figure 6: Band structure of (a) bulk HgTe and (b) bulk CdTe near the Γ point. HgTe represents a topological semimetal with an inverted band ordering and no energy gap between the valence (HH_1) and the conduction bands (LH_1). By contrast, bulk CdTe is a trivial semiconductor. Picture according to Ref. [16].

bulk arises [38, 48]. In the two-dimensional case, the degeneration can be lifted due to confinement effects in quantum wells [49].

In the case of a HgTe quantum well with a barrier material with trivial band order, e.g. CdTe, the strength of the spin-orbit interaction can be tuned by changing the thickness of the well (see Fig. 7(a)) [16]. For a thin QW layer, the ordering of the trivial barrier dominates (E_1 above HH_1), whereas for thick QW layers, HgTe dominates and the QW spectrum is inverted (HH_1 above E_1), as shown in Fig. 7(a) and (b) respectively. This means that at some point, the two bands have to intersect and a topological quantum phase transition from a normal to an inverted band ordering occurs [17]. This quantum well thickness is called critical thickness (d_c). At this point, the dispersion of the two bands becomes linear and can be described by the effective Dirac Hamiltonian for massless particles [16].

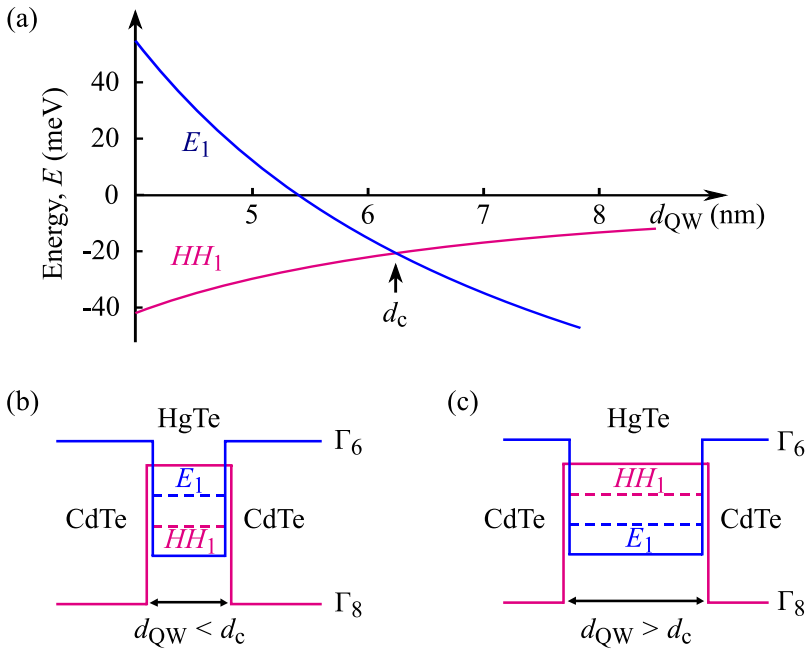

Figure 7: (a) Energies of E_1 (blue) and HH_1 (red) in dependence on the quantum well thickness d_{QW}. At $d_{\mathrm{QW}} = d_{\mathrm{c}}$ the two bands cross and a quantum phase transition from the (b) trivial ($d_{\mathrm{QW}} < d_{\mathrm{c}}$) to (c) the topological one ($d_{\mathrm{QW}} > d_{\mathrm{c}}$) occurs. Picture according to Ref. [16].

In contrast to a 2D TI, the Dirac cones in a quantum well with critical width are formed by the following four states [16, 23]:

$$\begin{aligned}
|E1,+1/2\rangle &= f_1(z)\,|\Gamma_6,+1/2\rangle + f_4(z)\,|\Gamma_8,+1/2\rangle\,,\\
|H1,+3/2\rangle &= f_3(z)\,|\Gamma_8,+3/2\rangle\,,\\
|E1,-1/2\rangle &= f_1(z)\,|\Gamma_6,-1/2\rangle + f_4(z)\,|\Gamma_8,-1/2\rangle\,,\\
|H1,-3/2\rangle &= f_3(z)\,|\Gamma_8,-3/2\rangle\,,
\end{aligned} \tag{5}$$

where $f_1(z)$, $f_3(z)$ and $f_4(z)$ are envelope functions, z is the growth direction, and $|\Gamma_6,\pm1/2\rangle$, $|\Gamma_8,\pm1/2\rangle$ and $|\Gamma_8,\pm3/2\rangle$ are the basis functions of the Γ_6 and the Γ_8 bands. These states are degenerated at $k = 0$. For $k \neq 0$, the states mix and are coupled by an effective Hamiltonian. This means that although

these states exhibit a Dirac-like dispersion, the spin-up and spin-down bands are formed by a mixture of the states of Eqs. (5).

In general, in HgTe QWs, it is possible to realize systems with a normal parabolic, linear (Dirac-like), and inverted band structures. As already mentioned, Bernevig *et al.* [16] proposed that inverted band structures provide a way to realize topologically protected states. The QSH states arise at the boundary between the inverted (topologically non-trivial) and a normal (topologically trivial) materials, as the band gap has to be closed (see Chap. 2.1.2). Moreover, in HgTe films, it is possible to realize 3D TI surface states (see Chap. 2.1.3). Therefore, HgTe is the perfect candidate for the investigation of this novel class of material.

2.2 Photogalvanic Effects

In the framework of this thesis, HgTe systems are investigated by means of photogalvanic spectroscopy. This effect occurs by definition due to inhomogeneities in neither the optical excitation nor in the sample. Instead, the *dc* electric current arises by a carrier redistribution in momentum space or in energy [20]. Here, a brief introduction to the basic physic behind this effect and the well-developed model for conventional 2D QWs is given.

Phenomenologically, the photogalvanic effect (PGE) can be described in terms of the squared *ac* electric field $\boldsymbol{E}$ of the terahertz (THz) radiation. The lowest, non-vanishing term of the generated current density $\boldsymbol{j}$ has the form [50]:

$$j_\lambda = \sum_{\mu,\upsilon} \chi_{\lambda\mu\upsilon} E_\mu E_\upsilon^*, \tag{6}$$

$$E_\mu E_\upsilon^* = \{E_\mu E_\upsilon^*\} + [E_\mu E_\upsilon^*], \tag{7}$$

with

$$\{E_\mu E_\upsilon^*\} = \frac{1}{2}(e_\mu e_\upsilon^* + e_\upsilon e_\mu^*) \text{ and } [E_\mu E_\upsilon^*] = \frac{1}{2}(e_\mu e_\upsilon^* - e_\upsilon e_\mu^*). \tag{8}$$

The total photogalvanic current can then be rewritten as:

$$j_\lambda = \sum_{\mu,\upsilon} \chi_{\lambda\mu\upsilon} \{E_\mu E_\upsilon^*\} + \sum_{\mu,\upsilon} \chi_{\lambda\mu\upsilon} [E_\mu E_\upsilon^*], \tag{9}$$

where the first term on the right-hand side corresponds to the linear photogalvanic effect and the second term to the circular photogalvanic effect, excited by linearly and circularly polarized radiations respectively. The linear PGE is only allowed in non-centrosymmetric media of piezoelectric crystals, where non-zero components of the third-rank tensor $\chi_{\lambda\mu\upsilon}$ exist. The circular PGE can only occur in gyrotropic media, where a coupling between an axial A_m and a polar vector P_l via a second-rank pseudo-tensor M_{lm} is allowed [50].

The circular PGE can be further simplified by reducing $\chi_{\lambda\mu\upsilon}$ to a real second-rank pseudo-tensor $\gamma_{\lambda\rho}$ [50]:

$$\sum_{\mu,\upsilon} \chi_{\lambda\mu\upsilon}[E_\mu E_\upsilon^*] = \sum_{\rho} \gamma_{\lambda\rho} i(\boldsymbol{E} \times \boldsymbol{E^*})_\rho = \sum_{\rho} \gamma_{\lambda\rho} \hat{e}_\rho E^2 P_{\mathrm{circ}}, \tag{10}$$

where P_{circ} is the degree of the circular polarization of light and $\hat{\boldsymbol{e}} = \boldsymbol{q}/q$ is the unit vector pointing in the propagation direction of light. The pseudo-tensor $\boldsymbol{\gamma}$ strongly depends on the symmetry of the investigated material. In point-groups with low symmetry like the C_s-group, a photocurrent generation is even allowed for normal incidence of light. For a QW with C_s symmetry, the currents flowing in x- and y-directions are then given by [51]:

$$\begin{aligned} j_x &= (\gamma_{xy'} \hat{e}_{y'} + \gamma_{xz'} \hat{e}_{z'}) E_0^2 P_{\mathrm{circ}}, \\ j_{y'} &= \gamma_{y'x} \hat{e}_x E_0^2 P_{\mathrm{circ}}. \end{aligned} \tag{11}$$

For normal incidence, where $\hat{e}_x = \hat{e}_{y'} = 0$ and $\hat{e}_{z'} = 1$, the current flows in x-direction, which is parallel to the $[1\bar{1}0]$-crystal direction.

Similar to the phenomenological theory, the microscopic picture of the current generation due to the circular PGE strongly depends on the symmetry of the investigated material and the polarization of the incident radiation [50]. As an example, here a microscopic model of the circular PGE based on direct inter-subband excitation in n-type QWs is briefly introduced. This is done for the situation of a C_s point group [50, 52]. In such a system, the spin-orbit interaction adds an additional term $\mathcal{H}_{\mathrm{so}}$ to the Hamiltonian $\mathcal{H}$, which splits the otherwise degenerated band in $\boldsymbol{k}$-space:

$$\mathcal{H} = \frac{\hbar^2 k^2}{2m^*} + \mathcal{H}_{\mathrm{so}}, \tag{12}$$

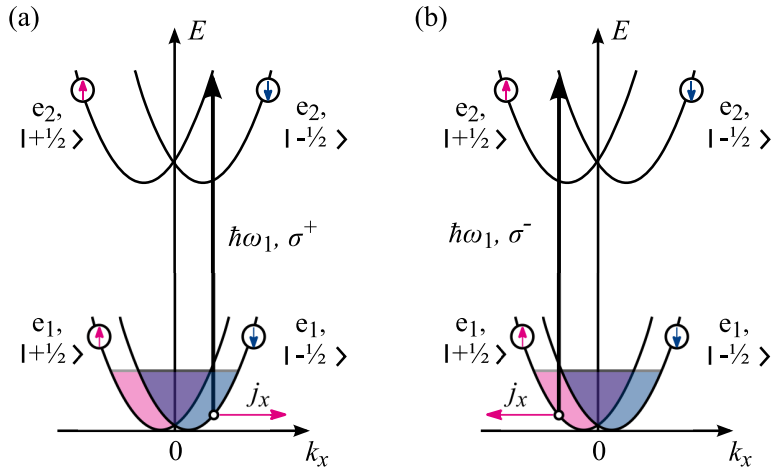

Figure 8: Microscopic picture of the circular PGE based on direct intersubband excitation in n-type QWs with low symmetry. Excitation with (a) right- (σ^+) and (b) left-handed (σ^-) circularly polarized radiation induces direct spin-flip transitions between the subbands e_1 and e_2 of the conduction bands. For right-handed circularly polarized radiation, only spin-flip transitions between the e_1 states with $s = -1/2$ and the e_2 states with $s = +1/2$ are possible. A change of the helicity mirrors the picture and switches the sign of the current. Picture has been adapted from Ref. [50].

where m^* is the effective mass of the carriers. The $\boldsymbol{k}$-linear term of the spin-orbit interaction is given by:

$$\mathcal{H}_{\rm so} = \sum_{\mu,\lambda} \beta_{\mu\lambda}\sigma_\mu k_\lambda, \tag{13}$$

where $\beta_{\mu\lambda}$ is a second-rank pseudo-tensor and σ_μ are the Pauli matrices. In Fig. 8, the splitting of the two levels e_1 and e_2 is shown. The spin-orbit interaction splits the levels into spin-sublevels with spin components $s = \pm 1/2$ along the growth direction z'. Due to the optical selection rules, only direct transitions between the subband e_1 with spin $s = -1/2$ and e_2 with $s = +1/2$ are allowed for right-handed circularly polarized radiation (see Fig. 8(a)). This leads to an imbalance of the electron distribution in the momentum space and, therefore, to an electric current in x-direction. By changing the polarization from the right- to left-handed one, the transition can only occur between the

e_1 level with spin $s = +1/2$ and e_2 level with $s = -1/2$ states and the current direction reverses, as shown in Fig. 8(b).

2.3 Cyclotron Resonance

A good tool to enhance the generated photocurrents is cyclotron resonance (CR), which results in a resonant absorption of radiation from electrons or holes in a static and uniform magnetic field. As shown below, CR provides a novel access to information about the band structure of the investigated material.

In a classical picture, free carriers with the velocity $\boldsymbol{v}$ are deflected due to the Lorentz force $\boldsymbol{F}_{\mathrm{L}} = q[\boldsymbol{v} \times \boldsymbol{B}]$ and start to move on circular orbits normal to the magnetic field $\boldsymbol{B}$ with a cyclotron frequency of [53]:

$$\omega_{\mathrm{CR}} = \frac{qB}{m_{\mathrm{CR}}}, \tag{14}$$

where q is the charge of the carrier, which is equal to $-e$ for electrons and $+e$ for holes and m_{CR} is the cyclotron mass. Radiation with a frequency exactly matching the angular frequency of the electrons ($\omega_{\mathrm{rad}} = \omega_{\mathrm{CR}}$) are absorbed with a resonant behaviour. The resonant absorption of radiation can only occur if most carriers can at least perform one whole cycle before being scattered. Using the momentum relaxation time τ, this requirement is given as $\omega_{\mathrm{CR}} \gg 1/\tau$ [54].

In $\boldsymbol{k}$-space, the electrons move on an orbit with constant energy in a plane normal to the magnetic field [53]. For electrons with Fermi energy this trajectory is also called Fermi surface, which is a sphere in the case of an ideal parabolic band structure. Due to the Fermi surface symmetry, the electrons move on closed circles with a period:

$$\widetilde{T} = \frac{\hbar^2}{eB}\frac{dS}{dE}, \tag{15}$$

where $\frac{dS}{dE}$ is the energy-dependence of the area of the closed orbit in $\boldsymbol{k}$-space. With this relation the cyclotron frequency can be rewritten to [55, 56]:

$$\omega_{\mathrm{CR}} = \frac{2\pi}{\widetilde{T}} = \frac{2\pi eB}{\hbar^2}\frac{dE}{dS}. \tag{16}$$

For a free electron moving on a circle ($S = \pi \boldsymbol{k}^2$) and an energy of $E = \frac{\hbar^2 k^2}{2m*}$ (parabolic dispersion) Eq. (14) changes to:

$$\omega_{\mathrm{CR}} = \frac{eB}{m^*}, \tag{17}$$

where m^* is the effective mass of the electron. Therefore, CR experiments allow the determination of the effective mass of electrons and holes in semiconductor structures [53].

The exact magnetic field position and the quantity of the absorbed light strongly depend on the polarization state of the radiation. For circularly polarized light, the absorbed power P_{circ} is given by [54, 57]:

$$P_{\mathrm{circ}} = \frac{\sigma_0 E_0^2}{(\omega \pm \omega_{\mathrm{CR}})^2 \tau^2 + 1}, \tag{18}$$

with the electric field E_0 of the polarized electro-magnetic wave and the *dc* conductivity $\sigma_0 = \frac{nq^2\tau}{m^*}$, where q is the charge of the carrier. The sign of the denominator of Eq. (18) stands for right- ("+") and left- ("−") handed circularly polarized radiation. As linearly polarized radiation can be considered as a superposition of both circular polarizations, the absorbed power P_{lin} adds up to:

$$P_{\mathrm{lin}} = \frac{1}{4}\sigma_0 E_0^2 \left[\frac{1}{(\omega - \omega_{\mathrm{CR}})^2 \tau^2 + 1} \frac{1}{(\omega + \omega_{\mathrm{CR}})^2 \tau^2 + 1} \right]. \tag{19}$$

For electrons, an absorption occurs on the positive magnetic field side for right-handed polarized and on the negative side for left-handed polarized radiation. This situation is reversed for a system with holes as principal carriers. For linear polarized radiation, the resonance appears for both carrier types on both magnetic field polarities.

Apart from the classical approach, there is also a quantum mechanical model to describe cyclotron resonance. At low temperature ($k_{\mathrm{B}}T < \hbar\omega_{\mathrm{CR}}$), a constant magnetic field applied perpendicularly to the quantum well plane splits the energy spectrum into Landau levels. The energy of the l-th Landau level of a system with parabolic dispersion is defined as [55, 58, 59]:

$$E_l(k_z) = \hbar\omega_{\mathrm{CR}} \left(l + \frac{1}{2} \right) + \frac{\hbar^2 k_z^2}{2m^*}, \tag{20}$$

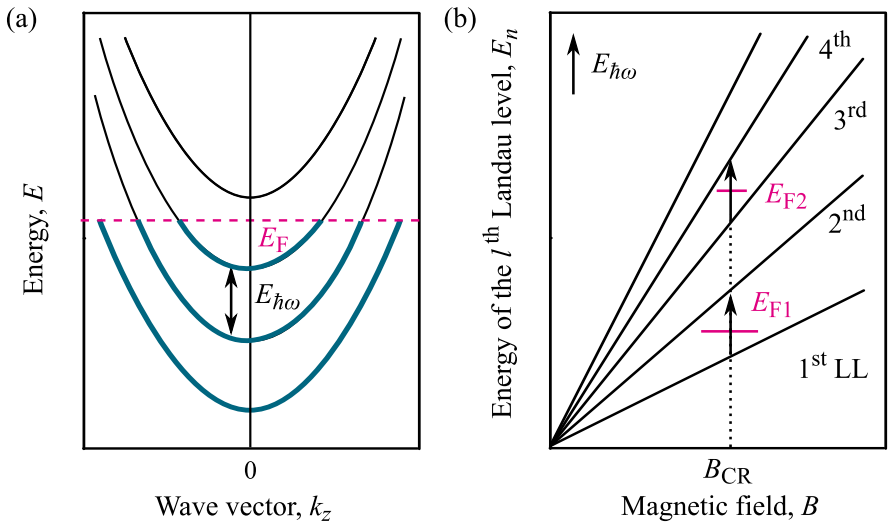

Figure 9: Schematic illustration of Landau level splitting for a 3D system with parabolic dispersion. Energy E of the Landau level, depending on (a) the wave vector k_z and (b) on the magnetic field B, is depicted. The black arrows indicate transitions between two Landau levels with energies $E_{\hbar\omega}$. The resonances stay at a fixed magnetic field value for different Fermi level position B_{CR}. Picture adapted from (a) Ref. [55] and (b) Ref. [58].

with $l \in \mathbb{N}$. From this relation, it can be seen that the Landau levels split equidistantly with an energy difference of $\Delta E_{l,l\pm1} = \pm\hbar\omega_{\mathrm{CR}}$. This is schematically depicted for a 3D system in Fig. 9(a). The cyclotron resonance corresponds to a transition between two neighbouring Landau levels, if the radiation energy exactly fits the energy difference between them. As these levels split equidistantly, only the magnetic field defines the radiation frequency that is absorbed. Therefore, the transitions for both Fermi energy positions $E_{\mathrm{F1,F2}}$, indicated in Fig. 9(b) with black arrows, are at the same magnetic field value B_{CR} for a given radiation energy $E_{\hbar\omega}$, independent of the Fermi level position.

2.4 CR-Enhanced Photocurrents in HgTe QWs

The photogalvanic effect, in combination with cyclotron resonance, is observed in HgTe QWs with parabolic dispersion as well as in QWs with $d_{\mathrm{QW}} \approx d_{\mathrm{c}} = 6.6\,\mathrm{nm}$, where the energy spectrum is expected to be characterized by a linear

one. Here, the main features of CR in both types of quantum wells is summarized. Furthermore, the photocurrent generation, based on the magneto-gyrotropic photogalvanic effect, is outlined briefly. A full study of the data is published in Ref. [23] and Ref. [60].

2.4.1 Parabolic Dispersion

Applying a magnetic field B and THz radiation normal to the surface of a 21 nm HgTe QW sample (under CR-condition), THz radiation-induced photosignals with a strong Lorentzian-like enhancement arise, as shown in Fig. 10(a). The positions B_{CR} of these resonances depend on the frequency of the applied radiation (not shown) and the effective mass of the carriers. These relations are given by Eq. (17). Moreover, the resonances show a strong helicity-dependence, where peaks at one magnetic field polarity are more pronounced for a given helicity. This is in full accordance with the theory and the dependencies can be described with Eq. (18). In Fig. 10(b), measurements for two different states of the sample are shown. A change of the carrier density has almost no influence on the positions of the resonances and only the peak amplitudes vary. All the mentioned features can also be found in transmission measurements, as shown in Fig. 10(c), and are in full accordance with the theory given in Sec. 2.3.

In Ref. [23], it is shown that the current arises due to the magnetic photogalvanic effect. The theory describes the dependencies of the induced current on the applied magnetic field direction and the radiation polarization state with respect to the crystallographic axes. In a linear approximation of the magnetic field strength $\boldsymbol{B}$, the photocurrent density $\boldsymbol{j}$ for gyrotropic materials is given by [50, 61]:

$$j_\alpha = \sum_{\beta,\gamma,\delta} \phi_{\alpha\beta\gamma\delta} B_\beta \{E_\gamma E_\delta^*\} + \sum_{\beta,\gamma} \mu_{\alpha\beta\gamma} B_\beta \hat{e}_\gamma E_0^2 P_{\mathrm{circ}}, \tag{21}$$

where E_γ are components of the complex amplitude of the radiation electric field $\boldsymbol{E}$, $\hat{\boldsymbol{e}}$ is the unit vector pointing in the direction of the light propagation, and the Greek indices are Cartesian coordinates. The term on the right-hand side, including the fourth-rank pseudo-tensor $\boldsymbol{\phi}$, which is symmetric in the last two indices, is induced by linear or unpolarized radiation. The photocurrents

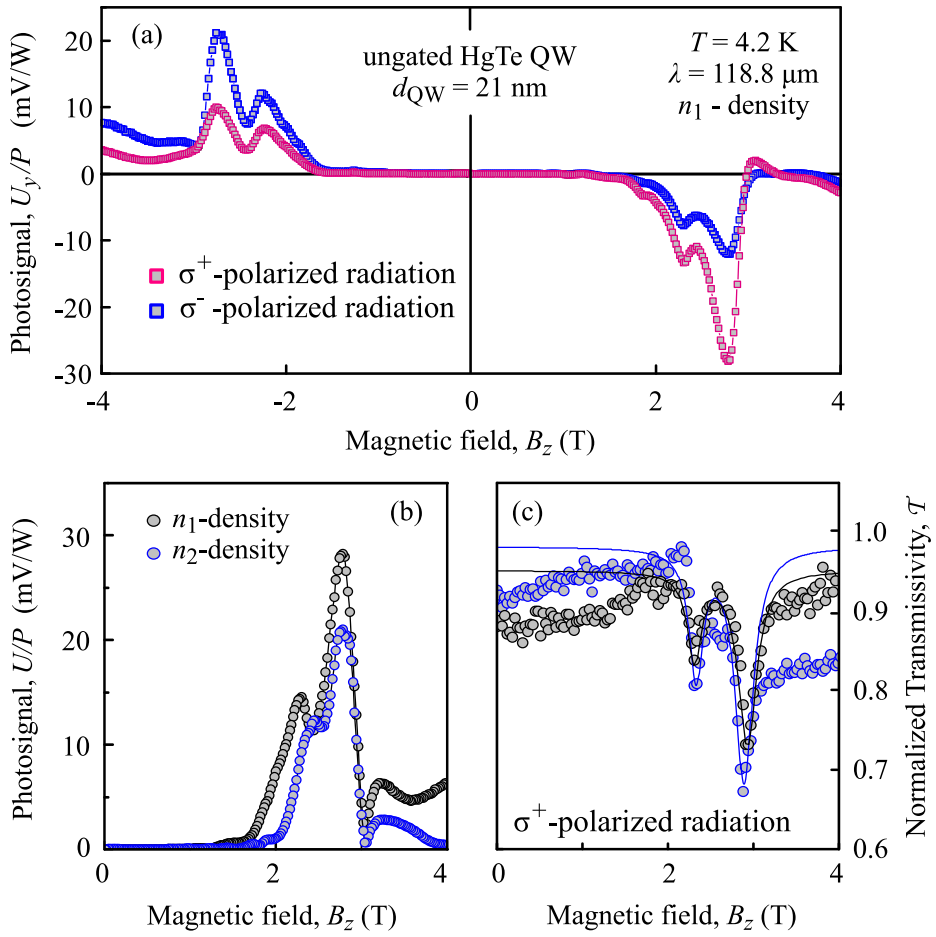

Figure 10: (a) Normalized photosignal U_y/P as a function of the magnetic field B_z for a 21 nm HgTe QW. The radiation and the magnetic field are applied perpendicularly to the surface of the sample. For right-handed (σ^+, red rectangle) circularly polarized radiation, the main peak is more pronounced at the positive magnetic field side. By switching to left-handed (σ^-, blue rectangle) circularly polarized radiation, the main peak appears at a negative magnetic field value. (b) Normalized photosignal magnitude $U/P = \frac{(U_x+U_y)/2}{P}$ and (c) transmissivity $\mathcal{T}$ for two different carrier densities, $n_1 = 18 \cdot 10^{10}\,\mathrm{cm}^{-2}$ and $n_2 = 24 \cdot 10^{10}\,\mathrm{cm}^{-2}$.

depending on the circularly polarized radiation are described by the second term of Eq. (21) containing the third-rank tensor $\boldsymbol{\mu}$.

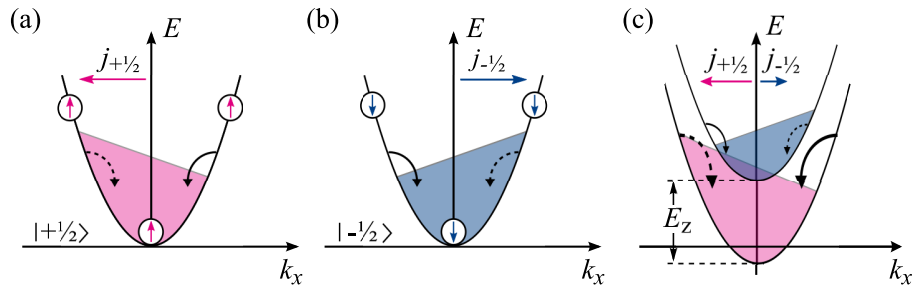

Figure 11: Semi-classical picture of the current generation due to the magneto-gyrotropic PGE. Asymmetry in the relaxation process of a homogeneously heated electron gas for the (a) spin-up and (b) spin-down subband. Curved arrows indicate the different scattering probabilities for electrons with positive and negative $\boldsymbol{k}$. (c) Model of the magneto-gyrotropic effect, where the spin-up subband is preferably occupied due to the Zeeman splitting and so an electric net current arises. Picture according to [50, 61].

Apart from the phenomenological theory the magneto-gyrotropic PGE can be expressed in a semi-classical microscopic picture. This picture is valid for moderate magnetic fields, when the system is not in the quantum Hall regime. For a fully quantized system this picture becomes more complicated and a microscopic description is still outstanding. In the semi-classical regime the homogeneous Drude-like absorption of THz radiation, together with a spin-dependent asymmetry of the electron scattering, can lead to an imbalance in the carrier distribution in momentum space. In gyrotropic media, such a spin-dependent term arises in the electron-phonon interaction due to the spin-orbit interaction and can be written as [50, 61, 62]:

$$W_{kk'} = W_0 + \sum_{\alpha\beta} W_{\alpha\beta}\sigma_\alpha(k_\beta + k'_\beta), \tag{22}$$

where the first term of the sum is the conventional spin-independent scattering W_0 and the second term is the spin-dependent scattering. Here, $\boldsymbol{W}$ is a second-rank pseudo-tensor, σ_α represents the Pauli matrices, and $\boldsymbol{k}$ and $\boldsymbol{k'}$ are the wave vectors before and after a scattering event.

The spin-dependence of the electron-phonon interaction results in different energy relaxation rates for electrons at positive and negative $\boldsymbol{k}$. This effect is depicted in Fig. 11(a) and (b) for the spin-up and -down bands in a parabolic

energy dispersion respectively. The black curved arrows indicate the different relaxation rates in momentum space within one subband. Independent of the energy dispersion, this scattering asymmetry causes an imbalance in the carrier distribution between positive and negative $\boldsymbol{k}$-states and therefore, electron fluxes $\boldsymbol{j}_{\pm 1/2}$ arise. The fluxes for the spin-up band ($\boldsymbol{j}_{+1/2}$) and the spin-down band ($\boldsymbol{j}_{-1/2}$) have the same strength, but different direction, since the asymmetric part of the scattering amplitude depends on the spin-orientation. Therefore, no electric current is generated. Only a pure spin-current arises, which separates the electrons with different spins:

$$\boldsymbol{j}_s = \frac{1}{2}(\boldsymbol{j}_{+1/2} - \boldsymbol{j}_{-1/2}). \tag{23}$$

By applying a magnetic field $\boldsymbol{B}$, the two subbands split energetically due to the Zeeman effect, as shown in Fig. 11(c). The energy difference of the subbands is given by:

$$\Delta E_Z = g\mu_\mathrm{B}\boldsymbol{B}, \tag{24}$$

where g is the effective Landé factor and μ_B is Bohr's magneton. This leads to a different equilibrium population for the two subbands and thus to different flux strengths (e.g. $\boldsymbol{j}_{+1/2} > \boldsymbol{j}_{-1/2}$). Now, the pure spin-current is converted into a detectable charge current [61]:

$$\boldsymbol{j_Z} = -e\frac{\Delta E_z}{E_\mathrm{F}}\boldsymbol{j_s} = 4eS\boldsymbol{j_s}, \tag{25}$$

where $S = \frac{1}{2}(n_{+1/2} - n_{-1/2})/(n_{+1/2} + n_{-1/2})$ is the magnitude of the average spin, with the carrier density $n_\pm$ of the spin-up and spin-down subbands. In equilibrium, $\boldsymbol{S}$ is given by:

$$\boldsymbol{S} = -\frac{g\mu_\mathrm{B}\boldsymbol{B}}{4\bar{\varepsilon}}, \tag{26}$$

where $\bar{\varepsilon}$ is the characteristic electron energy, which is equal to the Fermi energy E_F for a degenerate 2D electron gas.

2.4.2 Dirac-like Dispersion

THz radiation-induced photosignals with strong Lorentzian-like enhancement can also be found in samples with a linear dispersion by applying a magnetic field, as shown in Fig. 12(a). Here, three different carrier densities (p_1, n_1, and n_2) are depicted. Similar to the results obtained in the sample with parabolic energy dispersion, the resonance positions of the photosignal $B_{\mathrm{CR}}^{\mathrm{PGE}}$ show a strong coincidence with the ones found in transmission measurements $B_{\mathrm{CR}}^{\mathrm{TM}}$, as depicted in Fig. 12(b). Furthermore, the resonances exhibit a considerable dependence on the radiation helicity and the radiation frequency. All these features are already observed in the QWs with parabolic dispersion.

The main difference between the results obtained in the QWs with 6.6 nm thickness and the ones with parabolic dispersion is the dependence of the peak position on the carrier density in the samples with critical thickness. By a change of the carrier density from $p_1 = 1.5 \cdot 10^{10}\,\mathrm{cm}^{-2}$ to $n_1 = 3.4 \cdot 10^{10}\,\mathrm{cm}^{-2}$, the main resonance not only shifts from the negative magnetic field side to the positive magnetic field side, but appears also at a almost two times higher value. A further increase in the carrier density to $n_2 = 11 \cdot 10^{10}\,\mathrm{cm}^{-2}$ shifts the resonance to an even higher magnetic field value.

Apart from the characteristic dependence of B_{CR} on the carrier density, the resonances appear at much smaller magnetic field values then the ones obtained in previous studies of HgTe/HgCdTe QWs, with a parabolic dispersion. In 6.6 nm QWs, the resonance positions range from $B_{\mathrm{CR}} = 0.38 - 1.20\,\mathrm{T}$ for a wavelength of $\lambda = 118\,\mu\mathrm{m}$. Similar values are found in photoconductivity measurements in Ref. [63], done in $d = 6.4$ and 6.6 nm Hall-bar structures under CR and in transmission measurements in Ref. [64].

As before, the origin of the photocurrent can be attributed to the magneto-gyrotropic PGE, which can be adopted easily to Dirac fermions in a system at critical thickness [23]. By taking into account the effect of CR and assuming that the magnetic field only splits the states due to the Zeeman effect but does not change the scattering mechanism, the current magnitude can be estimate by [23]:

$$|\boldsymbol{j}| = \frac{2ev \sin 2\theta}{\sqrt{2} E_{\mathrm{F}} \omega_{\mathrm{CR}}} \xi I S \eta, \tag{27}$$

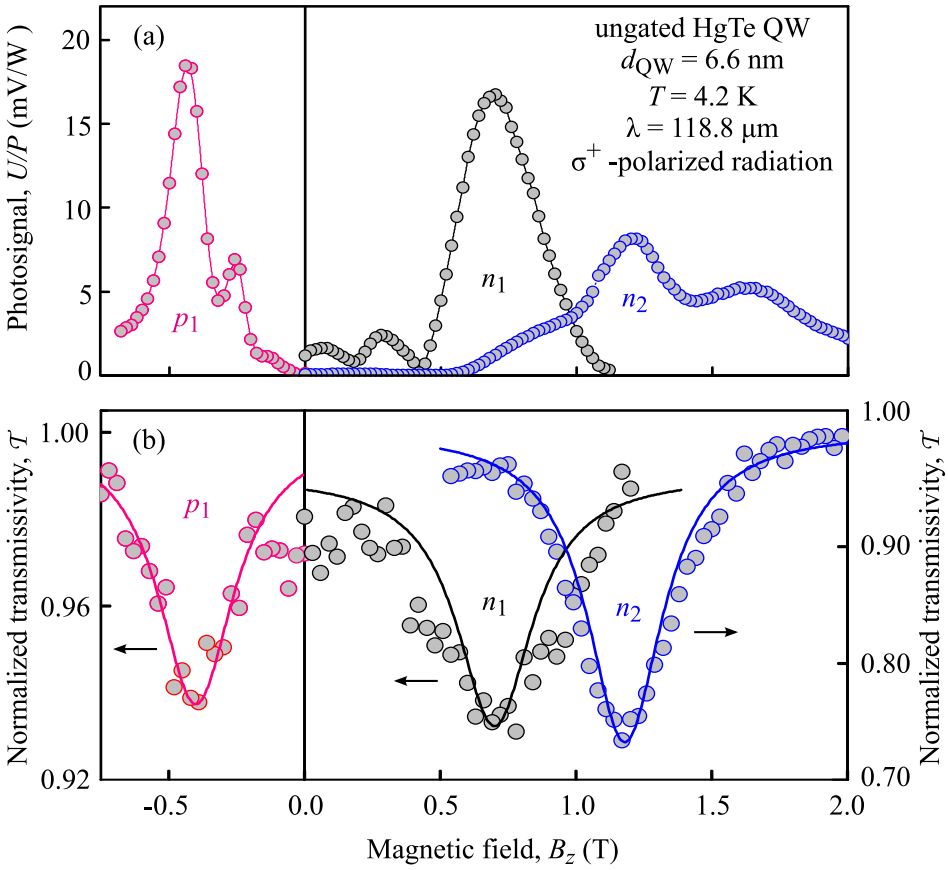

Figure 12: (a) Normalized photosignal magnitude $U/P = \frac{(U_x+U_y)/2}{P}$ as a function of the magnetic field for three different carrier states of the 6.6 nm sample. Only the photosignals in the vicinity of the resonance are shown. (b) Magnetic-field-dependence of the transmissivity $\mathcal{T}$ for right-handed circularly polarized radiation, see left scale for the p_1- and n_1-states and right scale for the n_2-state. Solid lines are Lorentzian fits.

where ξ represents the spin-orbit interaction, S is the magnitude of the averaged spin given in Eq. (26), and η takes into account the increased absorbance in the vicinity of CR:

$$\eta = \frac{2e^2 E_F}{c\hbar^2 n_\omega} \frac{\tau_p}{1+(\omega-\omega_{CR})^2\tau_p^2}, \tag{28}$$

Herein, n_ω is the refractive index and τ_p is the momentum relaxation time. Note that these equations are only accurate for a linear energy dispersion. For the parabolic one, the main features remain and only the prefactors change.

3 Experimental Methods and Techniques

This chapter is dedicated to the experimental methods and techniques used in this work. To get a better understanding of the studies carried out, herein a brief introduction to the experimental setup is given. This includes an illustration of the used continuous wave CO_2 far-infrared laser system. Then, the different measurement setups are outlined, namely the setups for the magneto-transport, photosignals (photovoltage and photocurrent), and radiation transmission. Finally, all investigated samples are specified and the structure and characteristics of the HgTe QWs and the HgTe films are introduced.

3.1 Experimental Setup

First, a brief overview of the generation of the THz radiation by a continuous wave (cw) CO_2 far-infrared (FIR) laser system and the optical path, including an optical cryostat with a superconducting magnet, is given.

The monochromatic cw radiation used in this work is produced by a molecular gas laser[1], which is optically pumped by a CO_2 laser[2]. In Fig. 13, an overview of the whole CO_2 FIR laser system is depicted. The CO_2 laser emits discrete spaced lines due to rotational-vibrational transitions of the P- and R-branches of the CO_2 molecule [50, 65]. In more detail, the two possible transitions between the vibrational states of the CO_2 molecule with centre wavelengths of $\lambda = 9.6\,\mu\text{m}$ and $\lambda = 10.6\,\mu\text{m}$ are split further into many rotational states. Therefore, the CO_2 laser is line-tunable around these two centre wavelength. This middle-infrared (MIR) radiation, with a power in the order of $P = 35$ W, is then used to pump the FIR laser.

To enable this pumping, the radiation produced by the CO_2 laser is deflected by two planar mirrors and coupled into a second molecular gas laser via a zinc selenide (ZnSe) lens through a ZnSe Brewster window and a gold-coated planar steel mirror. The Brewster angle $\phi_B = \arctan(n_\omega)$, where n_ω is the refractive index of the window, ensures that only the parallel components of

[1] $295FIR$, Edinburgh Instruments, Livingston, UK
[2] $PL5$, Edinburgh Instruments, Livingston, UK

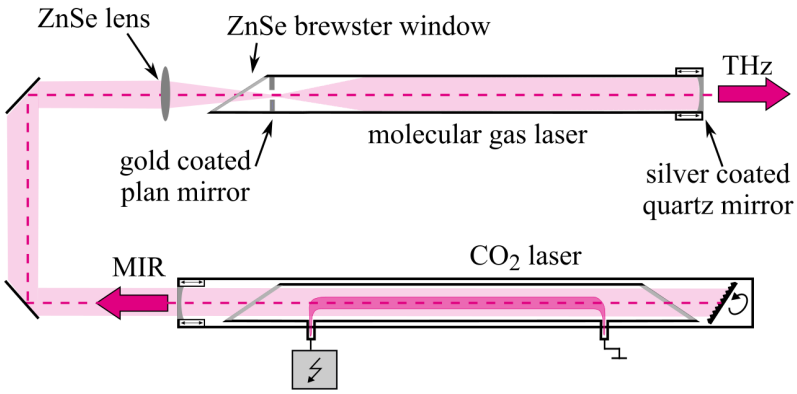

Figure 13: Schematic picture of the used laser system, producing high-power cw terahertz radiation. An electrical pumped CO_2 laser is used to optically pump a FIR molecular gas laser. The dashed red line represents the optical path. Picture modified from Ref. [66].

the electric field $\boldsymbol{E}$ are transmitted, which results in a horizontally polarized radiation. In the FIR laser resonator, the MIR radiation excites vibrational-rotational transition of a molecule with a permanent electric dipole moment. The subsequent relaxation occurs over pure rotational transition with a laser emission in the FIR range [50, 67].

The exact wavelength of the far-infrared laser radiation depends on the active media used and on the pump energy of the CO_2 laser. With these parameters, the laser system is line-tunable over the whole far-infrared range. In this work, three strong lines are used, which are summarized, together with the used active media, the wavelength λ, the frequency f, the photon energy $E_{\hbar\omega}$, and

FIR active media	λ (μm)	f (THz)	$E_{\hbar\omega}$ (meV)	P (mW)
methanol (CH_3OH)	118	2.54	10.4	60
difluoromethane (CH_2F_2)	184	1.62	6.7	80
formic acid (CH_2O_2)	432	0.69	2.9	20

Table 1: The parameters of the far-infrared laser radiation, including the laser gas (active media) of the FIR laser system, the wavelength λ, frequency f, photon energy $E_{\hbar\omega}$, and power P of the emitted THz radiation.

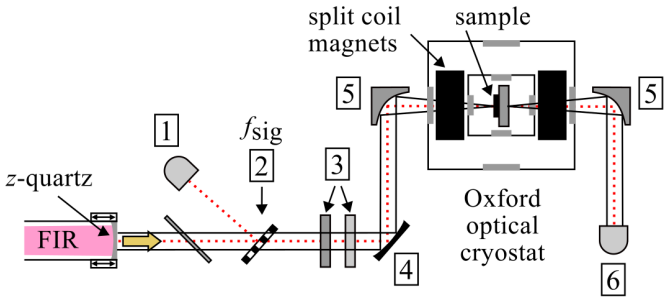

Figure 14: Schematic picture of the radiation path (red, dotted line) including the reference detector (1), optical chopper (2), position of different optical components like a wave plate, a grid or attenuators (3), planar mirror (4), parabolic mirror (5), the optical cryostat, and the transmission detector (6). Picture modified from Ref. [66].

the power P, in Tab. 1. Furthermore, the wavelength and the mode of the radiation can be adjusted with a moveable silver-coated z-cut quartz mirror at the end of the cavity. This output mirror is transparent for the produced THz radiation, but reflects the MIR radiation of the pump laser and ensures a monochromatic output of the laser system. The shape of the outcoupled mode can be monitored with thermal paper or with a pyrometer for temperature detection (Pyrocam).

In Fig. 14, an example of the experimental setup is shown. The dotted red line represents the optical path of the radiation beam. After leaving the FIR laser, the beam is modulated by an optical chopper (2) at frequencies of $f_{\mathrm{sig}} = 400 - 600\,\mathrm{Hz}$ and different optical components like a wave plate, a grid, or attenuators (3). It is then deflected and focused on the sample into an optical cryostat[3] with the help of a planar (4) and a parabolic (5) mirror. The outer windows of this cryostat are covered with black polyethylene sheets, which prevent an illumination of the sample with ambient light.

The sample is mounted in the centre of the cryostat between two superconducting split coil magnets. These magnets allow a generation of a magnetic

[3]Spectromag SM4000-8, Oxford Instruments, Abingdon, UK

field up to ±7 T, normal to the sample surface. Furthermore, the temperature at the sample position can be set and kept at any fixed temperature between $T = 1.8$ K and room temperature with liquid helium, a heater, and the help of a temperature controller. The part of the radiation that is transmitted through the sample and the cryostat is collected by a pyroelectric detector (6).

To reduce the influence of the surrounding electrically noise, Lock-in technique has been used for the measurements of the voltage drops across the sample (for details see Sec. 3.2). In addition, the part of the radiation which is reflected on the optical chopper is used as a reference signal. This reflected signal enables the analysis of the measurement data and a control of the stability of the laser. All mentioned signals, including the voltage drop over the sample, the signal of the transmission (6) and reference (1) detector, as well as parameters like the magnetic field strength, sample temperature, etc., are transmitted via a General Purpose Interface Bus (GPIB) system to a measurement computer, where they are stored for further processing by a LabVIEW program.

3.2 Measurement Setup

After introducing the general laser setup in the previous section, an overview of the different measurement methods is given here. This comprehend the magneto-transport, the measurements of photovoltage and photocurrent obtained by THz radiation, and the transmission of the radiation through the sample.

3.2.1 Measurements of Magneto-Transport

All samples are first characterized with standard magneto-transport. For this type of measurement, the sample are biased with an *ac* voltage in the range of $U_{\mathrm{ac}} = 0.1 - 1\,\mathrm{V}$ over a series resistor of $R_{\mathrm{ac}} = 1 - 10\,\mathrm{M\Omega}$. This results in a current flowing through the sample in the range of $I_{\mathrm{ac}} = 0.01 - 1\,\mu\mathrm{A}$. An exemplary sketch of this setup is depicted in Fig. 15. The change of the resistance in dependence on a magnetic field applied normal to the surface of the sample or in dependence on the gate voltage is determined. Thereafter, the voltage

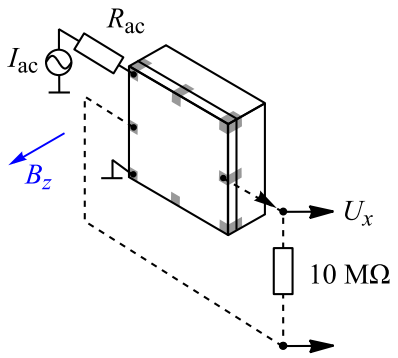

Figure 15: Illustration of the magneto-transport setup. A magnetic field B_z normal to the sample surface and an *ac* current I_{ac} over a load resistor R_{ac} are applied to the sample. The voltage drops in x- or y-direction are measured over a load resistor $R_{load} = 10\,\mathrm{M\Omega}$ via Lock-in technique. From the obtained signals, the Hall and the longitudinal resistance can be obtained.

drop parallel (U_{xx}) and perpendicular (U_{xy}) to the applied current is measured over a $10\,\mathrm{M\Omega}$ load resistor with Lock-in technique. From these signals, the Hall (R_{xy}) and the longitudinal resistance (R_{xx}) can be calculated, using $R = U/I_{ac}$. The obtained traces give information about the characteristics of the investigated sample, e.g. the carrier type and density.

3.2.2 Measurements of THz Radiation-Induced Photosignals

The THz radiation-induced photosignal is measured in an unbiased sample under normal incidence. If necessary, an external magnetic field is applied perpendicular to the sample's surface. The arising photosignal is measured in two orthogonal directions (x- and y-direction) over a load resistor R_L via Lock-in technique. Depending on the ratio between the load resistor and the sample resistance R_{sample}, the signal is measured as either a photovoltage ($R_L \gg R_{sample}$) or a photocurrent ($R_L \ll R_{sample}$). A sketch of the corresponding setup is depicted in Fig. 16.

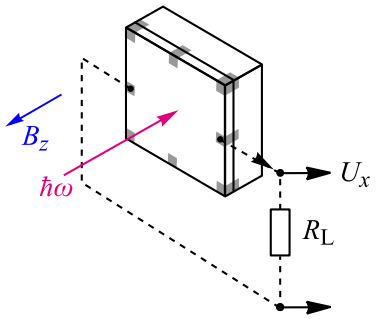

Figure 16: Setup of the photosignal measurement. The THz radiation ($\hbar\omega$) and if required the magnetic field B_z is applied normal to the surface of the sample. Depending on the load resistor R_L, the obtained photosignal is measured as photovoltage ($R_\mathrm{L} \gg R_\mathrm{sample}$) or photocurrent ($R_\mathrm{L} \ll R_\mathrm{sample}$).

For better comparability of the obtained photovoltage $U_{x,y}$ is normalized to the recorded reference signal U_{ref} according to:

$$U_{x,y}/P = \frac{U_{x,y} \cdot P_\mathrm{calib}}{U_\mathrm{ref}}. \tag{29}$$

Here P_calib is a calibration factor, obtained by measuring the averaged laser output power P and normalizing it to the mean value of the reference signal U_ref.

3.2.3 Measurements of Radiation Transmission

In addition, measurements of the radiation transmission through the sample are performed. This is a standard method to identify the effect of cyclotron resonance. In the used setup, the THz radiation and the external magnetic field are applied normal to the surface of the unbiased sample, as shown in Fig. 17. The part of the radiation that is not absorbed by the sample passes through it and is focused onto a detector. This detector is either a Golay cell (high sensitivity, slow) or a pyroelectric detector (fast). The signal is then further processed with standard Lock-in technique. To improve the noise level and overcome possible hysteresis effects of the detector, these measurements are done twice and then averaged.

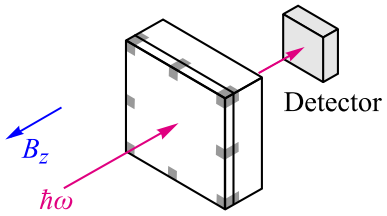

Figure 17: Setup of the transmission measurement. The magnetic field B_z and the THz radiation ($\hbar\omega$) are applied normal to the surface of the sample. The part of the radiation that is not absorbed passes through the sample and is detected.

3.3 Investigated Samples

In the framework of this thesis, 2D and 3D topological insulators based on HgTe QWs and films are investigated. In this section, the designs and properties of the used systems are briefly outlined. All of the samples presented here have been grown in the A.V. Rzhanov Institute in Novosibirsk, Russia by Dr Sergey A. Dvorestky and Dr Nikolay N. Mikhailov.

3.3.1 Mercury Telluride Films

For the investigation of photocurrents in 3D TIs, strained high-mobility 80 nm HgTe films are used. The full cross-section of the samples is depicted in Fig. 18(a). The different layers are grown by molecular beam epitaxy (MBE) on a (013)-orientated GaAs substrate, which is covered by a thin ZnTe layer and a fully relaxed 4 µm thick CdTe layer [68]. On top of this, the investigated layer system is grown, which consists of the 80 nm HgTe film sandwiched between two $Cd_{0.65}Hg_{0.35}$ layers acting as capping (top) and buffer (bottom) layers. These CdHgTe/HgTe/CdHgTe layers adopt the lattice constant a of the underlying CdTe layer. The arising lattice mismatch between HgTe ($a = 6.46\,\text{Å}$) and CdTe ($a = 6.48\,\text{Å}$) of about 0.3% results in a tensile strain in the HgTe film. This opens a topological gap in the otherwise gapless material [18, 38].

An evidence of the arising strain can be seen in the X-ray reciprocal space map depicted in Fig. 18(b), where the diffracted intensity is plotted on a colour-

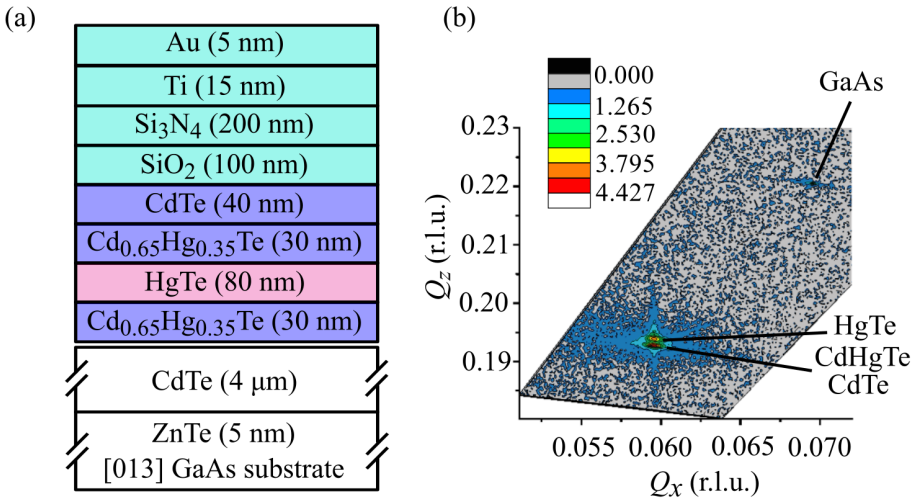

Figure 18: (a) Cross-section of the 80 nm HgTe film. The investigated HgTe structure is sandwiched between two $Cd_{0.65}Hg_{0.35}Te$ layers (in pink and blue respectively). These are grown on a (013)-oriented GaAs substrate including buffer layers (depicted in white). Some samples have an additional gold (Au)/titan (Ti) top gate, which is isolated from the QW by SiO_2 and SiN layers (shown in green). (b) X-ray diffraction space map near the asymmetric (113)-reflection, revealing the strain of the used films. Here, the diffracted intensity is plotted on a colour-coded logarithmic scale in dependence on the reciprocal lattice unit (r.l.u.).

coded logarithmic scale. The CdTe film is fully relaxed with respect to the GaAs substrate, as their maxima points lie on a straight line with the origin of the reciprocal space. In contrast, the peaks of HgTe and the CdHgTe layers are on a straight line along the z-axis perpendicular to the sample surface with the maximum of CdTe. This indicates that these layers are fully strained with respect to CdTe.

The used sandwich design reduces the influence of dislocations due to the lattice mismatch and enables high electron mobilities [69]. In the investigated samples, mobilities up to $\mu_e \approx 4 \cdot 10^4\,\mathrm{cm}^2/\mathrm{V}$ at $T = 40\,\mathrm{K}$ are obtained. The low residual bulk impurity lies at about $n \approx 10^6\,\mathrm{cm}^3$, which is estimated from ungated samples.

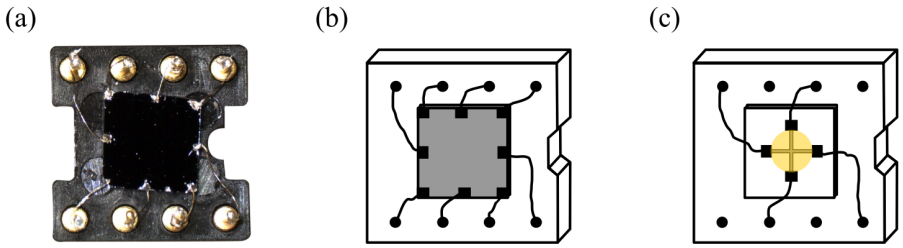

Figure 19: (a) Photo and (b) sketch of a large-area square-shaped 80 nm HgTe sample. This kind of sample is used for the simultaneous measurement of transmission and photosignals. (c) Sketch of a cross-shaped gated sample used for photocurrent measurements as a function of the Fermi level position.

For the following study, several samples are prepared from the same waver. Large-area square-shaped samples (Van-der-Pauw geometry) depicted in Fig. 19(a) and (b) are used for the simultaneous measurement of the transmission and the photosignals. For the latter, eight ohmic contacts are soldered to the sample with indium - four in the corners and four at the edges. These contacts are connected via gold wires to the pins of an eight-pin chip carrier. The edges of the samples are about 5 mm long and are oriented along $x \parallel [100]$ and $y \parallel [03\bar{1}]$.

In order to allow the study of magneto-transport and photocurrents in dependence on the position of the Fermi level, gated structures are fabricated by photo-lithography technique and wet etching. To reduce the likelihood of insulator leakages, small-area cross-shaped structures are produced, as shown in Fig. 19(c). These structures are 50 µm wide and 1500 µm long and have four Ohmic contacts, which are indium-soldered and connected via gold wires to the chip carrier. The yellow area in Fig. 19(c) schematically depicts the gate area. These semi-transparent gates with a diameter of 1500 µm consist of 15 nm Ti and 5 nm Au and are deposited on 100 nm $Si0_2$ and 200 nm of Si_3N_4. The latter one acts as a dielectric layer, as shown in Fig. 18(a).

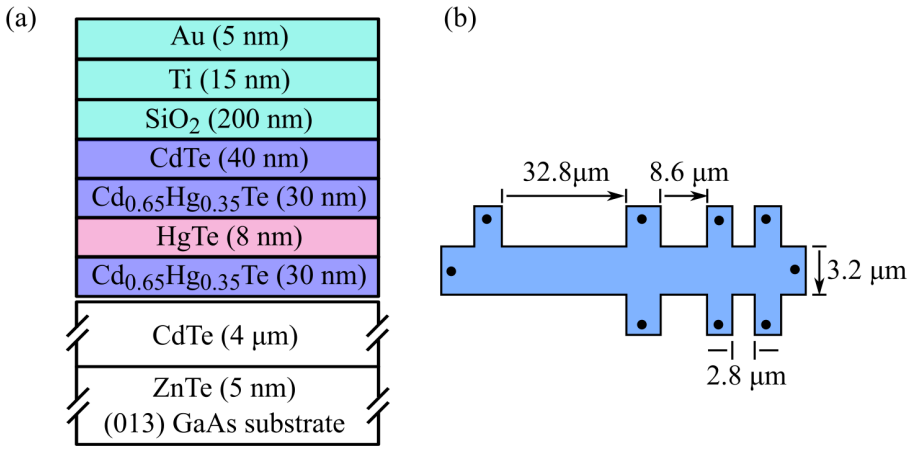

Figure 20: (a) Cross-section of the investigated 8 nm HgTe quantum well structure. On top of the [013]-oriented GaAs substrate, with buffer layers (depicted in white), the $Cd_{0.65}Hg_{0.35}$/HgTe/$Cd_{0.65}Hg_{0.35}$ quantum well structure is MBE-grown (in pink and blue respectively). Green layers depict the gold (Au)/titan (Ti) top gate. (b) Layout of the Hall-bar structure with different contact spacing.

3.3.2 Mercury Telluride Quantum Wells

In the second part of the thesis, 8 nm HgTe single quantum wells are investigated. In such systems, the band structure and ordering strongly depend on the thickness of the studied QWs, as seen in Sec. 2.1.4. For the 8 nm HgTe layer used here, the band ordering is inverted and topologically protected edge states can arise. Moreover, for the used thickness, the energy gap is in dimensions of $E_{\mathrm{gap}} \approx 25\,\mathrm{meV}$ [17, 70] and is consequently bigger than the photon energy used for the investigation.

A cross-section of the MBE-grown [12] samples can be found in Fig. 20(a). On top of the (013)-GaAs wafer, a thin film of ZnTe (5 nm) and 4 µm CdTe is placed. These layers assemble the substrate of the investigated $Cd_{0.65}Hg_{0.35}$/HgTe/$Cd_{0.65}Hg_{0.35}$ QWs. All samples are prepared with a semi-transparent top gate, which allows the control of the Fermi level. This gate is grown by

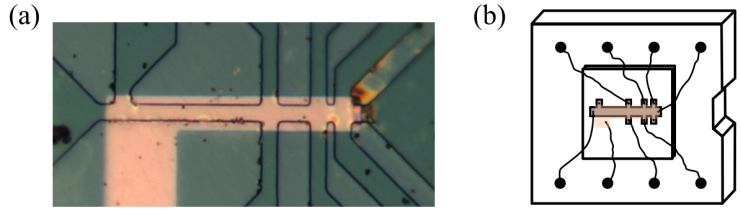

Figure 21: (a) Image of the investigated Hall-bar structure, where the peach-coloured area represents the top-gate. (b) Sketch of the Hall-bar mounted on the chip carrier. One of the pins is connected to the top gate (peach-coloured) and the other seven to contacts of the Hall-bar.

chemical vapour deposition and is composed of 15 nm Ti and 5 nm Au. It is isolated from the QW by a layer of 200 nm SiO_2, acting as insulators.

To enable the studies of magneto-transport and photosignals in the quantum spin Hall regime, small Hall-bars are prepared by photo-lithography technique and wet etching. For bigger samples, the probability of inelastic electron scattering increases, even in the helical edge states, which makes the investigation more difficult. In this work, seven samples from two wafers are studied. A sketch of the typical design, including dimensions can be found in Fig. 20(b). The whole structure is about 57 µm long and has a width of 3.2 µm. The spacing between the contacts differs, ranging from $l = 2.8$ µm to $l = 32.8$ µm. A microscopical image of a real structure is plotted in Fig. 21(a), where the peach-coloured area is the top gate.

The sample is attached to an eight-pin chip carrier, as shown in Fig. 21(b). One of these pins is connected via a gold wire to the top gate (peach-colour), allowing the application of a voltage to the gate layer. The other seven pins are attached to contacts of the Hall-bar structure via gold wires and indium soldering.

4 Cyclotron Resonance of 2D Surface States in HgTe-Based Films

In this chapter, cyclotron-resonance-assisted photocurrents in strained high-mobility 80 nm HgTe films are presented. In such a system, a band gap opens in the otherwise gapless HgTe bulk material and a three-dimensional topological insulator with conducting surface states can be realized, as seen in Sects. 2.1.3 and 2.1.4. Here, the existence of these states is proved and they are investigated with the help of cyclotron-resonance-enhanced photocurrents. This study is supported by complementary measurements of transport and transmission. All results presented in this chapter are published in Ref. [24].

4.1 Sample Characterization

Before the performance of actual photocurrent measurements, all the samples studied in this chapter are characterized by magneto-transport measurements. This characterization is done in close cooperation with Dr Dmitriy A. Kozlov[4] after Ref. [69]. Details concerning the experimental geometry and signal detection can be found in Sec. 3.2.1.

In Fig. 22, the longitudinal resistance $\rho_{xx}(B)$ and the Hall resistance $\rho_{xy}(B)$, measured as a function of the magnetic field B_z applied normally to the film plane, are exemplarily depicted for temperatures of $T = 4.2\,\mathrm{K}$ in blue and for $T = 40\,\mathrm{K}$ in red. For both temperatures, the determined longitudinal resistance ρ_{xx} has positive values and is even in the magnetic field. The Hall resistance ρ_{xy} shows a non-linear N-type shape for small magnetic fields. This – together with the large positive longitudinal resistance – is characteristic for a system with coexisting electrons and holes [71]. The same behaviour is found in measurements performed at various fixed temperatures in a range of $T = 4.2 - 120\,\mathrm{K}$ (not shown).

From these traces, the densities and the mobilities for both carrier types can be obtained by using the classical two-component Drude model [69]. The resulting

[4] A. V. Rzhanov Institute, Novosibirsk, Russia

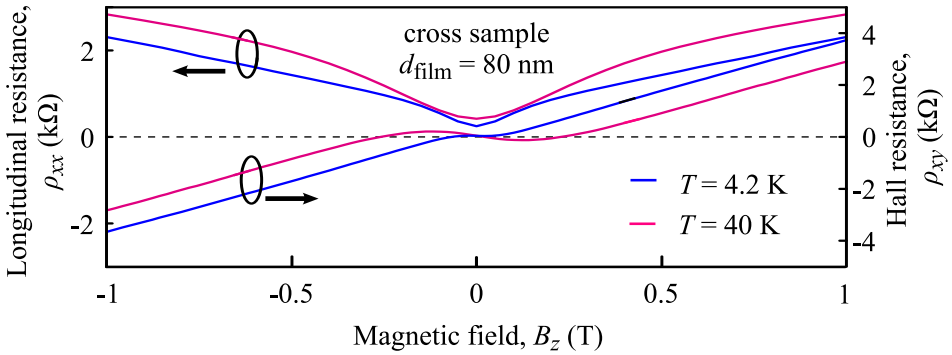

Figure 22: Magneto-transport data obtained in an ungated cross-shaped 80 nm film for $T = 4.2\,\text{K}$ and $T = 40\,\text{K}$ in blue and red respectively. The longitudinal resistance ρ_{xx}, which scales on the left side, shows a large positive resistance. The Hall resistance ρ_{xy} (right scale) exhibits a non-linear N-type shape around $B = 0\,\text{T}$, which is typical for an electron-hole system.

carrier densities for holes, p (red triangle), and electrons, n (blue triangle), are depicted in dependence on the temperature in Fig. 23(a). For both types of carriers, an abrupt increase in the density can be found at temperatures higher than $T \gtrsim 25$ K. Below this temperature, the densities almost saturate at a value of $n = 0.4 \cdot 10^{11}\,\text{cm}^{-2}$ for electrons and $p = 4.5 \cdot 10^{11}\,\text{cm}^{-2}$ for holes (see inset Fig. 23(a)). The existence of holes, even at low temperatures, is an indication that the Fermi level is situated in the valence band and therefore, the existing electrons can be attributed to the surface states of the HgTe film. In Fig. 23(b), the mobilities for electrons (μ_e) and holes (μ_p) as a function of temperature are depicted. They decrease with increasing temperature and saturate for $T > 60\,\text{K}$ at a value of approximately $\mu_\text{e} = 5 \cdot 10^4\,\text{cm}^2/\text{Vs}$ for electrons and $\mu_\text{p} = 0.8 \cdot 10^4\,\text{cm}^2/\text{Vs}$ for holes.

In addition, magneto-transport measurements are carried out on gated samples. Typical resistance curves (ρ_{xx}) obtained at $B_z = 0\,\text{T}$ as a function of the applied gate voltage are shown in Fig. 24(a) for $T = 4.2\,\text{K}$ (blue) and for $T = 40\,\text{K}$ (red). The low-temperature resistance reaches a maximum near $U_\text{g} \approx -0.8\,\text{V}$. For the same applied gate voltage value, the Hall resistance ρ_{xy} changes its sign. This is exemplarily depicted in Fig. 24(b) as a function of the magnetic field for two different gate voltage values. For $U_\text{g} = -4\,\text{V}$, the

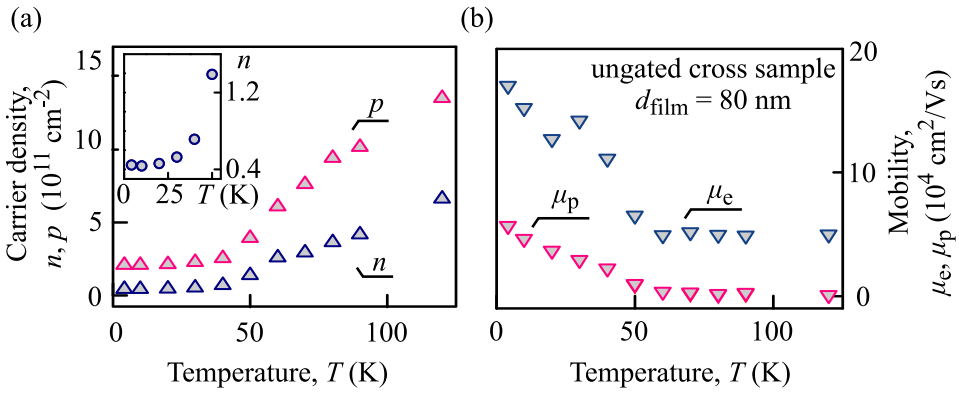

Figure 23: Electron and hole (a) densities (n (blue triangle) and p (red triangle)) as well as (b) mobilities (μ_e (blue triangle) and μ_p (red triangle)) as a function of temperature, extracted with the Drude model from magneto-transport measurements on a 80 nm HgTe ungated cross-shaped film. The carrier densities show an activation behaviour around $T = 25\,\mathrm{K}$ (see inset in (a)). The existence of holes even at low temperature reveals that the Fermi level lies in the valence band. Therefore, the electrons can be associated with the surface states.

Hall resistance ρ_{xy} has the same behaviour as the ungated sample, whereas for values larger than $U_g = 0.8\,\mathrm{V}$, the slope changes its sign. This proves that the Fermi level can be tuned with the top gate from the valence band crossing the surface states into the conduction band. In a detailed study of the transport properties, the borders of the bulk bands are determined for this material system in Ref. [69]. In Fig. 24(a), these points are marked with E_v for the valence band and E_c for the conduction band edge.

In the same work, the carrier densities are determined as a function of the applied gate voltage of the system investigated herein. As these results are important for the analysis of the photocurrent study, the main conclusions are depicted in Fig. 24(c) and are briefly outlined here. The densities of the total number of electrons and the bulk holes (n_{total} and p_{bulk}) are plotted in black squares and circles in dependence on the gate voltage respectively. Considering the total number of electrons, a strong dependence on U_g is observed. For negative applied gate voltages, n_{total} only slightly rises with increasing U_g, whereas for positive gate voltages, it increases rapidly up to a value of $n_{total} =$

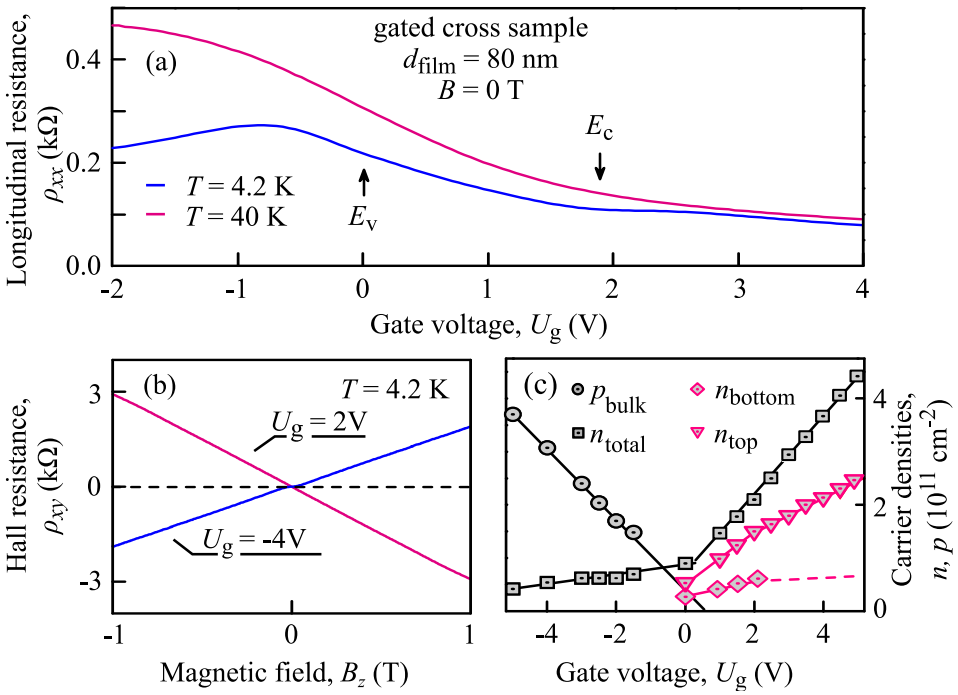

Figure 24: (a) Gate-voltage-dependence of the longitudinal resistance ρ_{xx} for $T = 4.2\,\mathrm{K}$ and $T = 40\,\mathrm{K}$ for the cross-shaped sample. The edge of the valence band is marked with E_v and the edge of the conduction band with E_c. For negative U_g, the system is a hole metal, which turns into a topological insulator and – finally for large positive gate voltages – into an electron metal. (b) Example of the magnetic-field-dependence of the Hall resistance ρ_{xy} measured at a cross-shaped sample at $T = 4.2\,\mathrm{K}$ for fixed gate voltages of $U_\mathrm{g} = -4\,\mathrm{V}$ (blue) and $U_\mathrm{g} = 2\,\mathrm{V}$ (red) representing a hole and an electron metal system respectively. (c) Gate-voltage-dependence of the carrier densities of electrons (n_total), holes (p_bulk) and the surface states (n_top and n_bottom) determined from a Hall-bar.

$4.4 \cdot 10^{11}\,\mathrm{cm}^{-2}$ obtained for $U_\mathrm{g} = 5\,\mathrm{V}$. In contrast, the hole density decreases for decreasing negative gate voltage and completely vanishes for $U_\mathrm{g} > 0\,\mathrm{V}$. The carrier densities of the top (n_top, red triangles) and the bottom surface states (n_bottom, red squares) are depicted in Fig. 24(c) respectively. From these results – in combination with a calculation of the k-linear dispersion of Dirac electrons [18] – an energy gap of $E_\mathrm{gap} \approx 15\,\mathrm{meV}$ is estimated [69]. Therefore, the thermal occupation for low temperatures used in experiments is small,

when the Fermi level lies in the valence band and only the surface electrons can contribute to the transport.

Note that although the overall characteristics of the transport data are reproducible, the position of the gap can shift on the gate voltage scale. This can be attributed to built-in electric fields due to the fabrication of the gate or due to different cool-down circles. To enable the comparability of all data, transport experiments are done under the same conditions as the photosignal measurements and the charge neutrality point (CNP) is shifted to the same gate voltage value for all investigated samples.

4.2 Terahertz Radiation-Induced Photogalvanic Effects

In this section, the experimental data of the THz radiation-induced photogalvanic effect in unbiased HgTe films are presented. The radiation and the magnetic field B_z are applied under cyclotron resonance condition, meaning that both are aligned normal to the surface of the sample. The experimental setups of the photosignal and the transmission measurements are illustrated in Secs. 3.2.2 and 3.2.3 respectively.

4.2.1 Photocurrents at Zero Magnetic Field

By exciting 80 nm HgTe films with linear polarized THz radiation under normal incidence without a magnetic field, a measurable electric current is observed. The dependence of the normalized photocurrent $U_{x,y}/P$ in x- (red dots) and y-directions (black dots) on the linear polarization angle α is depicted in Fig. 25. Note that for a better comparability, the data for the x-direction are multiplied

direction	A	B	C
x	0.19	0.051	0.017
y	0.06	+0.016	-0.012

Table 2: Fitting parameter after Eq. (30) for the photocurrent measurements as a function of the angle α, without an external magnetic field for the 80 nm HgTe film. Traces are depicted in Fig. 25 as solid lines.

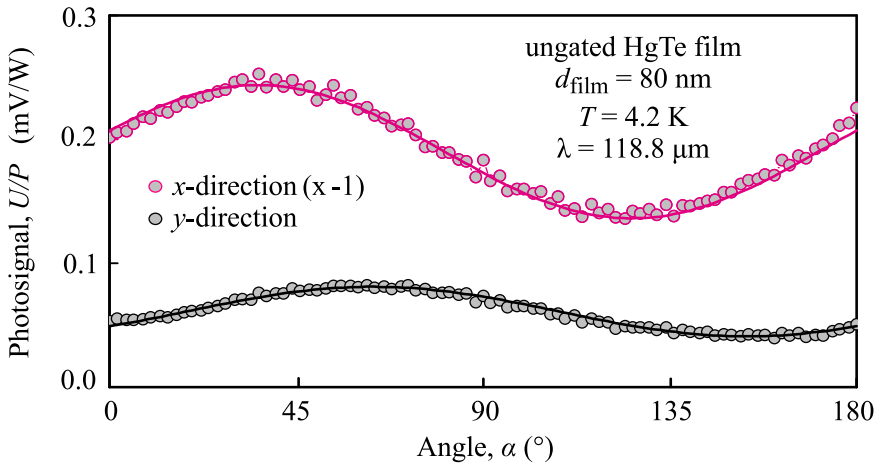

Figure 25: Normalized photosignal $U_{x,y}/P$ in x- (red dots) and y-directions (black dots) as a function of the angle α without an external magnetic field for the 80 nm HgTe film. Both curves are fitted with Eq. (30) (solid lines). The curve for the x-direction is multiplied by -1 for a better compatibility.

by -1. The mean values of the normalized photosignal in the two orthogonal directions are in the same order of magnitude, with $U_x/P = -0.19\,\mathrm{mV/W}$ and $U_y/P = 0.06\,\mathrm{mV/W}$ for x- and y-directions respectively. By changing the angle α, which represents a changing of the linear polarization plane in regard to the x-direction, a modulated photosignal is detected, which can be fitted as follows:

$$U_{x,y}(\alpha)/P = A + B\sin(2\alpha) + C\cos(2\alpha). \tag{30}$$

The corresponding fitting curves are shown in Fig. 25 as solid lines and the parameters are summarized in Tab. 2.

4.2.2 Cyclotron-Resonance-Assisted Photocurrents

By applying a magnetic field, the behaviour of the photocurrent changes and a strong resonant dependence is observed. First, magnetic-field-dependencies of the normalized photovoltage U_x/P in an ungated square-shaped sample are presented. The results found at a temperature of $T = 40\,\mathrm{K}$ for radiation with a wavelength of $\lambda = 118.8\,\mu\mathrm{m}$ are depicted in Fig. 26(a) for left- (σ^-, blue dots) and right-handed (σ^+, red dots) circularly polarized radiations.

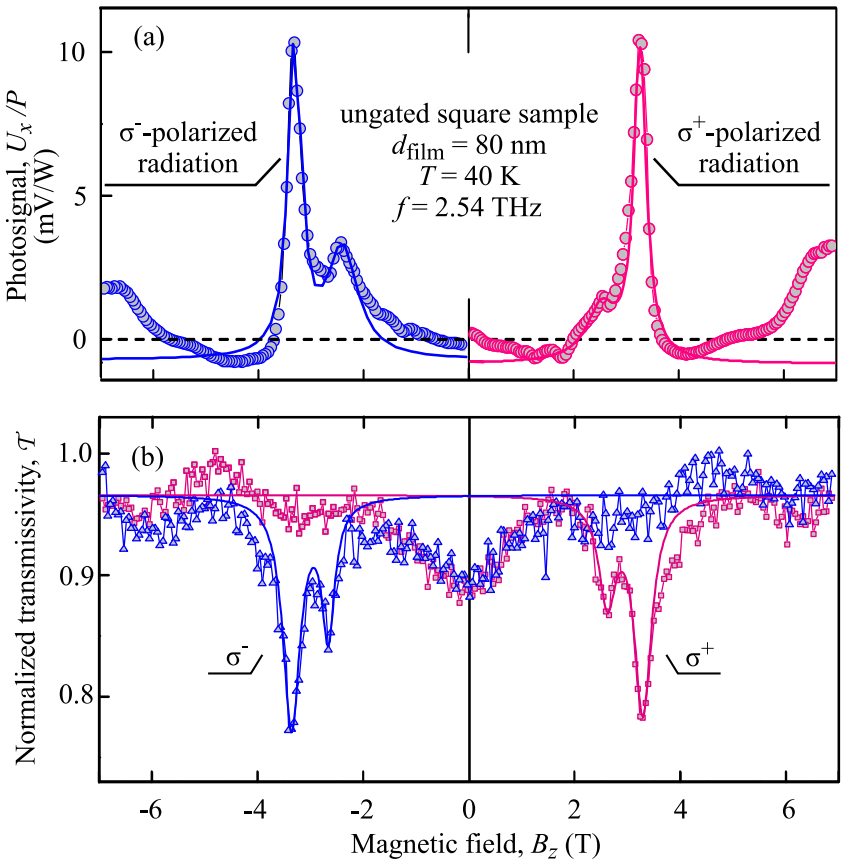

Figure 26: (a) Normalized photosignal U_x/P and (b) transmissivity $\mathcal{T}$ as a function of the magnetic field B_z measured in an ungated square-shaped HgTe film at $T = 40\,\mathrm{K}$. For right-handed (σ^+) circularly polarized radiation, two resonant peaks appear at positive magnetic field values of $B_{\mathrm{CR1}} = 2.55\,\mathrm{T}$ and $B_{\mathrm{CR2}} = 3.25\,\mathrm{T}$. (b) By switching the helicity to left-handed (σ^-), the resonances shift to negative magnetic fields.

By exciting the film with σ^+-polarized radiation and sweeping the magnetic field from $B_z = -7$ to $7\,\mathrm{T}$ two resonant peaks are observed at the positive magnetic field side. The centre values of the resonances are $B_{\mathrm{CR1}} = 2.55\,\mathrm{T}$ and $B_{\mathrm{CR2}} = 3.25\,\mathrm{T}$ with maximal amplitudes of $U_x/P = 1.53\,\mathrm{mV/W}$ and $U_x/P = 10.40\,\mathrm{mV/W}$ respectively. By switching the radiation helicity from σ^+ to σ^-, the resonances shift to the negative magnetic field side, with $B_{\mathrm{CR1}} = -2.4\,\mathrm{T}$ ($U_x/P = 3.33\,\mathrm{mV/W}$) and $B_{\mathrm{CR2}} = -3.3\,\mathrm{T}$ ($U_x/P = 10.34\,\mathrm{mV/W}$).

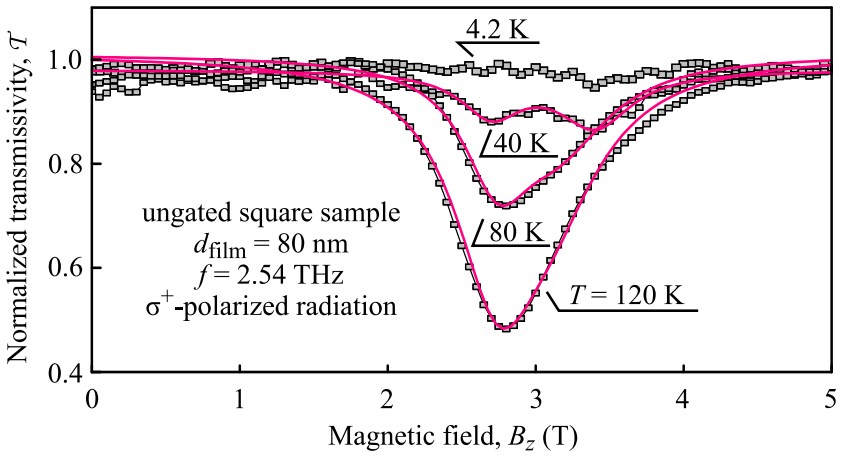

Figure 27: Averaged and normalized transmissivity $\mathcal{T}$ as a function of the magnetic field B_z for an ungated square-shaped 80 nm HgTe film measured at different fixed temperatures in the range of $T = 4.2 - 120$ K. Red lines represent Lorentzian fits after Eq. (31).

All resonances exhibit a Lorentzian-like distribution and are fitted by:

$$\mathcal{F}(B) = O \pm \frac{2A}{\pi} \frac{W}{W^2 + 4(B - B_{\mathrm{CR}})^2}, \tag{31}$$

where O is an offset, A the amplitude, W the width, and B_{CR} the centre value of the resonance. Such fits can be seen exemplarily as solid lines in Fig. 26. The slight asymmetry of the curve and the resulting deviation from the perfect Lorentzian shape can be explained by taking into account the multiple reflections in the substrate and a super-radiant decay [72, 73]. Note that the signals in y-direction exhibit a similar behaviour with resonances at the same magnetic field positions (not shown).

The same strong helicity-dependence can be found in the transmissivity measurements, as shown in Fig. 26(b) for a temperature of $T = 40$ K. Here, the data are normalized to the laser power and the maximal signal is defined as 100 %. To further improve the clarity of the data, two measurements are averaged. In the transmissivity $\mathcal{T}$ measurements, two strong resonances can be found for right-handed circularly polarized radiation (depicted in red rectangle). The first resonance appears at $B_{\mathrm{CR1}} = 2.67$ T and the second at $B_{\mathrm{CR2}} = 3.35$ T, with a minimal value of $\mathcal{T} = 0.85$ and $\mathcal{T} = 0.76$ respectively. For left-handed

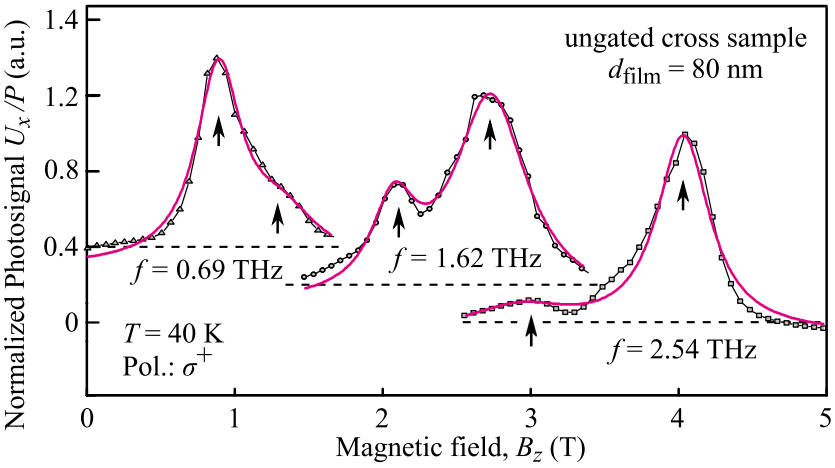

Figure 28: Normalized photovoltage U_x/P measured for three different frequencies in an ungated cross-shaped sample. The data are shifted in the vertical direction by 0.2 for $f = 1.62\,\text{THz}$ and by 0.4 for $f = 0.69\,\text{THz}$ and the maximum of each trace is normalized to one. Full lines show Lorentzian fits pursuant to Eq. (31).

circularly polarized radiation, the dips appear at negative magnetic field values of $B_{\text{CR1}} = -2.6\,\text{T}$ ($\mathcal{T} = 0.82$) and $B_{\text{CR2}} - 3.35\,\text{T}$ ($\mathcal{T} = 0.74$). Again, the solid lines represent the Lorentzian fits after Eq. (31).

Similar dips in transmission $\mathcal{T}$ are detected in a temperature range of $T = 10\,\text{K}$ to $T = 120\,\text{K}$, as exemplary depicted in Fig. 27. For temperatures lower than $T = 10\,\text{K}$, no clear resonances can be observed, as the amplitudes of the dips are smaller than the noise level of the used setup. As already seen in Fig. 26(b), two clear dips arise at $T = 40\,\text{K}$. With rising temperature, the amplitude of the dips increases and at $T > 80\,\text{K}$, they start merging together. For temperatures as high as $T = 120\,\text{K}$, only one resonance can be found, with a centre value of $B_{\text{CR}} = 2.8\,\text{T}$. These curves are again fitted with a Lorentzian function (Eq. (31)), see solid lines in Fig. 27.

Until now only measurements in large-area square-shaped samples (Van-der-Pauw geometry) are shown. Although these samples are necessary for transmission measurements, they are too big for the fabrication of a gate. Therefore, the following study of photocurrents is done on smaller cross-shaped samples. In Fig. 28, the resonances of the photosignal U_x/P are depicted in dependence

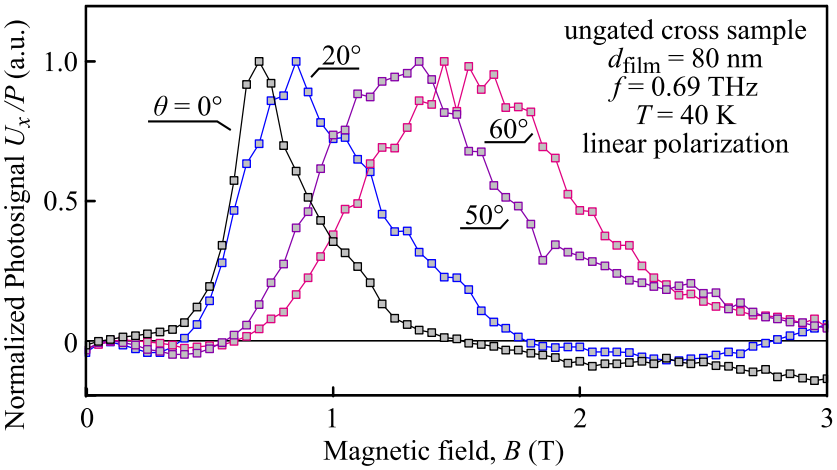

Figure 29: Normalized photovoltage in dependence of a magnetic field tilted by an angle θ. A strong dependence of the cyclotron resonance position on the magnetic field angle is observed.

on the magnetic field for three different radiation frequencies. For better clarity, the traces are shifted in y-direction by values of 0.2 and 0.4 for frequencies of $f = 1.62\,\mathrm{THz}$ and $f = 0.69\,\mathrm{THz}$ respectively. In addition, the maximal signal of each radiation frequency is defined as $U_x/P = 1.0$.

The resonances for a radiation frequency of $f = 2.54\,\mathrm{THz}$ arise at almost the same magnetic field positions as in the large square-shaped samples, with values of $B_{\mathrm{CR1}} = 2.4\,\mathrm{T}$ and $B_{\mathrm{CR2}} = 3.25\,\mathrm{T}$. By reducing the radiation frequency to $f = 1.62\,\mathrm{THz}$, the resonances move to smaller magnetic field values, $B_{\mathrm{CR1}} = 1.65\,\mathrm{T}$ and $B_{\mathrm{CR2}} = 2.15\,\mathrm{T}$. In case of a further reduction in the frequency to $f = 0.69\,\mathrm{THz}$, the resonances appear at even smaller values of $B_{\mathrm{CR1}} = 0.7\,\mathrm{T}$ and $B_{\mathrm{CR2}} = 1.1\,\mathrm{T}$. Moreover, the relative strength of the first and the second resonance changes considerably. The first resonance has a smaller amplitude than the second one for frequencies of $f = 2.54\,\mathrm{THz}$ and $f = 1.62\,\mathrm{THz}$, whereas this behaviour is reversed for $f = 0.69\,\mathrm{THz}$.

For a better understanding of the photocurrent origin, measurements with a magnetic field tilted by an angle θ and a fixed radiation frequency of $f = 0.69\,\mathrm{THz}$ are performed. Focusing on the main resonance, a clear shift to higher magnetic field values for an increase in the tilting angle θ is observed, as shown in Fig. 29. The resonance shifts from $B_{\mathrm{CR1}} = 0.7\,\mathrm{T}$ to $B_{\mathrm{CR1}} = 1.45\,\mathrm{T}$ when

angle θ	CR position B_{CR} (T)	$B_{\mathrm{CR}}^{\perp}$ (T)
0°	0.7	0.7
20°	0.8	0.75
40°	0.85	0.65
50°	1.35	0.85
60°	1.45	0.72

Table 3: Resonance position B_{CR} and the effective position $B_{\mathrm{CR}}^{\perp} = B_{\mathrm{CR}} \cdot \cos(\theta)$ for the normalized photosignal measured in an ungated cross-shaped sample at a frequency of $f = 0.69\,\mathrm{THz}$. The according curves are depicted in Fig. 29.

changing $\theta = 0°$ to $\theta = 60°$. The values of all shown traces are summarized in Tab. 3. Again, these traces are normalized, so that the maximum of the photosignal equals $U_x/P = 1.0$. Moreover, for an in-plane magnetic field B_x ($\theta = 90°$) the photosignal completely vanishes (not shown).

4.2.3 Gate-Voltage-Dependency

To investigate the influence of the Fermi energy position on the resonances, samples with top gate structure are used. In Fig. 30(a) and (b), the observed photocurrents are shown as a function of the applied gate voltage for $T = 40\,\mathrm{K}$ and $T = 20\,\mathrm{K}$. For better clarity, the traces are shifted in the y-direction and fitted with Eq. (31) (solid lines). Starting with the higher temperature, a strong dependence of the photosignal on the applied gate voltage is observed. For a negative gate voltage – depicted here for $U_{\mathrm{g}} = -0.5\,\mathrm{V}$ – no clear resonance is found. By increasing the gate voltage, first a resonance at $B_{\mathrm{CR2}} = 3.35\,\mathrm{T}$ ($U_{\mathrm{g}} = 0\,\mathrm{V}$) and then a second one at $B_{\mathrm{CR1}} = 2.6\,\mathrm{T}$ ($U_{\mathrm{g}} = 0.5\,\mathrm{V}$) appear. Note that for such small gate voltages, the resonance position is similar to those obtained for the ungated samples.

By increasing the applied gate voltage further to values above $U_{\mathrm{g}} \approx 1.5\,\mathrm{V}$, a third resonance appears at $B_{\mathrm{CR3}} = 2.45\,\mathrm{T}$. Moreover, all resonances increase in amplitude by increasing the gate voltage. Focusing on the position of the resonances, it can be found that only the resonance at a magnetic field of

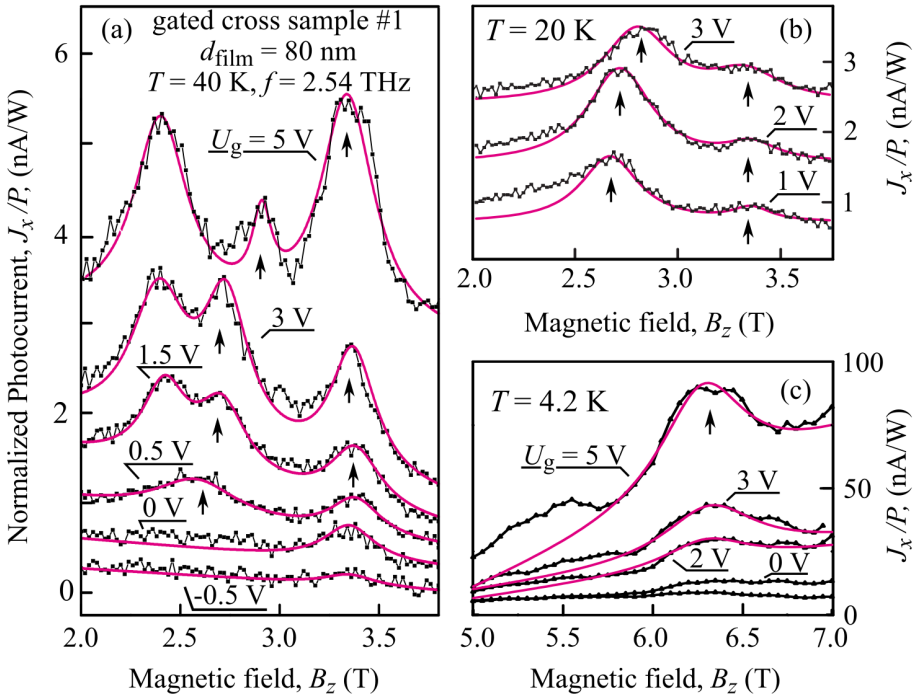

Figure 30: Magnetic-field-dependency of the gated cross-shaped sample #1 for different applied gate voltages, measured at (a) $T = 40\,\mathrm{K}$ and (b) $T = 20\,\mathrm{K}$. Solid lines show Lorentzian fit pursuant to Eq. (31). Note that the traces are shifted in the y-direction for clarity. (c) Magnetic-field-dependencies of the resonances for low temperature and high magnetic fields.

$B_{\mathrm{CR1}} \approx 2.6\,\mathrm{T}$ exhibit a clear dependence on the applied gate voltage. This resonance shifts from $B_{\mathrm{CR1}} = 2.56\,\mathrm{T}$ to $B_{\mathrm{CR1}} = 2.91\,\mathrm{T}$ due to an increase of the gate voltage from $U_{\mathrm{g}} = 0.5\,\mathrm{V}$ to $U_{\mathrm{g}} = 5.0\,\mathrm{V}$. The other two resonance positions show no observable dependence on the applied gate voltage. For $T = 20\,\mathrm{K}$ a similar behaviour can be observed, although the resonance at $B_{\mathrm{CR3}} = 2.4\,\mathrm{T}$ is absent. Here, B_{CR1} shifts from 2.7 T to 2.85 T upon changing the gate voltage from $U_{\mathrm{g}} = 1\,\mathrm{V}$ to $U_{\mathrm{g}} = 3\,\mathrm{V}$. Note that the curves for gate voltages of $U_{\mathrm{g}} = 2\,\mathrm{V}$ and $U_{\mathrm{g}} = 3\,\mathrm{V}$ in Fig. 30(b) are multiplied by a factor of four and are shifted in the y-direction. Hence, the amplitudes J_x/P of the resonances decrease with an increase in the applied gate voltage.

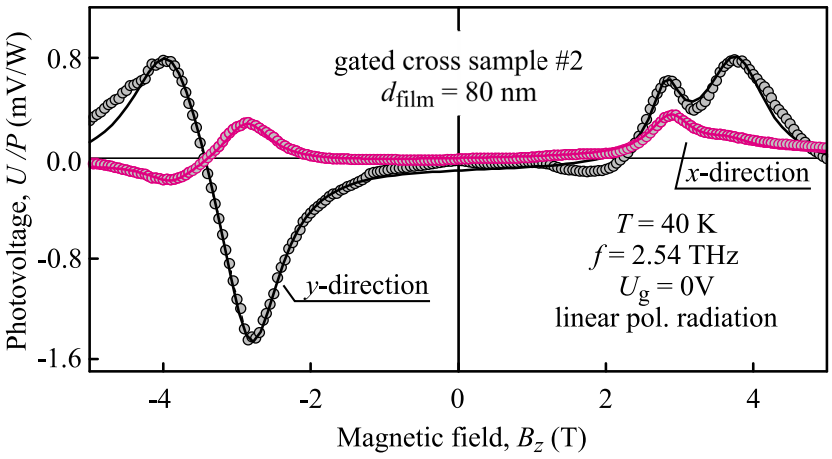

Figure 31: Magnetic-field-dependence of the normalized photovoltage U/P of the gated cross-shaped sample #2 measured in two orthogonal directions for linearly polarized radiation. The two resonances behave independently of each other and can exhibit odd or even dependence on the magnetic field B_z.

In Fig. 30(c), the measurements of the normalized photosignal J_x/P at helium temperature are depicted for different applied gate voltages. For gate voltages larger than $U_g = 2\,\mathrm{V}$, a fourth resonance appears at a higher magnetic field value ($B_{CR4} = 6.3\,\mathrm{T}$). The position of this resonance is almost independent of the applied gate voltage. For $B_z < 5\,\mathrm{T}$ and $T = 4.2\,\mathrm{K}$ the CR related resonances are superimposed by Shubnikov-de Haas oscillations (not shown) and therefore will not be discussed here. The influence of these oscillations on the photocurrent is well-known for HgTe samples and is studied in Ref. [74] for HgTe QWs with different widths, which are characterized by a Dirac-like, inverted or normal parabolic band structure.

Until now, only photocurrent measurements for one magnetic field polarity are shown. In Fig. 31, the photocurrent behaviour measured in two orthogonal directions is depicted for a reversal in the magnetic field direction. Surprisingly, the two resonances behave different on the magnetic field polarity. For example, the resonance at the smaller magnetic field (B_{CR1}) in the y-direction is odd in the magnetic field, whereas the peak at B_{CR2} is even. Moreover, for

the x-direction, the situation is reversed and the first resonance behaves evenly while the resonance at higher magnetic field is odd.

4.3 Discussion

Teraherz radiation-induced photocurrents observed in strained 80 nm HgTe films and shown in Sec. 4.2 are discussed in this section. These photocurrents exhibit strong resonances, which can be understood in the framework of cyclotron resonance of electrons in the topologically protected bottom and surface states of the films. From the obtained data, the cyclotron masses of the two states are extracted and their dependence on the position of the Fermi level is discussed in regard to the band structure. Moreover, it is demonstrated that the photocurrent stems from magnetic-field-induced asymmetric scattering of surface state carriers in momentum space. All theoretical calculations are performed simultaneously to the measurements by Grigory V. Budkin[5] and Prof. Dr Sergey A. Tarasenko[5] and are published in Ref. [24]. Here, no detailed derivations of the equations are given and only the main features of the theoretical considerations are outlined.

4.3.1 Cyclotron Resonance of Surface States

By applying a magnetic field normal to the surface of a HgTe film, a THz radiation-induced photosignal with a strong resonant behaviour is observed, as shown in Fig. 26. These resonant positions $B_{\mathrm{CR}}^{\mathrm{PGE}}$ in the photosignal show a strong coincidence with the dips in the transmission measurements, arising at $B_{\mathrm{CR}}^{\mathrm{TM}}$ (see Tab. 4). This is a clear sign that the enhancement of the photocurrent occurs due to an increased absorption of radiation.

Moreover, the photocurrents exhibit a considerable dependence on the radiation helicity. For example, the photosignal peaks are more pronounced for the positive than for the negative magnetic field side for right-handed circularly polarized radiation. This is even more distinct in the transmission measurements, where only one dip at one magnetic field polarity appears for a fixed

[5]Ioffe Institute, St. Petersburg, Russia

helicity (not shown). This, together with the fact that the resonances can be nicely fitted with a Lorentzian curve, is a clear evidence that the absorption is caused by cyclotron resonance. All these features are also found in QWs with parabolic and linear energy dispersion (see Sec. 2.4) and can be explained by the theory given in Sec. 2.3. Moreover, the fact that right-handed circularly polarized radiation leads to an absorption at the positive magnetic field side is a strong indication that the resonant absorption is due to the cyclotron resonance of electrons.

From these traces, the cyclotron masses m_{CR} can be calculated with Eq. (14). The masses obtained from the photosignal resonances at $B_{\mathrm{CR1}} = \pm 2.5\,\mathrm{T}$ ($B_{\mathrm{CR2}} = \pm 3.3\,\mathrm{T}$) measured at $T = 40\,\mathrm{K}$ are $m_{\mathrm{CR1}} = 0.028\,m_0$ ($m_{\mathrm{CR2}} = 0.037\,m_0$). Almost the same values ($m_{\mathrm{CR1}} = 0.029\,m_0$ and $m_{\mathrm{CR2}} = 0.037\,m_0$) are obtained from the transmission measurements. All CR positions at this temperature are summarized in Tab. 4. The masses are calculated from the average CR positions for both radiation helicities and are in accordance with the values obtained in similar systems investigated in Refs. [75, 76].

These experimentally obtained masses agree well with the ones estimated from $\boldsymbol{k}\cdot\boldsymbol{p}$ calculations of the band structure of (013)-oriented 80 nm HgTe films. Details of the calculation of the energy dispersion of HgTe-based TIs in general can be found in Ref. [77] and those for the (013)-oriented films used here are given in the appendix of Ref. [24]. The results of these calculations are shown in Fig. 32(a), where the obtained bulk bands are depicted in black and the two surface states in red. The energy dispersion of the surface states clearly deviates from the expected linear one. This derivation arises due to the fact

	$B_{\mathrm{CR}}^{\mathrm{PGE}}$ (T)		$B_{\mathrm{CR}}^{\mathrm{TM}}$ (T)		$m_{\mathrm{CR}}^{\mathrm{PGE}}$ (m_0)	$m_{\mathrm{CR}}^{\mathrm{TM}}$ (m_0)
	σ^+	σ^-	σ^+	σ^-		
CR_1	2.55	−2.40	2.67	−2.6	0.028	0.029
CR_2	3.25	−3.3	3.35	−3.35	0.037	0.037

Table 4: Summary of the cyclotron resonance positions of an ungated 80 nm film for σ^+ and σ^- circularly polarized radiation, obtained from photosignals ($B_{\mathrm{CR}}^{\mathrm{PGE}}$) and transmission measurements ($B_{\mathrm{CR}}^{\mathrm{TM}}$). From these values, the cyclotron masses $m_{\mathrm{CR}}^{\mathrm{PGE}}$ and $m_{\mathrm{CR}}^{\mathrm{TM}}$ are calculated.

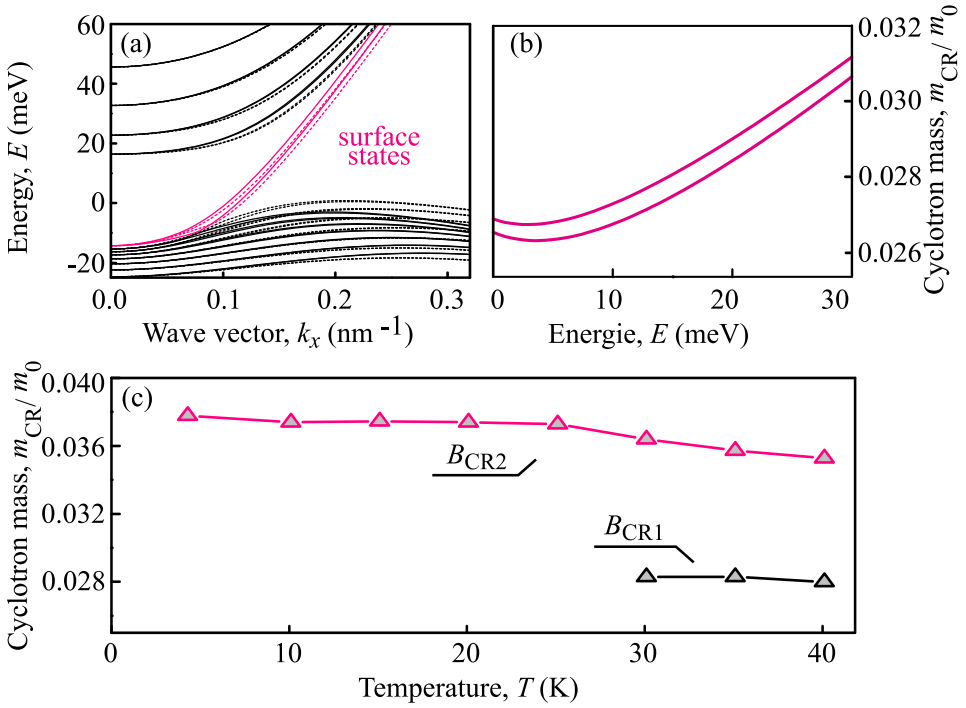

Figure 32: (a) Band structure of the (013)-grown 80 nm HgTe film calculated by $\boldsymbol{k} \cdot \boldsymbol{p}$ method. The black lines represent the bulk states and the red lines the surface states, calculated for two perpendicular in-plane crystallographic directions (in dashed and solid lines). Cyclotron masses of the two surface states (b) estimated from the calculation and (c) obtained from transmission measurements (for examples see Fig. 27) in an ungated 80 nm strained HgTe film in dependency on the temperature.

that the Dirac points of both interfaces lie deep in the valence band, which results in a hybridization with the Γ_8 heavy hole band [18].

The energy spectrum of the (013)-grown film is anisotropic at the interface plane. This is depicted in Fig. 32(a) for two orthogonal in-plane directions in solid and dashed lines. From this calculation, the masses of the top and bottom surface states can be estimated as a function of the energy, being in the range of $m_{\mathrm{CR1,CR2}} = 0.027 - 0.031\, m_0$, as shown in Fig. 32(b). Not only do these values match quite well the experimentally acquired ones ($m_{\mathrm{CR1}} = 0.028\, m_0$ and $m_{\mathrm{CR2}} = 0.037\, m_0$), but the cyclotron mass of bulk carriers estimated from the $\boldsymbol{k} \cdot \boldsymbol{p}$ calculations is also substantially larger, with a value of about $0.07\, m_0$.

Note that a detailed comparison of the computed and the experimental results would require a detailed knowledge of the electric field distribution of the real structures, which is out of the scope of this work.

Moreover, only a slight dependence of the surface masses on the energy is found, as shown in Fig. 32(b). This corresponds to the weak shift of the experimentally gained values upon changing the temperature, as shown in Fig. 32(c). These masses are estimated from transmission measurements, which are exemplarily depicted in Fig. 27. The deepening of the resonances and the consequent merging of the dips found therein can be explained by an increased absorption of radiation due to a higher carrier density for larger temperatures. Exactly such a behaviour is found in magneto-transport measurements for holes and for electrons, as shown in Fig. 23(a).

All the aforementioned features are good indications that the resonances arise due to electrons in the surface states. In addition, this assumption is further supported by the magneto-transport characterization of the sample, discussed in Sec. 4.1. It is shown that the Fermi level in the ungated samples lies in the valence band. These bulk states have a large effective mass and, therefore, a high density of states. It can be shown that the Fermi level in this sample, as well as in gated samples with negative gate voltages, is pinned to the top of the valence band. This can also be seen directly in Fig. 32(a), where no bulk electrons exist and hence the two clear resonances of electrons can only arise in the surface states.

For an experimental verification of the origin of these resonances, additional measurements on a smaller cross-shaped sample are performed. Although this geometry is too small to be used for transmission measurements, it allows the fabrication of a semi-transparent gate. First, photosignals U_x/P for different frequencies are investigated in this type of sample, as shown in Fig. 28. For a frequency of $f = 2.54\,\mathrm{THz}$, a resonance position similar to that of the previous experiments, performed on the square-shaped sample, is obtained. This is an indication that the additional processing of the sample has no influence on the band structure of the material; therefore, this sample can be used for further investigations. By lowering the frequency, a more or less linear shift of the two resonances arises, as shown in Fig. 33(a). Such a dependence is expected for

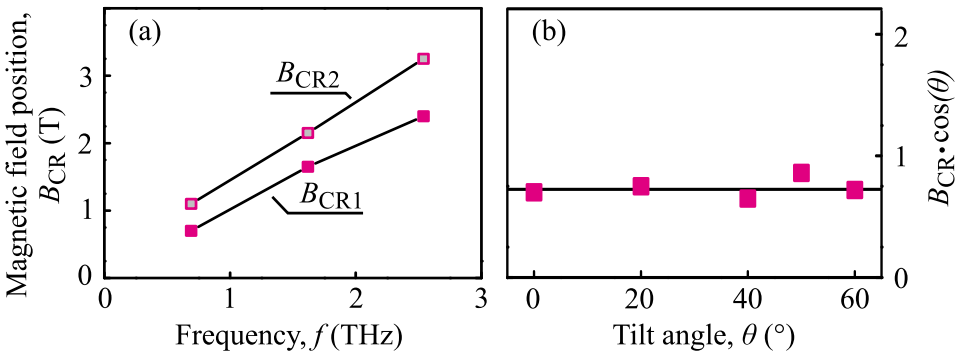

Figure 33: (a) Magnetic field positions of the first (B_{CR1}, filled squares) and the second (B_{CR2}, open squares) resonance in dependence on the excitation frequency f, obtained from photocurrent measurements shown exemplary in Fig. 29. (b) Magnetic field component normal to the surface $B_z^{\mathrm{CR}} = B_{\mathrm{CR}} \cdot \cos(\theta)$ in dependence on the tilting angle θ extracted from photocurrent measurements, as shown in Fig. 29.

CR in a system with parabolic and linear energy spectra, as seen in Eq. (14) and Eq. (35) respectively, and therefore, allows no further conclusion.

In contrast, a clear evidence that the CR arises in the 2D surface states can be found by measurements with tilted magnetic field. As seen in Sec. 2.3 the carriers move due to the Lorentz force on circular orbits normal to the magnetic field. In a 2D system the movement of the carriers is restricted to the 2D plane and therefore, only the part of the magnetic field normal to the confinement area can act on the carriers. Such a behaviour can be seen in Fig. 29, where the resonances shift to higher magnetic field values for an increased tilting angle θ. By calculating the magnetic field component normal to the surface $B_z^{\mathrm{CR}} = B_{\mathrm{CR}} \cdot \cos(\theta)$, an almost constant value of $B_z^{\mathrm{CR}} \approx 0.7\,\mathrm{T}$ is found, as seen in Fig. 33(b). This means that only the magnetic field part normal to the 2D plane acts on the carriers, which is proof of the two-dimensionality of these states.

For an in-plane magnetic field, the resonance completely vanishes (not shown). For an interpretation of this result, the thickness of the film and the cyclotron

radius r_{CR} have to be considered. The cyclotron radius r_{CR} can be calculated by [78]:

$$r_{\mathrm{CR}} = k_{\mathrm{F}} l_{\mathrm{B}}^2, \tag{32}$$

where k_F is the Fermi wave vector and l_B the magnetic length given by:

$$l_{\mathrm{B}} = \frac{\sqrt{\hbar}}{eB}. \tag{33}$$

For a carrier density of $n = 2 \cdot 10^{11}\,\mathrm{cm}^{-2}$ and a magnetic field value $B = 3.3\,\mathrm{T}$, a radius of $r_{\mathrm{CR}} \approx 22\,\mathrm{nm}$ is obtained. This value is smaller than the thickness of the film; therefore, CR for the bulk carriers should arise even for an in-plane magnetic field. Therefore, the vanishing of the resonances is another clear evidence that the resonances appear in the surface states.

Moreover, from the full width at half-maximum W of the cyclotron resonance peaks or dips, the mobility μ can be estimated by [54]:

$$\mu = \frac{e\tau}{m^*} = \frac{2}{W}, \tag{34}$$

where τ is the momentum relaxation time. For the surface states, a mobility of $\mu_{\mathrm{e}} = 5.5 \times 10^4\ \mathrm{cm}^2/\mathrm{Vs}$ is obtained from the CR dip in transmission measurements in the square shaped ungated sample at $T = 40\,\mathrm{K}$, as seen in Fig. 26(b). This value fits quite well with the mobility values obtained by magneto-transport, which are depicted in Fig. 23.

4.3.2 Fermi-Energy-Dependency

After proving with different methods that the resonances arise in the surface states, these states are further investigated with the help of gated samples. By comparing the magneto-transport data (see Fig. 24(a)) and the photocurrent measurements, the resonances can be interpreted in terms of the Fermi level position. As seen in Fig. 30(a) for $T = 40\,\mathrm{K}$ no resonances appear for a negative gate voltage, in which case the Fermi level lies in the valence band. By pushing the Fermi level into the band gap, two resonances appear, shown exemplarily for $U_{\mathrm{g}} = 0.5\,\mathrm{V}$ and $U_{\mathrm{g}} = 1.5\,\mathrm{V}$ in Fig. 30(a), and both grow in magnitude for an increasing gate voltage. This rise can be attributed to an increase in the

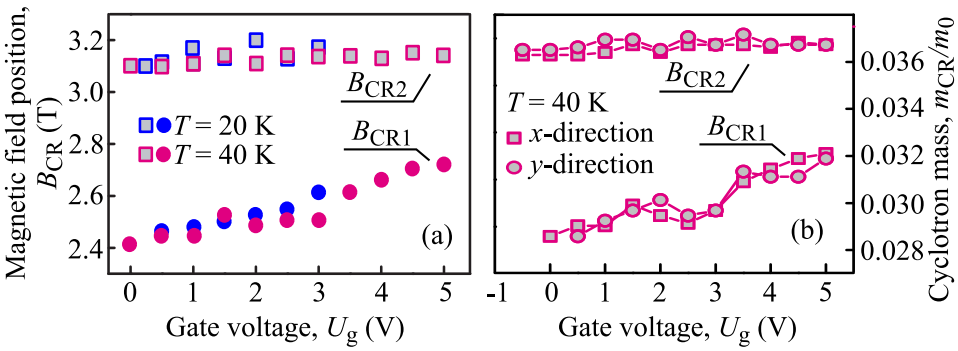

Figure 34: (a) Gate-voltage-dependence of the first and the second resonance $B_{CR1,CR2}$ for $T = 20\,\mathrm{K}$ and $T = 40\,\mathrm{K}$ obtained from measurements exemplarily depicted in Fig. 30(a) and (b) respectively. The first resonance B_{CR1} shows an almost linear dependence on the applied gate voltage, whereas the second one B_{CR2} is more or less independent of it. (b) Calculated cyclotron masses $m_{CR1,CR2}$ for two orthogonal directions for $T = 40\,\mathrm{K}$. The masses obtained from $J_x(B)$ and $J_y(B)$ are depicted in circles and squares respectively.

carrier density of the surface states, as shown in Fig. 24(c). For a higher gate voltage, where the Fermi level is located in the conduction band, the resonances remain. This is again in accordance with the transport measurements, as shown in Fig. 24.

The same characteristics are found for a temperature of $T = 20\,\mathrm{K}$. The main difference between the two temperatures is a missing peak seen for $T = 20\,\mathrm{K}$ at a magnetic field value of $B = 2.4\,\mathrm{T}$ for $U_g \geq 1.5\,\mathrm{V}$. For these gate voltage, the Fermi level lies close to the bottom of the conduction band. A possible explanation for the missing resonance could be a change in the energy dispersion of the bulk electrons due to the high gate voltage [79]. Such a so-called inversion layer can only appear for high temperatures, where a noticeable bulk electron density is present. Therefore, the disappearance of the additional resonance at $T = 20\,\mathrm{K}$ can be explained by this hypothesis. For a full understanding of this additional resonance, further study is needed, which is beyond the scope of this work.

In Fig. 34(a), the positions $B_{CR1,CR2}$ of the two resonances are depicted in dependence on the applied gate voltage U_g for $T = 20$ and $40\,\mathrm{K}$. For both

temperatures, the first resonance $B_{\mathrm{CR1}} = 2.4{-}2.7\,\mathrm{T}$ shows a strong dependence on the Fermi level position. In contrast the second resonance stays more or less fixed at a value of $B_{\mathrm{CR2}} = 3.1\,\mathrm{T}$. As expected, the same dependence can be found in the determined cyclotron masses, as depicted in Fig. 34(b). These masses are obtained from the experiments at $T = 40\,\mathrm{K}$ for the orthogonal x- and y-directions.

A similar dependence of the peak position on the carrier density is found in the sample with critical thickness, as seen in Sec. 2.4.2. To understand this rather unexpected observation, the extraordinary energy spectrum of such systems has to be considered. As depicted in Sec. 2.3, the cyclotron frequency can be expressed by $\omega_{\mathrm{CR}} \propto dE/dS$, see Eq. (16). For a linear dispersion with an energy of $E = pv_{\mathrm{DF}}$, the formula for the cyclotron frequency changes to [80,81]:

$$\omega_{\mathrm{CR}} = \frac{eBv_{\mathrm{DF}}}{p}, \tag{35}$$

where p is the momentum and v_{DF} the constant velocity of the Dirac fermions. Therefore, the cyclotron mass m_{CR} at Fermi energy E_{F} is given by:

$$m_{\mathrm{CR}} = \frac{p}{v_{\mathrm{DF}}} = \frac{E_{\mathrm{F}}}{v_{\mathrm{DF}}^2}. \tag{36}$$

With the relation $E_{\mathrm{F}} = \sqrt{2\pi n}\hbar v_{\mathrm{DF}}$ of two-dimensional Dirac fermions the cyclotron resonance position B_{CR} is given by:

$$B_{\mathrm{CR}} = \hbar\omega\frac{\sqrt{2\pi n}}{ev_{\mathrm{DF}}}, \tag{37}$$

revealing a square-root-dependence of B_{CR} on the carrier density n.

In a more illustrative way, this dependence can be seen in the Landau level splitting of a system with linear dispersion. In such a system, the l-th Landau level is given by [19, 26, 82]:

$$E_l = sgn(l)v_{\mathrm{DF}}\sqrt{2l\hbar eB}, \tag{38}$$

with $l \in \mathbb{N}$. This means that the Landau levels is no longer equidistant and the energy difference between the l-th and the $(l+1)$-st Landau levels can be calculated with:

$$\Delta E_{l,l+1} = v_{DF}\sqrt{2\hbar eB}(\sqrt{|l|} - \sqrt{|l+1|}). \tag{39}$$

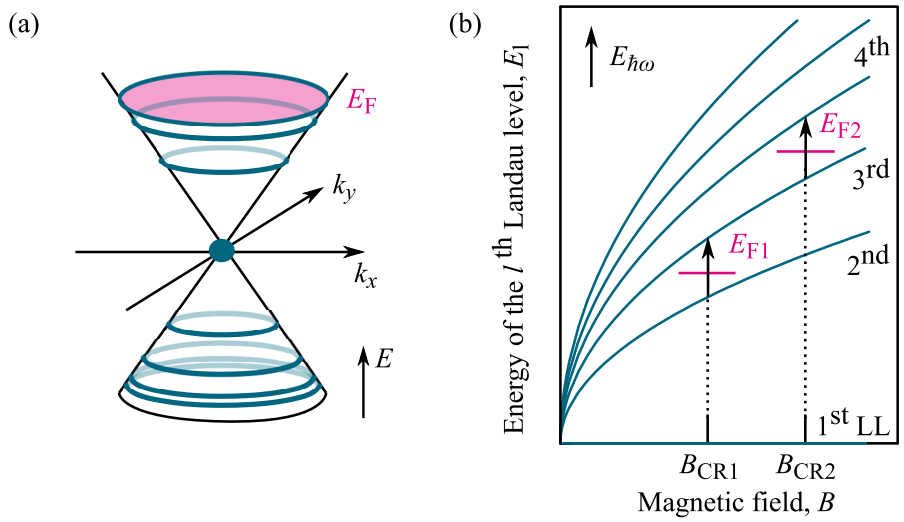

Figure 35: Schematic illustration of Landau level splitting for a system with linear dispersion. (a) Energy dispersion showing unevenly spaced Landau levels. Pictures according to Ref. [83]. (b) Magnetic-field-dependence of the Landau levels. Black arrows, representing the energy of an applied radiation $E_{\hbar\omega}$ indicate transitions between two Landau levels. Depending on the position of the Fermi level $E_{F1,F2}$, the magnetic field position jumps from B_{CR1} to B_{CR2}.

This relation is schematically depicted in Fig. 35(a).

In Fig. 35(b), Landau levels in dependence on the magnetic field are schematically depicted for the first six Landau levels. By applying radiation with an energy $E_{\hbar\omega}$, a transition between two Landau levels can occur if $E_{\hbar\omega} = \Delta E_{l,l+1}$. The corresponding magnetic field value B_{CR} of this transition can be calculated with Eq. (39). An example of such a transition is given in Fig. 35(b) between the second and the third Landau levels, by a black arrow representing $E_{\hbar\omega}$ at a given magnetic field B_{CR1}. With an increase in the carrier density and therefore, a higher position of the Fermi energy E_{F2}, a transition at the initial magnetic field value is no longer possible, as all states of the third Landau level are already occupied. A transition can then occur from the third to the fourth Landau level at a different magnetic field value of B_{CR2}.

Therefore, a strong dependency of the cyclotron resonance position on the applied gate voltage is expected for a system with Dirac fermions. The fact

that only one of the two resonances in the surface states shows this dependence leads to the assumption that the first resonance B_{CR1} corresponds to the top surface and is therefore more affected by the gate voltage, whereas the other one – belonging to the bottom surface – is almost not affected by the applied gate voltage. Such an unequal influence can also be found in the transport measurements, as shown in Fig. 24(b). The filling rates $dNn_s^{\mathrm{top/bottom}}/dU_{\mathrm{g}}$ are different, which is attributed to a screening effect, where a part of the electric field is screened by the top layer of Dirac electrons [69].

Returning to Fig. 30(c), an additional resonance is detected for gate voltages larger than $U_{\mathrm{g}} > 2\,\mathrm{V}$, where the Fermi level lies in the conduction band. This resonance can be found at a much higher magnetic field value of $B = 6.3\,\mathrm{T}$ and lower temperatures $T = 4.2\,\mathrm{K}$. From this value and the used frequency $f = 2.54\,\mathrm{THz}$, a corresponding cyclotron mass of $m_{\mathrm{CR}} = 0.07\,m_0$ is obtained. This value matches the one estimated for bulk electrons. Moreover, the resonance position does not depend on the applied gate voltage; hence, the resonance can be attributed to CR of the bulk electrons.

Moreover, from Eq. (37) and the position of the resonance, the Fermi velocity can be determined. For a photon energy of $E_{\hbar\omega} = 10.35$ meV ($f = 2.54\,\mathrm{THz}$) and a carrier density of $n_{\mathrm{e}} = 0.4 \cdot 10^{11}\,\mathrm{cm}^{-2}$, a value of $v_{\mathrm{DF}} = 5.3 \cdot 10^5\,\mathrm{m/s}$ and $v_{\mathrm{DF}} = 4.1 \cdot 10^5\,\mathrm{m/s}$ are calculated. These values are in good agreement with the velocities obtained from transmission measurements ($v_{\mathrm{DF}} = 5.2 \cdot 10^5$ m/s) in Ref. [75] and from *dc* Shubnikov-de Haas measurements ($v_{\mathrm{DF}} = 4.6 \cdot 10^5$ m/s) estimated in a 70 nm film and in Ref. [18].

4.3.3 Photocurrents at Zero Magnetic Field

For a better understanding of the origin of the photocurrents, signals excited with THz radiation under normal incidence without a magnetic field are investigated. The observed photosignals exhibit a strong dependence on the direction of the linear polarization, as shown in Fig. 25, which can be well-fitted by Eq. (30). All obtained fit parameters are summarized in Tab. 2. For systems with parabolic dispersion, the generation of such a current has already been studied in Refs. [84, 85] and is attributed to the photogalvanic effect, which is briefly outlined here.

Considering the C_1 point-group symmetry of the sample, which exhibits no symmetry except identity, all components of the tensors χ (see Eq. (6)) are linearly independent and no simplifications of Eq. (9) are possible. Therefore, the direction of the photocurrent is not restricted to a certain crystallographic axis. The dependence of the linear PGE on the azimuth angle α in x- and y-direction is given in the phenomenological theory by [23, 84]:

$$\begin{aligned} j_x &= \left[\chi_{xxy} \sin 2\alpha - \frac{\chi_{xxx} + \chi_{xyy}}{2} + \frac{\chi_{xxx} + \chi_{xyy}}{2} \cos 2\alpha \right] I\eta, \\ j_y &= \left[\chi_{yxy} \sin 2\alpha - \frac{\chi_{yxx} + \chi_{yyy}}{2} + \frac{\chi_{yxx} + \chi_{yyy}}{2} \cos 2\alpha \right] I\eta, \end{aligned} \tag{40}$$

where I is the radiation intensity and η is the free-carrier absorbance. Here, the azimuth angle α is defined by the x-axis and the plane of the linear polarization.

The measured dependence on the linear polarization of the photocurrent generated in the 80 nm film can be nicely described by Eq. (40). This allows the assumption that the current generated in this system also arises due to the PGE. A further conclusion about the origin of the excited carriers cannot be drawn as the surface states and the film itself belong to the lowest symmetry group C_1. Therefore, this work is considered as preliminary and no detailed study is performed.

4.3.4 Origin of the Photocurrent

Similar to the effect discussed in Sec. 2.4, the photocurrent in the vicinity of a magnetic field can be understood in the framework of an asymmetric excitation or relaxation of a non-equilibrium electron gas [24]. In the already discussed model, a spin-dependent term in the electron-photon interaction leads to an imbalance of the carrier distribution in $\boldsymbol{k}$-space; therefore, a pure spin-current is generated. By applying a magnetic field, this spin-current is converted into an electric current, as the spin-branches are populated differently due to the Zeeman splitting. Although this effect describes the generation in trivial HgTe QWs quite well, it cannot be applied to TIs. In these systems, a magnetic field leads only to a shift of both linear branches in $\boldsymbol{k}$-space, but no relative

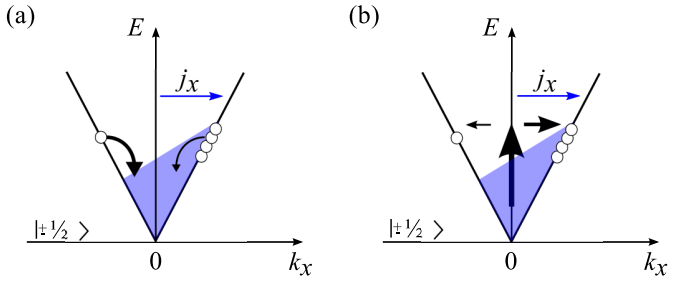

Figure 36: Schematic model of the current generation in k_x-direction due to the orbital effect for (a) the relaxation and (b) the excitation mechanisms. Thickness of arrows indicates the asymmetry of the scattering rates for carriers at positive and negative $\boldsymbol{k}$. Picture according to Ref. [86].

change of population occurs. To understand the photocurrent generation in TIs, a new model – based on an orbital effect – has to be introduced.

In contrast to the previous model, the photocurrent generation in topological non-trivial HgTe films is caused by the Lorentz force acting directly on the moving charge carriers [86,87]. The applied magnetic field leads to a correction of the scattering rate $W_{k'k}$, which scales linearly in the wave vector and in the in-plane magnetic field. For gyrotropic structures, the scattering rate can be written as [87]:

$$W_{k'k} = W_0 + \sum_{\alpha\beta} w_{\alpha\beta} B_\alpha (k_\beta + k'_\beta), \tag{41}$$

where W_0 is the scattering rate at zero magnetic field, $\boldsymbol{w}$ represents the scattering asymmetry degree and $\boldsymbol{k}$ and $\boldsymbol{k'}$ are the initial and the scattered wave vector respectively. The sum on the right-hand side of Eq. (41) leads to an asymmetric distribution of carriers in $\boldsymbol{k}$-space due to different scattering probabilities for positive and negative $\boldsymbol{k}$-states.

In Fig. 36, the current generation due to the orbital effect for (a) the relaxation and (b) the excitation mechanism is illustrated. The thickness of the black arrows indicates the different probabilities for elastic scattering events for positive and negative electron wave vectors. This difference leads to an asymmetric distribution (marked by blue area) of carriers in $\boldsymbol{k}$-space and hence to an electric current. This current can then be enhanced by the effect of CR.

Due to the spin-momentum locking in topologically protected surface states, these photocurrents are expected to be spin-polarized.

The asymmetric electron distribution in momentum space due to THz radiation, its behaviour in the magnetic field, and its decay due to scattering processes can be described with the Boltzmann equation for the distribution function $f_{\boldsymbol{p}}$ [24]:

$$e[\boldsymbol{v} \times \boldsymbol{B}] \cdot \frac{\partial f_{\boldsymbol{p}}}{\partial \boldsymbol{p}} = g_{\boldsymbol{p}} - \frac{f_{\boldsymbol{p}} - \langle f_{\boldsymbol{p}} \rangle}{\tau}. \tag{42}$$

Here, $\boldsymbol{p}$ is the electron momentum and $\boldsymbol{v}$ is the electron velocity, $g_{\boldsymbol{p}}$ is the generation rate of electrons at the state with momentum $\boldsymbol{p}$, τ is the momentum relaxation time, and $\langle f_{\boldsymbol{p}} \rangle$ is the distribution function averaged over all momentum directions. The photocurrent density $\boldsymbol{j}$ without an in-plane bias can be obtained by multiplying Eq. (42) with $e\boldsymbol{v}$ and summing it up over $\boldsymbol{p}$, accourding to $\boldsymbol{j} = \sum_{\boldsymbol{p}} e\boldsymbol{v} f_{\boldsymbol{p}}$. Considering this relation, Eq. (42) can be rewritten as:

$$-\boldsymbol{j} \times \boldsymbol{\omega}_{\mathrm{CR}} = \boldsymbol{G} - \frac{\boldsymbol{j}}{\tau}, \tag{43}$$

where $\boldsymbol{\omega}_{\mathrm{CR}} = \omega_{\mathrm{CR}} \hat{\boldsymbol{z}} = eB_z/m_{\mathrm{CR}}$ is the cyclotron frequency, $\hat{\boldsymbol{z}}$ is the unit vector pointing along the z-axis, and $\boldsymbol{G} = \sum_{\boldsymbol{p}} e\boldsymbol{v} g_{\boldsymbol{p}}$ is the current generation rate.

The current generation rate $\boldsymbol{G}$ is determined by the scattering of the surface state carriers with phonons or static defects and by the radiation absorbance. For the system investigated here with C_1 point-group symmetry, the scattering rate comprehends asymmetric terms even for a magnetic field perpendicular to the sample surface. As mentioned before, the scattering in the surface plane is not forced to a certain crystallographic axis. The photocurrent generation rate $\boldsymbol{G}$ is given for an applied magnetic field B_z by:

$$\boldsymbol{G} = \boldsymbol{\gamma} I \eta(\omega) B_z. \tag{44}$$

Herein, I is the radiation intensity, $\eta(\omega)$ is the absorbance and $\boldsymbol{\gamma}$ is the vector defined by the magnetic field-induced asymmetry of the electron scattering process. The direction of $\boldsymbol{\gamma}$ can depend on temperature, the applied gate voltage, the radiation frequency, etc. This explains the rather unpredictable photocurrent direction of the two resonances on the magnetic field direction.

Using Eq. (43), it can be shown that the currents in x- and y-direction are described by [24]:

$$\begin{aligned} j_x &= \frac{\gamma_x + \omega_{\mathrm{CR}}\tau\gamma_y}{1+(\omega_{\mathrm{CR}}\tau)^2} I\eta(\omega)B_z, \\ j_y &= \frac{\gamma_y + \omega_{\mathrm{CR}}\tau\gamma_x}{1+(\omega_{\mathrm{CR}}\tau)^2} I\eta(\omega)B_z. \end{aligned} \tag{45}$$

With Eq. (45), the main features of the experimental results can be explained. On the one hand, the photocurrents j_x and j_y show a resonant behaviour at $\omega = \omega_{\mathrm{CR}}$ due CR. The absorbance η in the surface states of the HgTe film has the same form as the one found in QWs with critical thickness given by Eq. (28), but without the prefactor of two. This difference arises because the surface states have one Dirac cone in the Brillouin zone, whereas HgTe QWs at critical thickness have two cones. The dependence on the absorbance explains all characteristic aspects of CR in a linear dispersion, e.g. the strong helicity-dependence, the dependence of the CR-position on the carrier density etc. On the other hand, Eq. (45) contains even and odd contributions in the magnetic field. This behaviour is found in many sets of experimental data and is for example depicted in Fig. 31.

In Fig. 37, the formation of the photocurrent for (a) a positive and (b) a negative magnetic field is sketched. For the positive magnetic field, the photocurrent is generated along the positive x- and y-directions. Due to the Hall effect, the generated electrons are shifted by an angle of $\arctan(\omega_{\mathrm{CR}}\tau)$. By inverting the magnetic field polarity, the photocurrent generation rate $\boldsymbol{G}$ changes its sign. Although $arctan(\omega_{\mathrm{CR}}\tau)$ changes its direction, the $\boldsymbol{j}$ components j_x and j_y may or may not change their directions. An example is given in Fig. 37(b), where j_y remains positive and j_x becomes negative. The exact parity of the signal depends on the direction of the photocurrent rate $\boldsymbol{G}$ relative to the contacts and the magnetic field strength, which determines the Lorentz force acting on the carriers. In addition, the generation rate $\boldsymbol{G}$ depends on temperature, gate voltage, radiation frequency, etc. Therefore, every combination of parity is possible, which is in full accordance with the experimental results.

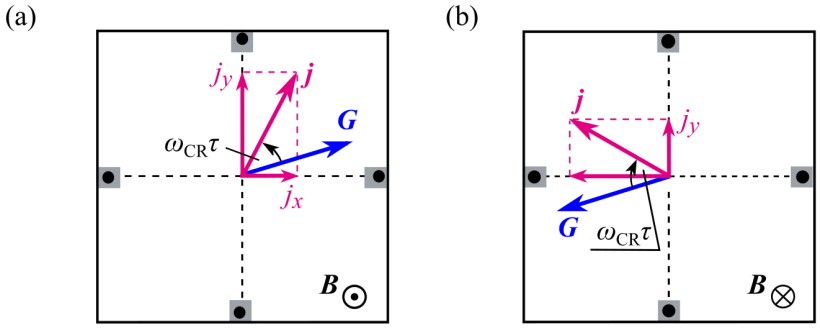

Figure 37: Sketch of the photocurrent generation rate $\boldsymbol{G}$ and the steady-state photocurrent $\boldsymbol{j}$ for two opposite magnetic field directions. Due to the Hall effect, the direction of the resulting photocurrent $\boldsymbol{j}$ deviates from the direction of the photocurrent generation rate $\boldsymbol{G}$. In the example illustrated here, j_x changes its sign upon a change of the magnetic field direction, while j_y does not.

4.4 Brief Summary

In this chapter, the presence of surface states in 3D topological insulators based on 80 nm fully strained HgTe films is proved. This is done by means of cyclotron-resonance-enhanced THz radiation-induced photocurrents, accompanied by measurements of THz radiation transmission as well as magneto-transport. The arising resonances can be attributed clearly to states lying either in the surface or in the conduction band of the studied system.

First, the nature of the two main resonances found in photosignals and in transmissions measurements is investigated with different techniques. Although the Fermi level for the ungated systems lies somewhere in the valence band, these resonances show a clear behaviour of electrons, as shown in Fig. 26. Moreover, the experimentally obtained cyclotron masses ($m_{\mathrm{CR1}}^{\mathrm{top}} = 0.028\,m_0$ and $m_{\mathrm{CR2}}^{\mathrm{bottom}} = 0.036\,m_0$) for the top and bottom surfaces fit perfectly the ones estimated from $\boldsymbol{k}\cdot\boldsymbol{p}$ calculations for these states. The origin of the resonances is further confirmed by measurements in tilted magnetic fields, as shown in Figs. 29 and 33. The shift of the resonances in regard to the tilting angle is

an experimental proof of the 2D character of the investigated carriers, which allows an assignment to the surface states.

In addition, the obtained resonances are investigated as a function of the Fermi level position (see Figs. 30 and 34). In this study, it is shown that the resonances completely vanish for a Fermi level located deep in the valence band. In contrast, they are distinctly resolved for Fermi levels in the bulk gap and in the conduction band. This finding is in full accordance with the calculated band structure. Moreover, one of the resonances exhibits a strong dependence on the applied gate voltages, which can be explained with the non-equidistant splitting of the Landau levels of a Dirac fermion system, characterized by a linear dispersion.

Furthermore, a microscopic model based on asymmetric excitation or relaxation caused by the Lorentz force acting on the moving charge carriers is introduced. The photocurrent described by Eq. (45) exhibits a resonant behaviour due to the CR-enhanced absorbance and behaves evenly or oddly in the magnetic field. Both features are in full accordance with the experiments. Moreover, the currents are expected to be spin-polarized due to the spin-momentum locking of the surface electrons.

In general, this work proves, that CR-assisted photocurrents provide a sensitive method to probe the cyclotron mass and the mobility of 2D Dirac surface states, even for micrometre-sized samples and for samples with a Fermi level lying in the conduction band, where transmission measurements are hardly possible.

5 Photocurrents in 1D Edge States

In this chapter, two-dimensional topological insulators based on 8 nm HgTe QWs are investigated. It is demonstrated that photocurrent spectroscopy can be effectively used to probe the helical edge states of this system without applying a magnetic field. In particular, it is observed that exciting the system with circularly polarized terahertz laser radiation results in circular photogalvanic currents in a wide range of applied gate voltages. Depending on the exact Fermi level position, the photosignal has different origins, which are outlined and discussed. All results presented herein are published in Ref. [25].

5.1 Sample Characterization

For the characterization of the studied samples, magneto-transport measurements are performed at the helium temperature. The obtained curves exhibit a conductance of $2e^2/h$, which is typical for the ballistic transport in topological insulators. In Fig. 38, representative curves of the four-terminal conductance G are shown for two different contact pairs of one of the investigated Hall-bars, labelled as # 1. For these measurements, the current is applied between contacts 1 and 6 and the voltage drop is measured between contact pairs $4-5$ and $3-5$, which have a significantly different spacing. The used contact numbering is depicted in the inset of Fig. 38. For both of these contact pairs, a strong dependency on the conduction on the applied gate voltage is found.

For small applied gate voltages ($U_\mathrm{g} < -0.4\,\mathrm{V}$), the Fermi level lies in the bulk valence band, indicated by a large conductance. By increasing the applied gate voltage, a minimum conduction is reached. The exact value of the minimum shows a significant dependence on the distance of the used contacts. For the shorter distance ($l_{54} = 2.8\,\mu\mathrm{m}$), shown in red, a plateau value of $G = 2e^2/h$ for a gate voltage range of $U_\mathrm{g} \approx -0.2$ to $0.2\,\mathrm{V}$ is found. This value demonstrates that the system is tuned into the quantum spin Hall regime [17], where the transport only arises in the topological protected edge states. In contrast, for the larger contact spacing ($l_{53} = 8.6\,\mu\mathrm{m}$), the plateau value decreases to almost $G = e^2/h$. This reduction can be attributed to a higher probability of electron spin-flip scattering, meaning that the transport is no longer perfectly

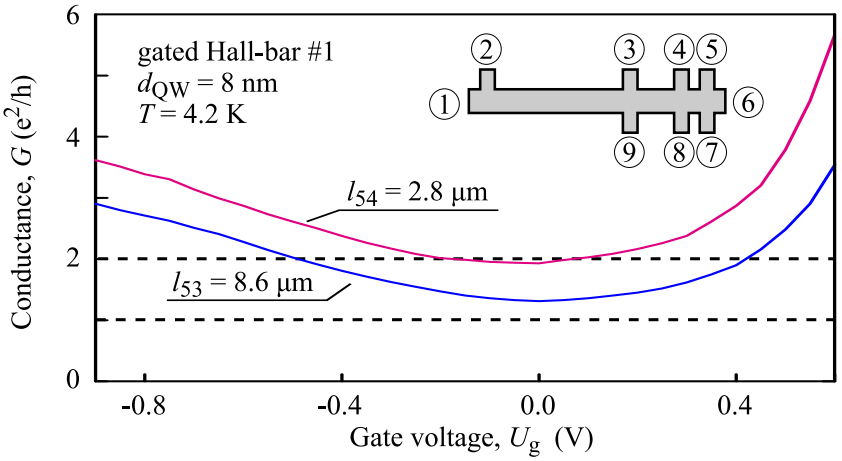

Figure 38: Longitudinal conductance G of the Hall-bar # 1 for two contact pairs (4-5) and (3-5). The measurement across the shorter spacing of $l_{54} = 2.8\,\mu m$ exhibits a quantized conductance value of $G = 2e^2/h$, indicating the quantum spin Hall regime. For the larger contact spacing of $l_{53} = 8.6\,\mu m$, the minimum value decreases to almost $G = e^2/h$. The inset depicts the layout of the sample and the used contact numbering.

ballistic [17, 88]. By applying a large positive gate voltage, the Fermi level is shifted into the bulk conduction band, resulting again in a high conduction.

Note that – similar to the measurements in the 80 nm HgTe film (see Sec. 4.1) – a cool-down dependent charge-trapping occurs, which shifts the charge neutrality point in regard to the applied gate voltage. To enable a comparison between different measurements, all data are plotted as a function of the normalized gate voltage, $U_g = U_{applied} - U_{CNP}$.

5.2 Photocurrent Experiments

By illuminating 8 nm HgTe Hall-bars with circularly polarized radiation under normal incidence, a photosignal is observed between any of the contacts along one edge of the sample in a wide range of gate voltages. Here, only experimental data obtained at the helium temperature are presented. For details on the experimental setup of the photovoltage measurements see Sec. 3.2.2.

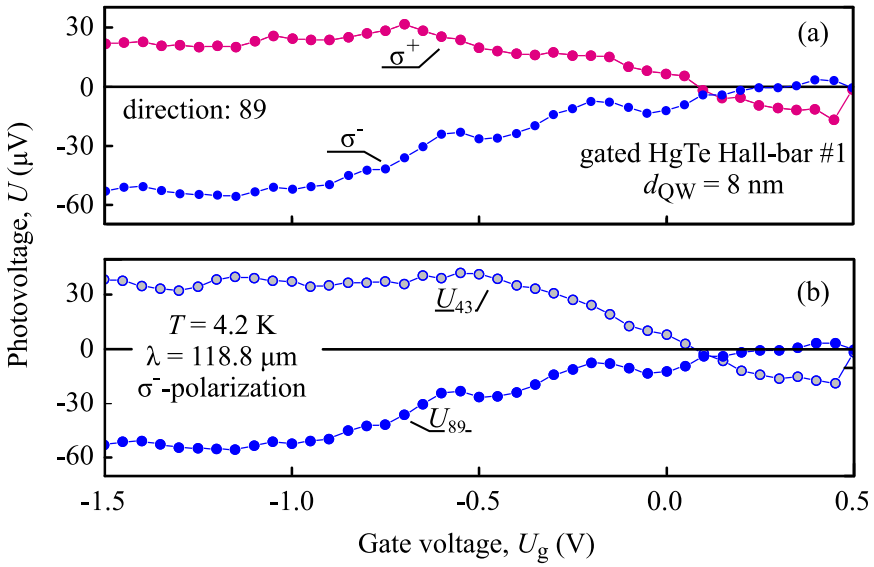

Figure 39: Gate-voltage-dependence of the photovoltage U obtained in the gated HgTe Hall-bar # 1 at $T = 4.2\,\mathrm{K}$. (a) The signals measured in the direction $8-9$ exhibits opposite signs for right- (σ^+) and left-(σ^-) circularly polarized radiation. (b) Photoresponse of two opposite sample edges for a fixed helicity (σ^-) showing consistently different polarity.

In Fig. 39(a), photovoltage measurements between the contacts $8-9$ are depicted with a dotted red line for an excitation with right-handed circularly polarized radiation. In the whole gate voltage range, a photosignal can be found. For positive gate voltages, a negative photosignal can be detected. Near the CNP ($U_\mathrm{g} = 0.1\,\mathrm{V}$), it changes sign, increases and saturates at a value of $U \approx 20 - 25\,\mu\mathrm{V}$ by reducing U_g to $-1.5\,\mathrm{V}$. By changing the helicity from σ^+ to σ^-, the polarity of the photosignal changes in the entire investigated gate voltage range. Otherwise, the dependence on U_g remains similar to the previous one, with only a slightly higher saturation value of $U \approx -50\,\mu\mathrm{V}$ for negative gate voltages.

The data curve obtained with σ^- is replotted in Fig. 39(b), together with the photosignal measured at the opposite sample edge (contacts 3-4). This signal again shows a consistently different polarity compared to the one measured for contacts $8-9$. This indicates that the photoresponse stems from a photocurrent

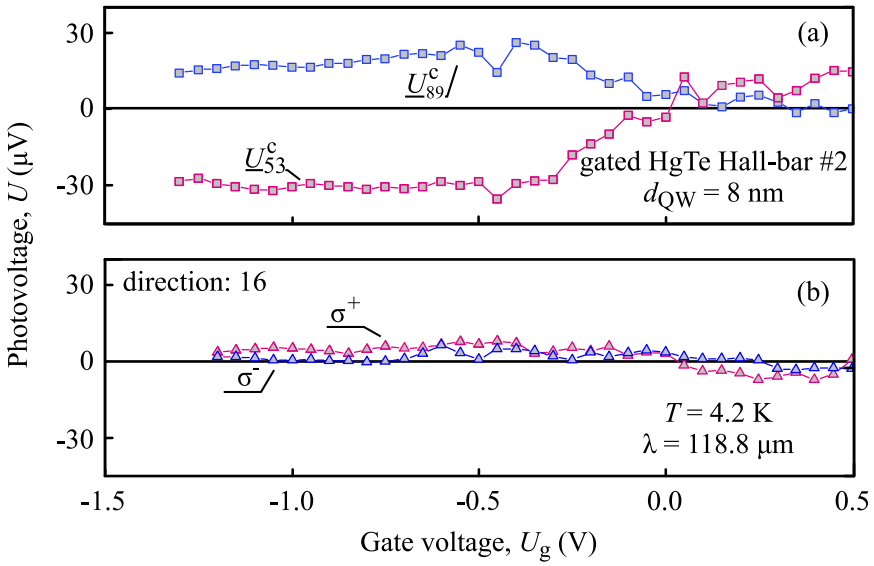

Figure 40: (a) Helicity-sensitive photoresponse U^c in dependence of the gate voltage obtained from measurements performed on Hall-bar # 2 for two opposite edges. For both edges ($8-9$ in blue and $5-3$ in red), a strong helicity-dependent signal that changes its sign near the CNP is obtained. (b) Photovoltage U_{16} is obtained across the sample.

flowing along the sample edges, where the direction of the current flow is determined by the helicity of the applied radiation.

A similar behaviour is observed in a number of samples. In Fig. 40(a), the helicity-dependent signal of a second Hall-bar sample (#2) is depicted, which can be calculated by:

$$U^c_{nm} = \frac{U_{nm}(\sigma^+) - U_{nm}(\sigma^-)}{2}, \tag{46}$$

where $U(\sigma^+)$ and $U(\sigma^-)$ are the voltages obtained for right- and left-handed circularly polarized radiations respectively and n and m are the used contacts. The signals U^c for Hall-bar #2 show opposite polarities for opposite edges and saturate at a value of $U^c \approx \pm 15 - 30\,\mu$V. They change their signs near the CNP.

The conclusion that these helical photosignals mainly flow along the edges of the sample is further confirmed by the fact that the photosignal almost

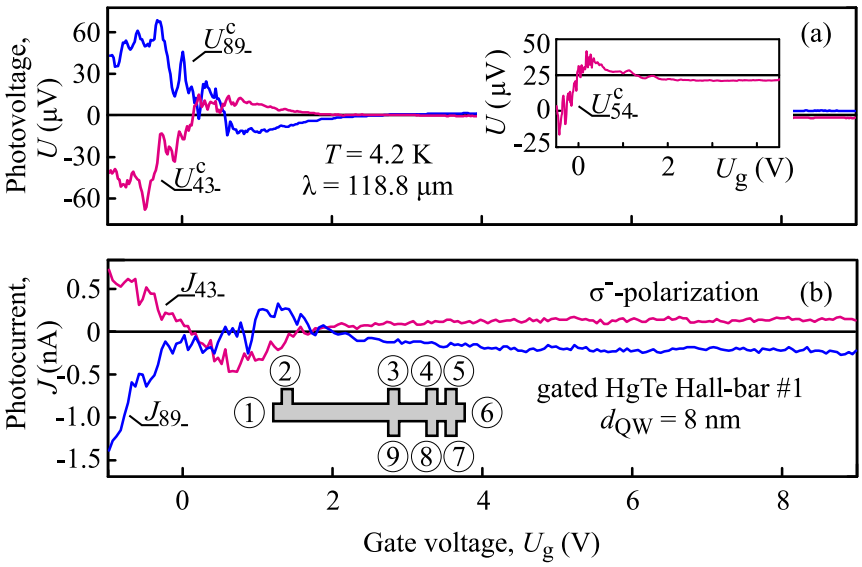

Figure 41: (a) Helicity-sensitive photosignal U^c measured over a large gate voltage range obtained for Hall-bar # 1 for the two opposite edges. The inset in (a) shows U^c measured over the smallest contact spacing. (b) Photocurrent J for left-handed polarized radiation for the two opposite edges. The inset in (b) shows the sample layout with the contact numbering.

vanishes for measurements across the sample. In such a case, the two counter-propagating currents along the opposite edges compensate each other and no measurable electric current arises. Such a dependency is depicted in Fig. 40(b), obtained between contacts $1-6$ for σ^+ (red line) and σ^- (blue line).

In Fig. 39(a) and (b), a second change of sign can be assumed at $U_g \approx 0.5\,\mathrm{V}$. To explore this feature further, the cool-down procedure is modified, enabling the study of photosignal at larger positive gate voltages. In Fig. 41(a), the helicity-dependent photovoltage curves U^c for two opposite edges measured across contact pairs $4-3$ (red line) and $8-9$ (blue line) are depicted. A strong signal for negative gate voltages is found, which decreases in the vicinity of the CNP. In contrast to the previous measurements, a second inversion point at $U_g \sim 2\,\mathrm{V}$ is now clearly detectable. A similar result is obtained for U^c_{54} measured over the smallest contact spacing of $l_{54} = 2.8\,\mu\mathrm{m}$, as depicted in the inset of Fig. 41(a).

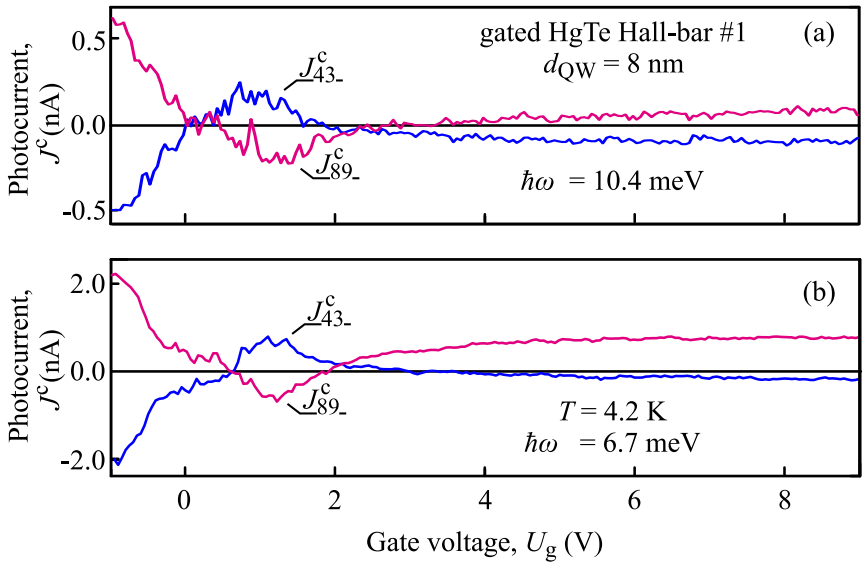

Figure 42: Helicity-sensitive photocurrent J^c obtained at two opposite edges at contact pairs $4-3$ (blue) and $8-9$ (red) for (a) $\hbar\omega = 10.4\,\text{meV}$ and (b) $\hbar\omega = 6.7\,\text{meV}$.

In Fig. 41(b), the photocurrents J obtained across the contact pairs $4-3$ and $8-9$ are depicted. For details of the photocurrent measurements see Sec. 3.2.2. Similar to the photovoltage curves, two sign changes are clearly observable, at $U_g = 0\,\text{V}$ and $U_g \approx 2\,\text{V}$. The only significant difference between the results for the two measurement methods is that stronger photocurrent signals are obtained for high positive gate voltages.

From these traces, the helicity-dependent signal is given by:

$$J^c_{nm} = \frac{J_{nm}(\sigma^+) - J_{nm}(\sigma^-)}{2}, \tag{47}$$

where $J_{nm}(\sigma^+)$ and $J_{nm}(\sigma^-)$ are the photocurrents obtained in nm-direction for right- and left-handed circularly polarized radiation respectively. The acquired traces are depicted in Fig. 42(a) for the two opposite edges ($4-3$ and $8-9$) for a radiation energy of $\hbar\omega = 10.4\,\text{meV}$ ($\lambda = 118\,\mu\text{m}$), which shows the already well-known behaviour. By changing the radiation energy from $\hbar\omega = 10.4\,\text{meV}$ to $\hbar\omega = 6.7\,\text{meV}$, a similar behaviour of the helicity-dependent photocurrent with a generally higher magnitude is found, as shown in Fig. 42(b). The main difference in these two signals is the position of the zero

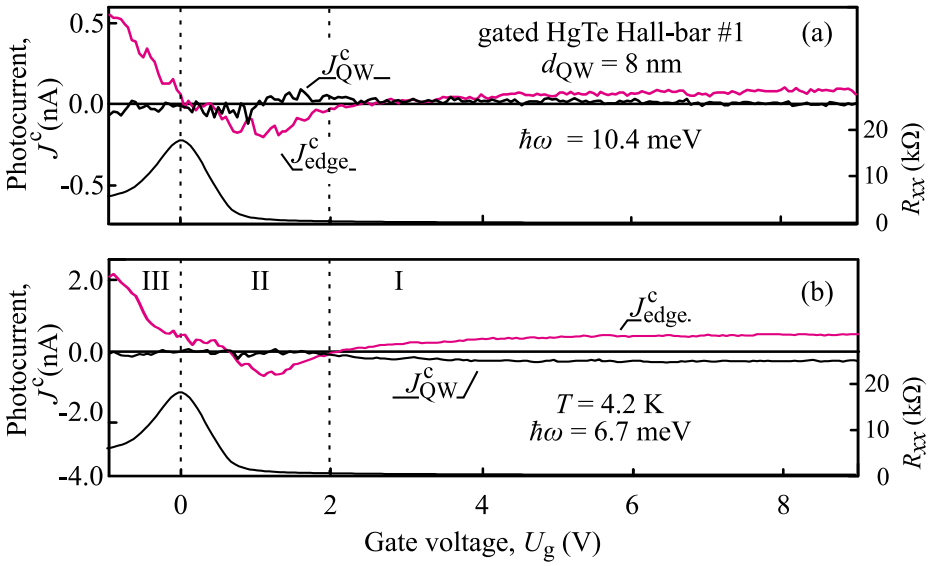

Figure 43: Edge J^c_{edge} (red line) and QW J^c_{QW} (black line) contribution to the photocurrent obtained for radiation energies of (a) $\hbar\omega = 10.4\,\text{meV}$ and (b) $\hbar\omega = 6.7\,\text{meV}$. Black solid lines at the bottom of each graph represent the respective resistance measurements between contacts $3-4$ (right scale). The photocurrents can be grouped in three regions, depicted as I, II and III in (b).

crossings. The first change of sign shifts to higher gate voltages of $U_g \approx 0.5\,\text{V}$ for the smaller excitation energy, whereas the second change of sign stays fixed at $U_g \approx 2\,\text{V}$.

As the edge currents (J_{43} and J_{89}) at opposite sides of the sample have opposite directions, the pure edge contribution J^c_{edge} can be obtained by subtracting these currents:

$$J^c_{edge} = \frac{J^c_{43} - J^c_{89}}{2}, \tag{48}$$

and the bulk contribution J^c_{QW} can be determined by summing up the two currents:

$$J^c_{QW} = \frac{J^c_{43} + J^c_{89}}{2}. \tag{49}$$

The obtained traces are depicted in Fig. 43 for radiation energies of (a) $\hbar\omega = 10.4\,\text{meV}$ and (b) for $\hbar\omega = 6.7\,\text{meV}$. The traces in Fig. 43(a) indicate that

almost the whole photocurrent flows in the edges of the sample for the higher photon energy, exhibiting the already well-known behaviour. The contribution of the bulk of the QW can almost be neglected for this radiation energy. In contrast, for a radiation energy of $\hbar\omega = 6.7\,\mathrm{meV}$, a clearly evident QW contribution to the current arises for gate voltages higher than $U_\mathrm{g} < 2\,\mathrm{V}$. In addition, the corresponding resistance R_{xx} measured between contacts $3-4$ is depicted in Fig. 43(a) and (b), scaled at the right axis.

To summarize, by illuminating a 8 nm HgTe QW, a helicity-sensitive photosignal arises. This photosignal flows – depending on the position of the Fermi level – mainly at the edge or in the bulk of the sample. All of these obtained traces can be grouped into three regions, which are marked by I to III in Fig. 43(b). In region I ($U_\mathrm{g} > 2\,\mathrm{V}$), a constant helicity-sensitive edge photosignal is found over a wide range of applied gate voltages. Near $U_\mathrm{g} = 2\,\mathrm{V}$, this edge photosignal decreases for decreasing gate voltages and then changes its sign, defining the beginning of region II ($0\,\mathrm{V} > U_\mathrm{g} < 2\,\mathrm{V}$). In region II, the edge photosignal remains negative, reaches a minimum, and increases again till a second change of sign occurs. At this point, region III ($U_\mathrm{g} < 0\,\mathrm{V}$) begins, where the signal increases and a strong helicity-sensitive edge photosignal is observed.

5.3 Discussion

In Sec. 5.1, photon helicity-sensitive photosignals flowing in the edges and in the bulk of the sample are observed, which are grouped into three regions. In the following section, the origin of the photocurrents is discussed for each region separately. The main focus of this discussion lies on region II. It is shown that the photocurrent in this region is caused by a photoionization of helical edge electrons to the conduction band. For this phenomenon, a microscopic model is introduced, which was developed simultaneously to the experiments by Mikhail V. Durnev[6] and Sergey A. Tarasenko[6]. Here, only the main features of Ref. [25] are given, without any derivation of the equations.

[6]Ioffe Institute, St. Petersburg, Russia

5.3.1 Photocurrents in the Conduction Band Regime

First, the origin of the photocurrent in region I, which comprises gate voltages larger than $U_\mathrm{g} \approx 2\,\mathrm{V}$, is discussed. Following the transport measurement depicted at the bottom of Fig. 43(b) for the corresponding cooling circle, the Fermi level in this region lies in the conduction band. Therefore, the bulk and the edge photocurrents are formed by conduction band (bulk) carriers.

The generation of a helicity-sensitive photocurrent flowing in the bulk of HgTe QWs can be understood in the framework of the circular photogalvanic effect. This effect is investigated by Wittmann *et al.* in Ref. [84] for QWs with $d_\mathrm{QW} = 8\,\mathrm{nm}$ and $d_\mathrm{QW} = 21\,\mathrm{nm}$. By considering the C_1 point-group symmetry of the sample, all components of the tensor χ are linearly independent and no simplification of Eq. (9) is possible. For an excitation of a QW with elliptically polarized radiation under normal incident, the currents in x- and y-direction are given by [84]:

$$j_x = \left[\gamma_{xz}\sin 2\varphi - \frac{\chi_{xxx}+\chi_{xyy}}{2} + \frac{\chi_{xxx}-\chi_{xyy}}{4}(1+\cos 4\varphi) + \frac{\chi_{xxy}}{2}\sin 4\varphi\right] I\eta, \quad (50)$$

$$j_y = \left[\gamma_{yz}\sin 2\varphi - \frac{\chi_{yxx}+\chi_{yyy}}{2} + \frac{\chi_{yxx}-\chi_{yyy}}{4}(1+\cos 4\varphi) + \frac{\chi_{yxy}}{2}\sin 4\varphi\right] I\eta, \quad (51)$$

where γ_{xz} is a second-rank pseudo-tensor, I the radiation intensity, and η the free-carrier absorbance. Note that γ and χ strongly depend on parameters like the temperature or the wavelength of the used radiation. Such a dependence is also found in the measurements, as a helicity-sensitive bulk photosignal J^c_QW arises only for a radiation with an energy of $\hbar\omega = 6.7\,\mathrm{meV}$, as shown in Fig. 43.

In addition to this bulk photosignal, a considerable contribution from the edge of the sample is found in this region, as shown in Fig. 43. This helicity-sensitive photocurrent ($J^\mathrm{c}_\mathrm{edge}$) is caused by diffuse scattering on the sample boundaries. A similar effect has been observed earlier in graphene [89, 90], QW structures

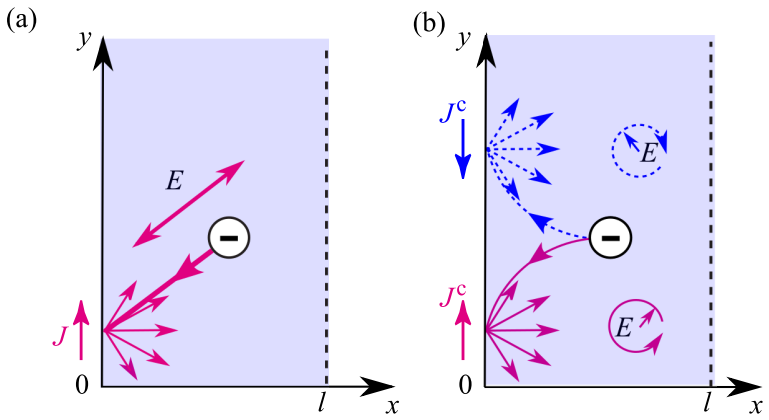

Figure 44: Schematic picture of the edge photocurrent generation in bulk states. (a) The electric field E of linearly polarized radiation acts on the carriers. The current arises due to a diffusive scattering of the carriers (here electrons) at the boundary of the sample. (b) The electric field E of the right- (solid red line) or left-handed (dotted blue line) circularly polarized radiation forces the carriers on clockwise or counterclockwise trajectories respectively. Again, the current arises due to a diffusive scattering of the carriers at the boundary of the sample. Picture according to Refs. [89, 90].

[91], and bulk materials [92, 93] for linear and circular polarization, and is briefly outlined here.

In the framework of this mechanism, the edge contribution of the photosignal is generated in a narrow stripe within the mean free path l at the sample boundary. Far from this stripe ($x > l$), the electric field of the applied radiation results only in a oscillation of the charges without a generation of a current. However, for an electron inside from the mean free path, the carrier follow the electric field and are pushed towards the boundaries of the sample, as shown in Fig. 44(a). There the charges are diffusive scattered, which results in a random velocity at the boundary. This destruction of the balance between the back and forth motion of the carrier results in a measurable edge photocurrent. A similar effect is found for circularly polarized radiation, as shown in Fig. 44(b). There the direction of the arising current depends on the helicity of the applied radiation.

The microscopic theory of the effect can be developed in the framework of the Boltzmann kinetic equation [89]. The electron distribution $f(\boldsymbol{p}, x, t)$ is given by:

$$\frac{\delta f}{\delta t} + \nu_x \frac{\delta f}{\delta x} + q\boldsymbol{E}(t)\frac{\delta f}{\delta \boldsymbol{p}} = Q\{f\}, \tag{52}$$

where $\boldsymbol{p}$ is the momentum, x is the coordinate of the carrier, $\boldsymbol{E}(t) = \boldsymbol{E}_0 e^{-i\omega t} + \boldsymbol{E}_0^* e^{+i\omega t}$ is the electric field of the radiation, ν_x is the electron velocity in x-direction and q is the carrier charge, with $q = +|e|$ for holes and $q = -|e|$ for electrons. The parameter $Q\{f\}$ is the collisions integral which can be described by:

$$Q\{f(\boldsymbol{p}, x, t)\} = -\frac{f(\boldsymbol{p}, x, t) - f_0(\epsilon_p)}{\tau}, \tag{53}$$

with τ being the scattering time and ϵ_p the electron energy.

By expanding the distribution function in powers of the electric field and taking the boundaries into account, the edge current generation in a degenerated electron gas is given by:

$$J_y \sim -\frac{\tau^3}{[1+(\omega\tau)^2]}\left[\frac{\omega\tau}{1+(\omega\tau)^2} i\left[\boldsymbol{E}_0 \times \boldsymbol{E}_0^*\right]_z + \left(\frac{1-(\omega\tau)^2}{1+(\omega\tau)^2}\right)\left(E_{0,x}E_{0,y}^* + E_{0,y}E_{0,x}^*\right)\right]. \tag{54}$$

The first term includes the helicity-dependent current, whereas the second term describes the photocurrent caused by linearly polarized radiation. The model demonstrates that the current is caused by a movement of the carrier towards the edges and involves a retardation of the electron motion compared to the instantaneous electric field. With the help of this model, the arising helicity-dependent edge photocurrent in region I can be fully understood.

5.3.2 Topological Edge Current

For applied gate voltages smaller than $U_\mathrm{g} \approx 2\,\mathrm{V}$, corresponding to the start of region II, the Fermi level crosses the bottom of the conduction band and enters the bulk gap. As for these gate voltages, no bulk carriers are present,

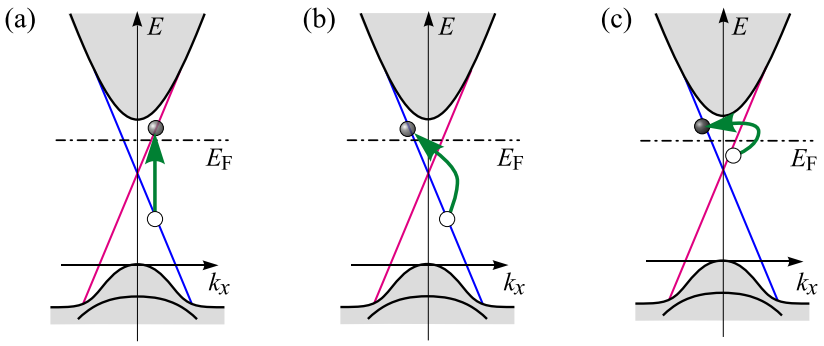

Figure 45: Schematic illustration of possible transitions in region II. (a) Direct inter-band transition between the spin-up and the spin-down branches of the linear edge states and indirect (b) inter-band and (c) intra-band transitions. Picture according to Ref. [90]

the aforementioned mechanism can no longer be effective. This is clearly seen for the bulk photocurrent, which vanishes on entering region II. Moreover, the edge photocurrent changes its sign, rises until a maximum is reached at $U_g \approx 1\,\mathrm{V}$, and decreases again. Such a behaviour cannot be explained in the framework of the model described in Sec. 5.3.1. Therefore, a new effect of optical transitions involving the topological edge states has to be considered in order to understand the photocurrent generation in this region.

There are several possible transitions, that can lead to a photocurrent generation in the bulk gap. First, there are direct transitions between the spin-up and the spin-down branches of the linear edge states, as shown in Fig. 45(a). These currents are expected to show the observed helicity-dependence, as the probability for e.g. transitions from the spin-up to the spin-down branch is different for the two helicities [94]. In total the probability for such transitions is low [95]. Moreover, the generated current would show a maximum near the Dirac point, which is not observed in the here presented experiments. Therefore, this effect cannot be the origin of the investigated currents.

Other possible mechanisms could be indirect inter-band or intra-band transitions, as depicted in Fig. 45(b) and (c) respectively. These transitions require an additional scattering and a k-dependent velocity; therefore, their probability again is rather small.

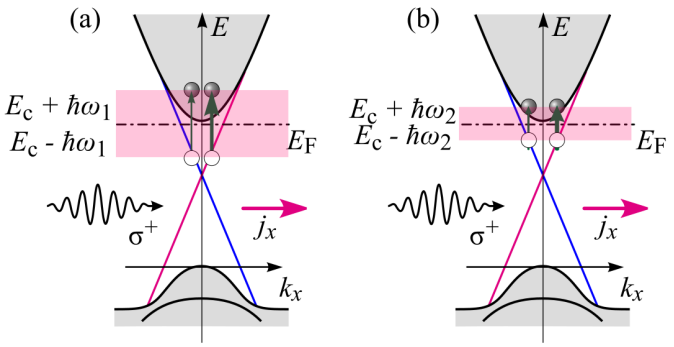

Figure 46: Schematic picture of the photoionization of helical states into the conduction band for a Fermi level in region II. Green arrows indicate the transitions for photon energies of (a) $\hbar\omega_1$ and (b) $\hbar\omega_2$, with $\omega_1 > \omega_2$. Due to a difference in the optical transition probabilities for spin-up and spin-down states, a photocurrent j_x is generated.

A fourth candidate for the generation of photocurrents in the gap are localized electron states, which may exist in the bulk band gap of HgTe/CdHgTe QWs. Such so called charge puddles are discussed as a possible source of backscattering in helical channels in Refs. [96–98] and can lead to a photocurrent generation by enhancing the Drude absorption. Again, the expected contribution of this effect should be small, as the density of the trivial states localized at the edges is much smaller than that of the helical states. Moreover, the photoresponse measured over the shortest contact spacing is equivalent to the measurements over the larger distances. As these shorter part of the edge shows perfect ballistic transport, such charge puddles cannot be the origin of the arising photocurrent.

The last and most likely candidate for the generation of the circular edge photocurrent in region II is the excitation of electrons from helical edge states to bulk conduction band states [95, 99]. This effect is similar to the photocurrent generation in semiconductor QWs due to inter-subband transitions, which is discussed in Sec. 2.2. Therefore, this effect is also referred to as the 'photoionization' of edge channels.

In Fig. 46(a), this photoionization mechanism is depicted for an excitation with right-handed circularly polarized radiation, with a photon energy of $E_1 = \hbar\omega_1$.

For a Fermi level E_F in region II, but still in the vicinity of the conduction band, Dirac states are depopulated by exciting them into the bulk states. In the case of right-handed circularly polarized radiation, the probability of optical transitions from spin-up states ($s = +1/2$, red line) is higher than that of transitions from spin-down states ($s = -1/2$, blue line), as indicated by the thickness of the vertical arrows. Due to this difference in the transition rates, the remaining population of the edge states exhibits an imbalance in k_x, which leads to a photocurrent generation in x-direction. For an excitation with left-handed circularly polarized radiation, the transitions from the spin-down states dominate and the generated photocurrent reverses its sign. This behaviour is found in the measurements, as shown in Fig. 42.

Considering the fact that the initial state of the transition has to be occupied and the final one has to be empty, a photocurrent can be excited in an energy range of $E_\mathrm{c} - \hbar\omega < E_\mathrm{F} < E_\mathrm{c} + \hbar\omega$. This means that a decrease in the photon energy reduces the range of gate voltages in which a photocurrent is generated, as shown in Fig. 46(b). Exactly such a behaviour is found by changing the photon energy from $\hbar\omega = 10.4\,\mathrm{meV}$ to $\hbar\omega = 6.7\,\mathrm{meV}$, as depicted in Fig. 43(a) and (b).

The rate of the photoionization $g_{k_x s}$ of electrons from the edge states into the conduction band can also be theoretical described by Fermi's golden rule, as given in the supplemental material of Ref. [25]:

$$g_{k_x s} = \frac{2\pi}{\hbar} \sum_{k_y} |M_{s's}(k_x, k_y)|^2 \left[f_0(\epsilon_{k_x s} - f_0(\epsilon^\mathrm{c}_{k_x k_y s}) \right] \delta \left(\epsilon^\mathrm{c}_{k_x k_y s} - \epsilon_{k_x s} - \hbar\omega \right). \quad (55)$$

Here, f_0 is the equilibrium distribution, $\epsilon^\mathrm{c}_{k_x k_y s}$ is the energy of the conduction band states, and $\epsilon^\mathrm{c}_{k_x s}$ is the energy of the edge states, where $k_{x/y}$ are the wave vectors in the x- and y-directions respectively, and s is the pseudo-spin index. The matrix element $|M_{s's}(k_x, k_y)|$ represents the edge-to-band optical transition for a given radiation polarization. From the selection rules described above, it can be seen that the relative difference of the rates $g_{k_x+1/2}$ and $g_{k_x-1/2}$ has to be proportional to the helicity of the photons P_circ; therefore, the selection rules can be presented as:

$$\frac{g_{+1/2}(k_x) - g_{-1/2}(-k_x)}{g_{+1/2}(k_x) + g_{-1/2}(-k_x)} = K P_\mathrm{circ}. \quad (56)$$

Herein, $g_{\pm 1/2}$ are the probabilities of the transitions from initial states with $s = \pm 1/2$, K is the coefficient describing the rigidity of the selection rules, and P_{circ} is the radiation helicity. With the help of the Bernevig-Hughes-Zhang (BHZ) model, it can be shown that the coefficient K only weakly depends on k_x and the photon energy $\hbar\omega$. For details see Ref. [95] and the supplemental material of Ref. [25].

The edge current is then given by:

$$j_x = -e \sum_{k_x s} \tau_p (\epsilon_{k_x s} v_{k_x s} g_{k_x s}), \tag{57}$$

where $v_{k_x s}$ is the velocity and τ_p is the momentum relaxation time determined by the backscattering processes. The spin-relaxation of the bulk carriers is assumed to be fast; hence, the photoexcited carriers get unpolarized before they are trapped back on the helical edge states. This means that only the depopulation of the edge states determines the photocurrent. By considering Kramer's degeneracy, which is given by $\epsilon_{k_x s} = \epsilon_{-k_x -s}$ and $\epsilon^c_{k_x k_y s} = \epsilon_{-k_x -k_y -s}$, the formula for the edge photocurrent can be rewritten as:

$$j_x = -\frac{eKP_{\mathrm{circ}}}{e\pi\hbar} \int \tau_p(\epsilon) g_{\mathrm{tot}}(\epsilon) d\epsilon. \tag{58}$$

Here, $g_{\mathrm{tot}}(\epsilon) = g_{+1/2} + g_{-1/2}$ is the total rate of the photoionization of electrons, which are excited by circularly polarized radiation with energy ϵ.

In Fig. 47(b), the calculated currents for photon energies of $\hbar\omega = 6.7\,\mathrm{meV}$ and $\hbar\omega = 10.4\,\mathrm{meV}$ are depicted for Fermi levels in the bulk gap. For the calculation shown here, a step-like function of the momentum relaxation time is assumed [25]. For the Fermi energy in the band gap, it is set to $\tau_p = 20\,\mathrm{ps}$, approximated from the length of the ballistic transport edge $l_{54} \approx 2.8\,\mu\mathrm{m}$ and the edge state velocity $\sim 10^7\,\mathrm{cm/s}$. For Fermi energies in the conduction band, the momentum relaxation time is estimated from the bulk mobility with a value of $\tau_p = 0.3\,\mathrm{ps}$. By comparing these results with the measured ones, which are magnified depicted in Fig. 47(a), a clear narrowing of the peak occurs with a decrease in the photon energy in both cases. Moreover, the amplitude for $\hbar\omega = 10.4\,\mathrm{meV}$ is smaller than that for $\hbar\omega = 6.7\,\mathrm{meV}$. The obtained decrease in the photocurrent magnitude for large ω can be attributed to a reduction in

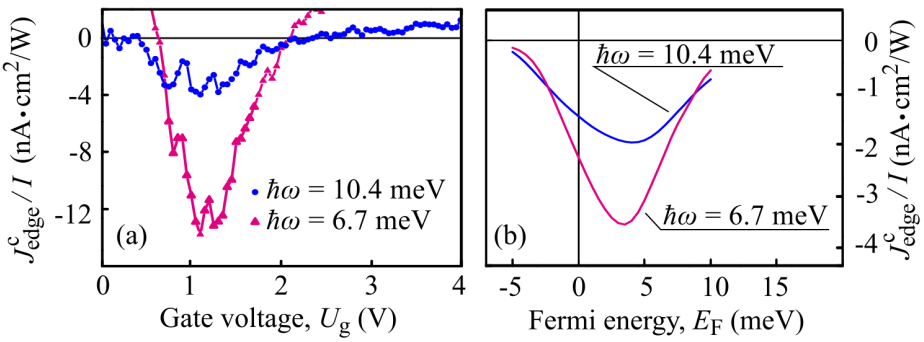

Figure 47: Comparison of (a) experimental and (b) calculated circular edge photocurrent in region II for two photon energies ($\hbar\omega = 10.4\,\text{meV}$ (blue) and $\hbar\omega = 6.7\,\text{meV}$ (red)). The calculated currents are shown as a function of E_F counted from the Dirac point.

the photon density at a fixed radiation intensity and a reduced probability of edge-band optical transitions. This probability reduction occurs because the overlap between the wave functions of the edge and bulk states decreases with the photon energy, as seen in the supplemental material in Ref. [25].

In conclusion, the here introduced theory can nicely describe the dependence of the photocurrent on the gate voltage and the radiation frequency. In addition, the magnitude of the calculations and that of the experiments are in the same order. Therefore, the current generation in region II can be attributed to the effect of photoioniziation.

5.3.3 Photocurrents in the Valence Band Regime

Now, the discussion turns to the photocurrent generation in region III. In this region, the applied negative gate voltages shift the Fermi level further towards the valence band edge. Therefore, the photosignals – similar to the effects discussed above – can be contributed to transitions from the valence band to the edge states.

In Fig. 48, such transitions are depicted for an excitation with right-handed circularly polarized radiation. To explain the change of sign of the photosignal compared to region II, as seen in the experimental data, the selection rules

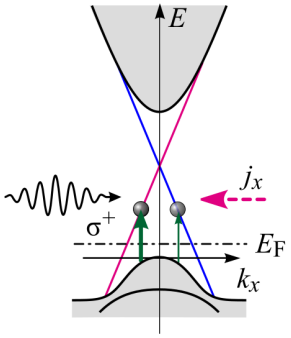

Figure 48: Schematic picture of optical transitions from the valence band to the edge states for a Fermi level close to the valence band top (region III). The different thicknesses of the green arrows indicate the difference of the optical transition probability for spin-up and spin-down states. In contrast to region II the resulting photocurrent direction is reversed.

for the optical transitions have to be reversed. So, the transition from the $s = +1/2$ edge state would have to occur with a higher probability compared to the one starting from states with $s = -1/2$ for an excitation with σ^+-polarized radiation. This is depicted in Fig. 48 by different thicknesses of the green arrows. Such a reversal of the selection rules, however, is not compatible with the BHZ model used for the previous calculations.

In fact, such a disagreement is not surprising as the real valence band structure of 8 nm HgTe QWs is quite complex. The closely lying excited $|H2\rangle$ subband, which is completely neglected in the BHZ model, has a strong influences on the valence band structure. This results in a non-monotonic dispersion of the hole states and leads to the formation of side maxima [100]. In addition, the change in the sign of the current can also be related to a strong energy-dependence of the momentum relaxation time. For a realistic calculation and a fully understanding of the photocurrent based on transitions from valence band states to edge states, a detailed knowledge of the real band structure beyond the BHZ model would be required. Such a detailed simulation of the band structure is still a challenging and difficult task.

5.4 Brief Summary

In this chapter, circular photogalvanic currents excited by terahertz radiation in 2D HgTe topological insulators are observed. In detail, 8 nm QWs are investigated, which exhibit a quantized conductance of $2e^2/h$, characterizing the quantum spin Hall regime. Through measurements in a wide range of gate voltages, it is shown that in these samples, a photosignal can be excited which flows along the edges of the sample and shows a strong helicity-sensitive behaviour. The latter means that the photosignal direction is reversed by switching from right- to left-handed circularly polarized radiation, as shown in Figs. 40 and 41.

By extracting the pure edge and bulk contribution, it is shown that the origin of these photosignals can be segmented into three regions. In region I, where the Fermi level lies deep in the conduction band, the whole photosignal has to be generated by bulk carriers. The formation of the helicity-sensitive bulk photocurrent can be attributed to the circular photogalvanic effect, whereas the part flowing in the edges is attributed to a diffusive scattering at the boundaries of the sample and the action of the electric field of the circularly polarized radiation on the carriers.

By tuning the Fermi level below the conduction band bottom, region II is reached. The measured data reveal that the photocurrent in this region is caused by photoionization of helical edge electrons into the conduction band. The strong helicity-dependence of this current arises due to the selection rules, where for a fixed radiation helicity, the probabilities for transitions from spin-up and spin-down states are different, which results in a photocurrent generation. A comparison of the calculated photocurrent (Eq. (58)) and the experimentally obtained data shows that all relevant features can be described with this theory. For example, by decreasing the photon energy, a narrowing of the peak with an increased magnitude is found for both cases.

The photocurrent in region III – similar to the effect of region II – can be attributed to transitions from the valence band to the edge states of the system. To obtain the change in the photocurrent direction found in the experiments, the selection rules would have to be reversed. A theoretical calculation of the

photocurrents in this region would require a detailed knowledge of the real band structure and the optical transitions in non-trivial HgTe QWs, which is still a challenging task.

6 Conclusion

In the framework of this thesis, two- and three-dimensional topological insulators are investigated with opto-electronic effects in the terahertz range. It is demonstrated that in both cases, photogalvanic effects can be utilized for the detection and the analysis of Dirac fermion states.

In the three-dimensional case, a cyclotron-resonance-enhanced photocurrent is observed by exciting 80 nm strained HgTe films with terahertz radiation. The arising resonances could be clearly attributed to the topologically protected top and bottom surface states of the system. Studying these resonant responses in a gated sample, the behaviour of the photocurrent is observed upon a modification of the Fermi energy, which allowes the extraction of the cyclotron masses of the top and bottom surface states as a function of the Fermi energy. For larger gate voltages, an additional cyclotron resonance is detected, which is caused by bulk carriers and corresponds to a mass about two times larger than that obtained for the surface states.

These results are in full agreement with the band structure of the strained HgTe films, calculated by the $\boldsymbol{k} \cdot \boldsymbol{p}$ method. The cyclotron masses of the surface states estimated from this calculation fit well with the experimental ones. Based on the experimental results, a microscopic theory of the resonant photocurrent is developed. It is shown that an orbital effect emerges due to an asymmetric scattering of non-equilibrium surface electrons, resulting in a fully spin-polarized direct electric current, which exhibits a resonant behaviour due to the cyclotron-resonance-enhanced absorbance.

Photogalvanic spectroscopy is also used for the investigation of two-dimensional topological insulators. There spin-polarized photogalvanic currents flowing mainly in the edges of the sample are observed by exciting 2D HgTe QWs with circularly polarized terahertz radiation. These currents exhibit a strong helicity-dependence, meaning that the reversal of the radiation helicity reverses the direction of the photocurrent. Moreover, the sign of the photosignal for a fixed helicity is opposite for the opposite edge, which demonstrates that the current indeed flows in the edges of the sample. Such chiral edge photocurrents

are detected in a wide range of applied gate voltages, in which they change their sign twice, which allows a division into three different regions.

The mechanisms responsible for the generation of the photocurrent strongly depend on the location of the Fermi level within the band structure. For a Fermi level in the conduction band, the helicity-sensitive photocurrent flowing in the bulk can be attributed to the circular photogalvanic effect, whereas the part generated in the edges is attributed to diffusive scattering at the boundaries of the sample together with the action of the electric field of the circularly polarized radiation on the carrier. In contrast to this, in the TI-regime, the photocurrent is caused by a photoionization of helical edge electrons into the conduction band. For this effect, a microscopic model and the microscopic theory are developed simultaneous to the experiments. It is shown that due to spin-dependent selection rules, the photoionization from spin-up and spin-down branches induced by right- and left-handed circularly polarized radiation is different, which leads to an imbalance of the edge state population and thus to an electric net current. A similar effect is expected for a Fermi level near the valence band region. The photocurrent generation is attributed to transitions from the valence band to the edge sates. However, no full theory could be given till now, as this would require a full understanding of the complex band structure of HgTe near the valence band.

To conclude, this work clearly demonstrated that opto-electronic methods present a convenient tool for the investigation of two- and three-dimensional topological insulators and can even be suitable for the search for new topological insulators. An important feature of this kind of investigation is that it can be applied to diverse geometries and states of samples. Thus, opto-electronic effects can be utilised for micrometre-sized samples where pure optical methods can no longer be performed. Furthermore, the CR-assisted investigation of 3D TI can even be carried out in samples where classical *dc* transport is hardly possible. For example, it can be used in samples with a high residual carrier density of the bulk or in samples with a Fermi energy lying in the conduction band.

References

[1] F. Bloch, *Über die Quantenmechanik der Elektronen in Kristallgittern*, Z. Phys. **52**, 555 (1929).

[2] J.M. Kosterlitz and D.J. Thouless, *Long range order and metastability in two dimensional solids and superfluids. (Application of dislocation theory)*, J. Phys. C: Solid State Phys. **5**, L124 (1972).

[3] J.M. Kosterlitz and D.J. Thouless, *Ordering, metastability and phase transitions in two-dimensional systems*, J. Phys. C: Solid State Phys. **6**, 1181 (1973).

[4] F.D.M. Haldane, *Continuum dynamics of the 1-D Heisenberg antiferomanget: Identification with the O(3) nonlinear sigma model*, Phys. Lett. A **93**, 464 (1983).

[5] F.D.M. Haldane, *Model for a Quantum Hall Effect without Landau Levels: Condensed-Matter Realization of the "Parity Anomaly"*, Phys. Rev. Let. **61**, 2015 (1988).

[6] Nobel Media AB 2014, "*The 2016 Nobel Prize in Physics - Press Release.*" http://www.nobelprize.org/nobel_prizes/physics/laureates/2016/press.html, visited on 24. 08. 2017.

[7] D.J. Thouless, M. Kohmoto, M.P. Nightingale, and M. den Nijs, *Quantized Hall Conductance in a Two-Dimensional Periodic Potential*, Phys. Rev. Lett **49**, 405 (1982).

[8] B.A. Bernevig and S.-C. Zhang, *Quantum Spin Hall Effect*, Phys. Rev. Lett. **96**, 106802 (2006).

[9] C.L. Kane and E.J. Mele, *Quantum Spin Hall Effect in Graphene*, Phys. Rev. Lett. **95**, 226801 (2005).

[10] Y. Ando, *Topological Insulator Materials*, J. Phys. Soc. Jpn. **82**, 102001 (2013).

[11] J.P. Faurie, S. Sivananthan, M. Boukerche, and J. Reno, *Molecular beam epitaxial growth of high quality HgTe and $Hg_{1-x}Cd_xTe$ onto GaAs(001)substrates*, Appl. Phys. Lett **45**, 1307 (1984).

[12] S.A. Dvoretsky, N.N. Mikhailov, Yu.G. Sidorov, V.A. Shvets, S.N. Danilov, B. Wittman, and S.D. Ganichev, *Growth of HgTe Quantum Wells for IR to THz Detectors*, J. Electron. Mater. **39**, 918 (2010).

[13] C.R. Becker, *Growth and properties of HgTe quantum wells - A topic review*, Phys. Status Solidi B **251**, 1125 (2014).

[14] N.N. Berchenko and M.V. Pashkovskii, *Mercury telluride - a zero-gap semiconductor*, Sov. Phys. Usp. **19**, 462 (1976).

[15] J. Chu and A. Sher, *Physics and Properties of Narrow Gap Semiconductors*. (Springer, 2008).

[16] B.A. Bernevig, T.L. Hughes, and S.-C. Zhang, *Quantum Spin Hall Effect and Topological Phase Transition in HgTe Quantum Wells*, Science **314**, 1757 (2006).

[17] M. König, S. Wiedmann, C. Brüne, A. Roth, H. Buhmann, L.W. Molenkamp, X.-L. Qi, and S.-C. Zhang, *Quantum Spin Hall Insulator State in HgTe Quantum Wells*, Science **318**, 766 (2007).

[18] C. Brüne, C.X. Liu, E.G. Novik, E.M. Hankiewicz, H. Buhmann, Y.L. Chen, X.L. Qi, Z.X. Shen, S.C. Zhang, and L.W. Molenkamp, *Quantum Hall Effect from the Topological Surface States of Strained Bulk HgTe*, Phys. Rev. Lett. **106**, 126803 (2011).

[19] B. Büttner, C.X. Liu, G. Tkachov, E.G. Novik, C. Brüne, H. Buhmann, E.M. Hankiewicz, P. Recher, B. Trauzettel, S.C. Zhang, and L.W. Molenkamp, *Single valley Dirac fermions in zero-gap HgTe quantum wells*, Nature Phys. **7**, 418 (2011).

[20] E.L. Ivchenko and S.D. Ganichev, *Spin-Photogalvanics*, in *Spin Physics in Semiconductors*, M.I. Dyakonov, ed. (Springer, 2017).

[21] J.W. McIver, D. Hsieh, H. Steinberg, P. Jarillo-Herrero, and N. Gedik, *Control over topological insulator photocurrents with light polarization*, Nat. Nanotechnol. **7**, 96 (2012).

[22] P. Olbrich, L.E. Golub, T. Herrmann, S.N. Danilov, H. Plank, V.V. Bel'kov, G. Mussler, Ch. Weyrich, C.M. Schneider, J. Kampmeier, D. Grützmacher, L. Plucinski, M. Eschbach, and S.D. Ganichev, *Room-Temperature High-Frequency Transport of Dirac Fermions in Epitaxially Grown Sb_2Te_3- and Bi_2Te_3-Based Topological Insulators*, Phys. Rev. Lett. **113**, 096601 (2014).

[23] P. Olbrich, C. Zoth, P. Vierling, K.-M. Dantscher, G.V. Budkin, S.A. Tarasenko, V.V. Bel'kov, D.A. Kozlov, Z.D. Kvon, N.N. Mikhailov, S.A. Dvoretsky, and S.D. Ganichev, *Giant photocurrents in a Dirac fermion system at cyclotron resonance*, Phys. Rev. B **87**, 235439 (2013).

[24] K.-M. Dantscher, D.A. Kozlov, P. Olbrich, C. Zoth, P. Faltermeier, M. Lindner, G.V. Budkin, S.A. Tarasenko, V.V. Bel'kov, Z.D. Kvon, N.N. Mikhailov, S.A. Dvorestky, D. Weiss, B. Jeninchen, and S.D. Ganichev, *Cyclotron-resonance-assisted photocurrents in surface states of a three-dimensional topological insulator based on a strained high-mobility HgTe film*, Phys. Rev. B **92**, 165314 (2015).

[25] K.-M. Dantscher, D.A. Kozlov, M.T. Scherr, S. Gebert, J. Bärenfänger, M.V. Durnev, S.A. Tarasenko, V.V. Bel'kov, N.N. Mikhailov, S.A. Dvorestky, Z.D. Kvon, J. Ziegler, D. Weiss, and S.D. Ganichev, *Photogalvanic probing of helical edge channels in two-dimensional HgTe topological insulators*, Phys. Rev. B **95**, 201103(R) (2017).

[26] S.-Q. Shen, *Topological Insulators: Dirac Equation in Condensed Matters*. (Springer, 2012).

[27] G. Tkachov, *Topological Insulators: The Physics of Spin Helicity in Quantum Transport*. (Pan Stanford Publishing, 2016).

[28] M. Franz and L. Molenkamp, eds., *Topological Insulators*. Contemporary Concepts of Condensed Matter Science. (Elsevier, 2013).

[29] J.E. Moore, *The birth of topological insulators*, Nature **464**, 194 (2010).

[30] M.Z. Hasan and C.L. Kane, *Colloquium: Toplogical insulators*, Rev. Mod. Phys. **82**, 3045 (2010).

[31] M. Nakahara, *Geometry, Topology and Physics*, Graduate Student Series in Physics. (Taylor & Francis Group, 2003).

[32] K. v. Klitzing, G. Dorda, and M. Pepper, *New Method for High-Accuracy Determination of the Fine-Structure Constant Based on Quantized Hall Resistance*, Phys. Rev. Lett **45**, 494 (1980).

[33] R.S.K. Mong and V. Shivamoggi, *Edge states and the bulk-boundary correspondence in Dirac Hamiltonians*, Phys. Rev. B **83**, 125109 (2011).

[34] Y. Hatsugai, *Chern Number and Edge States in the Integer Quantum Hall Effect*, Phys. Rev. Lett **71**, 3697 (1993).

[35] C.L. Kane and E.J. Mele, *Z_2 Topological Order and the Quantum Spin Hall Effect*, Phys. Rev. Lett. **95**, 146802 (2005).

[36] M. König, H. Buhmann, L.W. Molenkamp, T. Hughes, C.-X. Liu, X.-L. Qi, and S.-C. Zhang, *The Quantum Spin Hall Effect: Theory and Experiment*, J. Phys. Soc. Jpn. **77**, 031007 (2008).

[37] E. Wigner, *Über die Operation der Zeitumkehr in der Quantenmechanik*, Nachr. Ges. Wiss. zu Gött., Math.-Phys. Klasse **1932**, 546 (1932).

[38] L. Fu and C.L. Kane, *Topological insulators with inversion symmetry*, Phys. Rev. B **76**, 045302 (2007).

[39] L. Fu, C.L. Kane, and E.J. Mele, *Topological Insulators in Three Dimensions*, Phys. Rev. Lett **98**, 106803 (2007).

[40] J.E. Moore and L. Balents, *Topological invariants of time-reversal-invariant band structures*, Phys. Rev. B **75**, 121306(R) (2007).

[41] R. Roy, *Topological phases and the quantum spin Hall effect in three dimensions*, Phys. Rev. B **79**, 195322 (2009).

[42] Y. Yao, F. Ye, X.-L. Qi, S.-C. Zhang, and Z. Fang, *Spin-orbit gap of graphene: First-principles calculations*, Phys. Rev. B **75**, 041401(R) (2007).

[43] H. Min, J.E Hill, N.A. Sinitsyn, B.R. Sahu, L. Kleinman, and A.H. MacDonald, *Intrinsic and Rashba spin-orbit interactions in graphene sheets*, Phys. Rev. B **74**, 165310 (2006).

[44] D. Hsieh, D. Qian, L. Wray, Y. Xia, Y.S. Hor, R.J. Cava, and M.Z. Hasan, *A topological Dirac insulator in a quantum spin Hall phase*, Nature **452**, 970 (2008).

[45] Y. Xia, D. Qian, D. Hsieh, L. Wray, A. Pal, H. Lin, A. Bansil, D. Grauer, Y.S. Hor, R.J. Cava, and M.Z. Hasan, *Observation of a large-gap topological-insulator class with a single Dirac cone on the surface*, Nature Phys. **5**, 398 (2009).

[46] Y.L. Chen, J.G. Analytis, J.-H. Chu, Z.K. Liu, S.-K. Mo, X.L. Qi, H.J. Zhang, D.H. Lu, X. Dai, Z. Fang, S.C. Zhang, I.R. Fisher, Z. Hussain, and Z.-X. Shen, *Experimental Realization of a Three-Dimensional Topological Insulator,* Bi_2Te_3, Science **325**, 5937 (2009).

[47] D.J. Chadi, J.P. Walter, M.L. Cohen, Y. Petroff, and M. Balkanski, *Reflectivities and Electronic Band Structure of CdTe and HgTe*, Phy. Rev. B **5**, 3058 (1972).

[48] X. Dai, T.L. Hughes, X.-L. Qi, Z. Fang, and S.-C. Zhang, *Helical edge and surface states in HgTe quantum wells and bulk insulators*, Phys. Rev. B **77**, 125319 (2008).

[49] J.-W. Luo and A. Zunger, *Design Principles and Coupling Meachanisms in the 2D Quantum Well Topological Insulator HgTe/CdTe*, Phys. Rev. Lett. **105**, 176805 (2010).

[50] S.D. Ganichev and W. Prettl, *Intense Terahertz Excitation of Semiconductors*. (Oxford Univ. Press, 2006).

[51] S.D. Ganichev and W. Prettl, *Spin photocurrents in quantum wells*, J. Phys.: Condens. Matter **15**, R935 (2003).

[52] S.D. Ganichev, V.V. Bel'kov, P. Schneider, E.L. Ivchenko, S.A Tarasenko, W. Wegschneider, D. Weiss, D. Schuh, E.V. Beregulin, and W. Prettl, *Resonant inversion of the circular photogalvanic effect in n-doped quantum wells*, Phys. Rev. B **68**, 035319 (2003).

[53] H. Ibach and H. Lüth, *Festkörperphysik: Einführung in die Grundlagen*. (Springer, 2009).

[54] K. Seeger, *Semiconductor Physics: An Introduction*. (Springer, 2004).

[55] S. Hunklinger, *Festkörperphysik*. (De Gruyter, 2009).

[56] K. Kopitzki and P. Herzog, *Einführung in die Festkörperphysik*. (Springer, 2007).

[57] T. Numai, *Fundamentals of Semiconductor Lasers*. (Springer, 2004).

[58] T. Ihn, *Semiconductor Nanostructures*. (Oxford University Press, 2010).

[59] L.D. Landau and E.M. Lifshitz, *Quantum Mechanics: Non-relativistic Theory*. (Pergamon Press, 1965).

[60] C. Zoth, "Terahertz Laser Radiation Induced Opto-Electronic Effects in HgTe Based Nanostructures." PhD thesis, University of Regensburg, 2014.

[61] V.V. Bel'kov and S.D. Ganichev, *Magneto-gyrotropic effects in semiconductor quantum wells*, Semicond. Sci. Technol. **23**, 114003 (2008).

[62] S.D. Ganichev, V.V. Bel'kov, S.A. Tarasenko, S.N. Danilov, S. Giglberger, C. Hoffmann, E.L. Ivchenko, D. Weiss, W. Wegscheider, C. Gerl, D. Schuh, J. Stahl, J. De Boeck, G. Borghs, and W. Prettl, *Zero-bias spin separation*, Nature Phys. **2**, 609 (2006).

[63] Z.D. Kvon, S.N. Danilov, D.A. Kozlov, C. Zoth, N.N. Mikhailov, S.A. Dvoretskii, and S.D. Ganichev, *Cyclotron Resonance of Dirac fermions in HgTe Quantum Wells*, JETP Lett. **94**, 816 (2011).

[64] J. Ludwig, Y.B. Vasilyev, N.N. Mikhailov, J.M. Poumirol, Z. Jiang, O. Vafek, and D. Smirnov, *Cyclotron resonance of single-valley Dirac fermions in nearly gapless HgTe quantum wells*, Phys. Rev. B **89**, 241406(R) (2014).

[65] O. Svelto, *Principles of Lasers.* (Springer, 2010).

[66] P. Olbrich, "THz radiation induced spin polarized currents in low dimensioanl semiconductor structures." PhD thesis, University of Regensburg, 2010.

[67] K. Renk, *Basics of Laser Physics.* (Springer, 2012).

[68] S.A. Dvoretsky, D.G. Ikusov, Z.D. Kvon, N.N. Mikhailov, V.G. Remesnik, R.N. Smirnov, Yu.G. Sidorov, and V.A. Shvets, *HgCdTe quantum wells grown by molecular beam epitaxy*, SPQEO **10**, 47 (2007).

[69] D.A. Kozlov, Z.D. Kvon, E.B. Olshanetsky, N.N. Mikhailov, S.A. Dvoretsky, and D. Weiss, *Transport Properties of a 3D Topological Insulator based on a Strained High-Mobility HgTe Film*, Phys. Rev. Lett. **112**, 196801 (2014).

[70] X.-L. Qi and S.-C. Kane, *Topological insulators and superconductors*, Rev. Mod. Phys **83**, 1057 (2011).

[71] Z.D. Kvon, E.B. Olshanetsky, D.A. Kozlov, N.N. Mikhailov, and S.A. Dvoretskii, *Two-Dimensional Electron-Hole System in a HgTe-Based Quantum Well*, JETP Lett. **87**, 502 (2008).

[72] T. Herrmann, I.A. Dmitriev, D.A. Kozlov, M. Schneider, B. Jentzsch, Z.D. Kvon, P. Olbrich, V.V. Bel'kov, A. Bayer, D. Schuh, D. Bougeard, T. Kuczmik, M. Oltscher, D. Weiss, and S.D. Ganichev, *Analog of microwave-induced resistance oscillations induced in GaAs heterostructures by terahertz radiation*, Phys. Rev. B **94**, 081301(R) (2016).

[73] G. Abstreiter, J.P. Kotthaus, J.F. Koch, and G. Dorda, *Cyclotron resonance of electrons in surface space-charge layers on silicon*, Phys. Rev. B **14**, 2480 (1976).

[74] C. Zoth, P. Olbrich, P. Vierling, K.-M. Dantscher, V.V. Bel'kov, M.A. Semina, M.M. Glazov, L.E. Golub, D.A. Kozlov, Z.D. Kvon, N.N. Mikhailov, S.A. Dvorestky, and S.D. Ganichev, *Quantum oscillations of photocurrents in HgTe quantum wells with Dirac and parabolic dispersions*, Phys. Rev. B **90**, 205415 (2014).

[75] A.M. Shuvaev, G.V. Astakov, G. Tkachov, C. Brüne, H. Buhmann, L.W. Molenkamp, and A. Pimenov, *Terahertz quantum Hall effect of Dirac fermions in a topological insulator*, Phys. Rev. B **87**, 121104(R) (2013).

[76] V. Dziom, A. Shuvaev, A. Pimenov, G.V. Astakhov, C. Ames, K. Bendias, J. Böttcher, G. Tkachov, E.M. Hankiewicz, C. Brüne, H. Buhmann, and L.W. Molenkamp, *Observation of the universal magnetoelectric effect in a 3D topological insulator*, Nat. Commun **8**, 15197 (2017).

[77] M.S. Zholudev, A.V. Ikonnikov, F. Teppe, M. Orlita, K.V. Maremyanin, K.E. Spirin, V.I. Gavrilenko, W. Knap, S.A. Dvoretskiy, and N.N. Mihailov, *Cyclotron resonance in HgTe/CdTe-based heterostructures in high magnetic field*, Nanoscale Res. Lett. **7**, 534 (2012).

[78] T. Heinzel, *Mesoscopic Electronics in Solid State Nanostructures.* (Wiley-VCH, 2010).

[79] G. Abstreiter, P. Kneschaurek, J.P. Kotthaus, and J.F. Koch, *Cyclotron Resonance of Electrons in an Inversion Layer on Si*, Phys. Rev. Lett. **32**, 104 (1974).

[80] K.S. Novoselov, A.K. Geim, S.V. Morozov, D. Jiang, M.I.Katsnelson, I.V. Grigorieva, S.V. Dubonos, and A.A. Firsov, *Two-dimensional gas of massless Dirac fermions in graphene*, Nature **438**, 197 (2005).

[81] A.H. Castro Neto, F. Guinea, N.M.R. Peres, K.S. Novoselov, and A.K. Geim, *The electronic properties of graphene*, Rev. Mod. Phys. **81**, 109 (2009).

[82] V.P. Gusynin and S.G. Sharapov, *Magnetic oscillations in planar systems with the Dirac-like spectrum of quasiparticle excitations. II. Transport properties*, Phys. Rev. B **71**, 125124 (2005).

[83] B.K.-C. Chuang, R.S. Deacon, R.J. Nicholas, K.S. Novoselov, and A.K. Geim, *Cyclotron resonance of electrons and holes in graphene monolayers*, Phil. Trans. R. Soc. A **366**, 237 (2008).

[84] B. Wittmann, S.N. Danilov, V.V. Bel'kov, S.A. Tarasenko, E.G. Novik, H. Buhmann, C. Brüne, L.W. Molenkamp, Z.D. Kvon, N.N. Mikhailov, S.A. Dvoretsky, N.Q. Vinh, A.F.G. van der Meer, B. Murdin, and S.D. Ganichev, *Circular photogalvanic effect in HgTe/CdHgTe quantum well structures*, Semicond. Sci. Technol. **25**, 095005 (2010).

[85] H. Diehl, V.A. Shalygin, L.E. Golub, S.A Tarasenko, S.N. Danilov, V.V. Bel'kov, E.G. Novik, H. Buhmann, C. Brüne, L.W. Molenkamp, E.L. Ivchenko, and S.D. Ganichev, *Nonlinear magnetogyrotropic photogalvanic effect*, Phys. Rev. B **80**, 075311 (2009).

[86] S.D. Ganichev, S.A. Tarasenko, J. Karch, J. Kamann, and Z.D. Kvon, *Magnetic quantum ratchet effect in Si-MOSFETs*, J. Phys.: Condens. Matter **26**, 255802 (2014).

[87] S.A. Tarasenko, *Electron scattering in quantum wells subjected to an in-plane magnetic field*, Phys. Rev. B **77**, 085328 (2008).

[88] G.M. Gusev, Z.D. Kvon, O.A. Shegai, N.N. Mikhailov, and S.A. Dvoretsky, *Aharonov Bohm effect in 2D topological insulator*, Solid State Commun. **205**, 4 (2015).

[89] J. Karch, C. Drexler, P. Olbrich, M. Fehrenbacher, M. Hirmer, M.M Glazov, S.A Tarasenko, E.L. Ivchenko, B. Birkner, J. Eroms, D. Weiss, R. Yakimova, S. Lara-Avila, S. Kubatkin, M. Ostler, T. Seyller, and

S.D. Ganichev, *Terahertz Radiation Driven Chiral Edge Currents in Graphene*, Phys. Rev. Lett. **107**, 276601 (2011).

[90] M.M. Glazov and S.D. Ganichev, *High frequency electric field induced nonlinear effects in graphene*, Phys. Rep. **535**, 101 (2014).

[91] Privat communiction with S. Ganichev.

[92] V.L. Gurevich and R. Laiho, *Photomagnetism of metals: Microscopic theory of the photoinduced surface current*, Phys. Rev. B **48**, 8307 (1993).

[93] V.L. Al'perovich, V.I. Belinicher, V.N. Novikov, and A.S. Terekhov, *Surface photovoltaic effect in gallium arsenide*, JETP Lett. **31**, 546 (1980).

[94] S.N. Artemenko and V.O. Kaladzhyan, *Photogalvanic effects in topological insulators*, JETP Lett. **97**, 82 (2013).

[95] V. Kaladzhyan, P.P. Aseev, and S.N. Artemenko, *Photogalvanic effect in the HgTe/CdTe topological insulator due to edge-bulk optical transitions*, Phys. Rev. B **92**, 155424 (2015).

[96] J.I. Väyrynen, M. Goldstein, and L.I. Glazman, *Helical Edge Resistance Introduced by Charge Puddles*, Phys. Rev. Lett. **110**, 216402 (2013).

[97] B.L. Altshuler, I.L. Aleiner, and V.I. Yudson, *Localization at the Edge of a 2D Topological Insulator by Kondo Impurities with Random Anisotropies*, Phys. Rev. Lett. **111**, 086401 (2013).

[98] S. Essert and K. Richter, *Magnetotransport in disordered two-dimensional topological insulators: signatures of charge puddles*, 2D Matt. **2**, 024005 (2015).

[99] L.I. Magarill and M.V. Entin, *Circular Photogalvanic Effect Caused by the Transitions between Edge and 2D States in a 2D Topological Insulator*, JETP Lett. **104**, 771 (2016).

[100] G.M. Minkov, A.V. Germanenko, O.E. Rut, A.A. Sherstobitov, M.O. Nestoklon, S.A. Dvoretski, and N.N. Mikhailov, *Spin-orbit splitting of valence and conduction bands in HgTe quantum wells near the Dirac point*, Phys. Rev. B **93**, 155304 (2016).

Acknowledgment

An dieser Stelle möchte ich mich herzlichst bei allen bedanken, ohne die das Verfassen dieser Arbeit niemals möglich gewesen wäre.

Im Besonderen möchte ich mich bei Sergey Ganichev bedanken, der mir dieses spannende und viel versprechende Thema zugetraut hat. Danke, dass Du stets Zeit für meine Fragen und für die zahlreichen Diskussionen gefunden hast. Ebenfalls möchte ich mich bei Dir bedanken, dass du es mir ermöglicht hast an zahlreichen Konferenzen weltweit teilzunehmen.

Ein großes Danke geht an Dima Kozlov, Dima Kvon und Vasily Bel'kov für ihre unermüdliche Unterstützung. Danke, für die zahlreichen Tipps im Labor und die geduldige Zusammenarbeit. Zusätzlich möchte ich bei Nikolai Mikhailov und Sergey Dvoretsky für die HgTe Proben bedanken. Vielen Dank, auch an Sergey Tarasenko, Grigory Budkin und Mikhail Durnev für die theoretische Unterstützung. Danke, dass Ihr all meinen Fragen stets mit einem offenen Ohr begegnet seid und niemals die Geduld verloren habt.

Des Weiteren möchte ich mich bei Sergey Danilov, Toni Humbs, Christian Schneider und Hannelore Lanz für Ihre hilfsbereite Unterstützung bedanken.

Für das Korrekturlesen dieser Arbeit möchte ich mich herzlichst bei Helene Plank und Tina Zoth bedanken.

Ein ganz besonderer Dank geht auch an meine Master- und Bachelorstudenten, Matthias Lindner, Maria-Theresia Scherr, Max Otteneder, Sebastian Gebert und Jan Bärenfänger. Danke für die produktive Zeit und die vielen interessanten und lehrreichen Stunden.

Ein ganz lieber Dank geht auch an meine Kollegen Helene Plank, Philipp Faltermeier und Tobias Herrmann. Ohne Euch wäre es nur halb so lustig, aufregend und verrückt gewesen. Vielen Dank für die zahlreichen Diskussion, Umtrünke und die geteilte Zeit. Für die tolle Arbeitsatmosphäre möchte ich mich neben den bereits genannten Personen noch bei Susanne Candussio, Stefan Hubmann und bei allen Ehemaligen bedanken.

Zu guter Letzt möchte ich meiner Familie danken. Danke, dass Ihr mir stets den Rücken freigehalten und meine Launen ertragen habt.